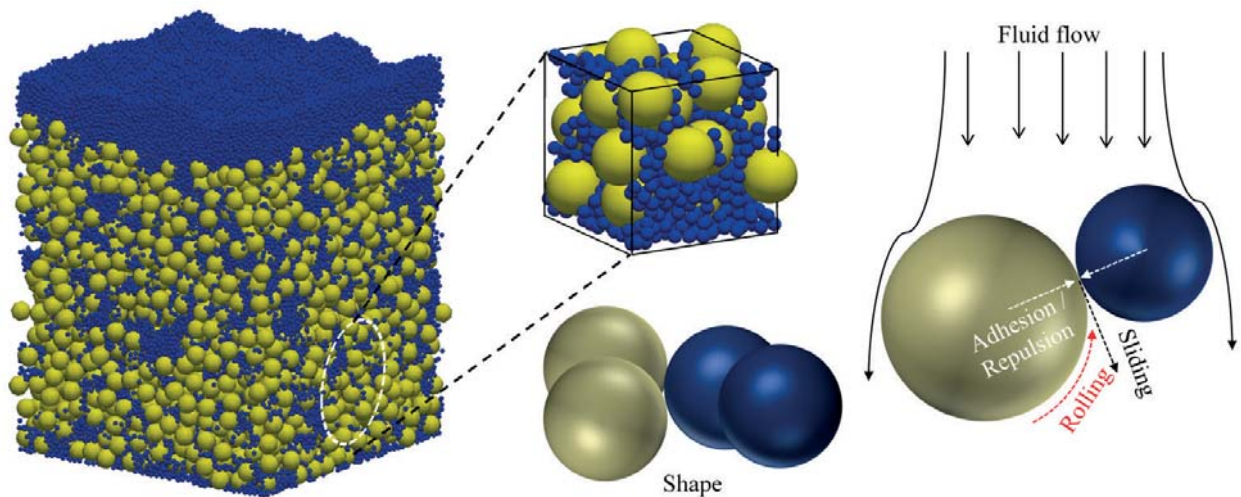


Ruturaj Deshpande

---

# Investigation of the Filter Cake Formation Process using DEM-CFD Simulation with Experimentally Calibrated Parameters



Fraunhofer-Institut für  
Techno- und Wirtschaftsmathematik ITWM

# Investigation of the Filter Cake Formation Process using DEM-CFD Simulation with Experimentally Calibrated Parameters

Ruturaj Deshpande

FRAUNHOFER VERLAG

**Kontakt:**

Fraunhofer-Institut für Techno- und Wirtschaftsmathematik ITWM  
Fraunhofer-Platz 1  
67663 Kaiserslautern  
Telefon +49 631/31600-0  
Fax +49 631/31600-1099  
E-Mail [info@itwm.fraunhofer.de](mailto:info@itwm.fraunhofer.de)  
URL [www.itwm.fraunhofer.de](http://www.itwm.fraunhofer.de)

**Bibliografische Information der Deutschen Nationalbibliothek**

Die Deutsche Nationalbibliothek verzeichnet diese Publikation in der Deutschen Nationalbibliografie; detaillierte bibliografische Daten sind im Internet über <http://dnb.d-nb.de> abrufbar.  
ISBN (Print): 978-3-8396-1519-5

**D 386**

Zugl.: Kaiserslautern, TU, Diss., 2019

Titelbild: © Ruturaj Deshpande

Druck: Mediendienstleistungen des  
Fraunhofer-Informationszentrum Raum und Bau IRB, Stuttgart

Für den Druck des Buches wurde chlor- und säurefreies Papier verwendet.

© by **FRAUNHOFER VERLAG**, 2019

Fraunhofer-Informationszentrum Raum und Bau IRB  
Postfach 80 04 69, 70504 Stuttgart  
Nobelstraße 12, 70569 Stuttgart  
Telefon 07 11 9 70-25 00  
Telefax 07 11 9 70-25 08  
E-Mail [verlag@fraunhofer.de](mailto:verlag@fraunhofer.de)  
URL <http://verlag.fraunhofer.de>

Alle Rechte vorbehalten

Dieses Werk ist einschließlich aller seiner Teile urheberrechtlich geschützt. Jede Verwertung, die über die engen Grenzen des Urheberrechtsgesetzes hinausgeht, ist ohne schriftliche Zustimmung des Verlages unzulässig und strafbar. Dies gilt insbesondere für Vervielfältigungen, Übersetzungen, Mikroverfilmungen sowie die Speicherung in elektronischen Systemen.

Die Wiedergabe von Warenbezeichnungen und Handelsnamen in diesem Buch berechtigt nicht zu der Annahme, dass solche Bezeichnungen im Sinne der Warenzeichen- und Markenschutz-Gesetzgebung als frei zu betrachten wären und deshalb von jedermann benutzt werden dürften. Soweit in diesem Werk direkt oder indirekt auf Gesetze, Vorschriften oder Richtlinien (z.B. DIN, VDI) Bezug genommen oder aus ihnen zitiert worden ist, kann der Verlag keine Gewähr für Richtigkeit, Vollständigkeit oder Aktualität übernehmen.

# **Investigation of the Filter Cake Formation Process using DEM-CFD Simulation with Experimentally Calibrated Parameters**

The Department of Mechanical and Process Engineering  
The Technischen Universität Kaiserslautern  
for obtaining the academic degree

**Doktor-Ingenieur (Dr.-Ing.)**

submitted

**Dissertation**

by

Mr.

M. Eng. Ruturaj Ramesh Deshpande

from Daund, India

Day of the oral examination: 5 June 2019.

Dean : Prof. Dr.-Ing. Jörg Seewig

Exam Chairman : Prof. Dr.-Ing. Hans-Jörg Bart

1. Examiner : Prof. Dr.-Ing. Sergiy Antonyuk

2. Examiner : Prof. Dr. Oleg Iliev



# **Untersuchung des Filterkuchenbildungsprozesses unter Verwendung der DEM-CFD Simulation mit Experimentell Kalibrierten Parametern**

Dem Fachbereich Maschinenbau und Verfahrenstechnik  
der Technischen Universität Kaiserslautern  
zur Erlangung des akademischen Grades

**Doktor-Ingenieur (Dr.-Ing.)**

vorgelegte

**Dissertation**

von

Herrn

M. Eng. Ruturaj Ramesh Deshpande

aus Daund, India

Tag der mündlichen Prüfung: 5. Juni 2019.

Dekan : Prof. Dr.-Ing. Jörg Seewig

Prüfungsvorsitzender : Prof. Dr.-Ing. Hans-Jörg Bart

1. Berichterstatter : Prof. Dr.-Ing. Sergiy Antonyuk

2. Berichterstatter : Prof. Dr. Oleg Iliev



---

## Abstract

---

The solid-fluid separation can be realized by the deposition of the solid phase (particles) within the filtering medium (depth filtration) or by the deposition of the solid phase on the surface of the filtering medium (cake formation). The process of cake filtration is used in many process industries where large quantities of solids are to be recovered/filtered. The present study is dedicated to the investigation of the filter cake formation process using DEM-CFD simulation with experimentally calibrated parameters.

The experimental studies in the literature lack the information about the particle-particle interaction parameters (coefficients of restitution and frictions). The experimental measurement of these properties is one of the goals of this thesis. In this thesis, the numerical analysis is carried out using the *two-way volume averaged coupling approach between the DEM and the CFD*. For performing the numerical study involving the bi-dispersed spherical or the non-spherical particles, appropriate drag models are implemented and validated. Then the sensitivity analysis of the various factors affecting the structure of the packed bed/cakes is performed. Further, the consolidation in the packed beds/cakes due to the fluid forces is studied.

The major conclusions of the thesis are: Increase in coefficient of frictions and work of adhesion tends to increase the final void fraction of the packed beds/cakes. For the bi-dispersed particles, the pressure drop increases with the increase in the mass fraction of the bigger particles. The void fraction of the packed bed/cake increases with the decrease in the sphericity. Further, the correlations developed between the void fraction and the Reynolds number are useful in predicting the changed void fraction (consolidation) of the packed beds/cakes.





---

## Kurzfassung

---

Eine Fest-Flüssig-Trennung kann über die Ablagerung der festen Phase (Partikel) im Filtermedium oder die Ablagerung der festen Phase auf der Oberfläche des Filtermedium (Filterkuchen) erreicht werden. Kuchenfiltration wird in vielen industriellen Prozessen benutzt um große Mengen an Feststoff zurückzugewinnen bzw. Suspensionen mit hohem Feststoffgehalt zu filtrieren. Die vorliegende Arbeit untersucht die Filterkuchenbildung mit der Hilfe von DEM-CFD Simulationen. Dabei werden die Modellparameter mit Experimenten kalibriert.

In den bisherigen experimentellen Arbeiten, die in der Literatur zu finden sind, mangelt es an Informationen über die Partikelinteraktionsparameter (Reibungskoeffizient und Stoßzahl). Ein Ziel der vorliegenden Arbeit ist die experimentelle Ermittlung dieser Parameter. Die numerische Analyse wird in dieser Arbeit mittels eines *Volumen-gemittelten und Zweiwege-gekoppelten Ansatzes zwischen DEM und CFD* durchgeführt. Für die numerische Analyse von bidispersen sphärischen und nicht-sphärischen Partikeln werden geeignete Widerstandsmodelle implementiert und validiert. Danach wird eine Sensitivitätsanalyse für verschiedene Einflussfaktoren der Filterkuchen-/Schüttungsstruktur durchgeführt. Außerdem wird die strömungsinduzierte Verdichtung des Filterkuchens untersucht.

Die wesentlichen Ergebnisse der Arbeit sind: Die Erhöhung des Reibungskoeffizienten und der Adhäsionsarbeit neigt dazu die Porosität des Kuchens/der Schüttung zu erhöhen. Bei bidispersen Partikeln vergrößert sich der Druckabfall, wenn der Massenanteil der großen Partikel erhöht wird. Die Porosität erhöht sich beim Verringern der Sphärizität. Außerdem können die Korrelationen zwischen der Porosität und der Reynolds-Zahl genutzt werden um die Änderung in der Porosität des Kuchens/der Schüttung bei Verdichtung vorauszusagen.



---

## Acknowledgements

---

This PhD thesis is a fruitful outcome of the research journey embarked at the Technische Universität and the Fraunhofer ITWM in October 2014. The journey would not have been possible without direct and indirect support of many individuals. Therefore, I would like to take this opportunity to acknowledge a few of them.

First of all, I would like to express my deep gratitude to Prof. Dr.-Ing. Sergiy Antonyuk for supervising the thesis at the Technische Universität Kaiserslautern. He copiously commented on my drafts and unstintingly helped me to solve technical difficulties related to the thesis.

I am deeply grateful to Prof. Dr. Oleg Iliev, for supervising the research at the Fraunhofer ITWM. His constant encouragement, constructive comments and sharp eye for the details has contributed in improving the quality of this thesis.

I am indebted to Mr. Fabian Krull and Mr. Dominik Weis for their suggestions and support in performing the experiments at the Technische Universität Kaiserslautern.

A special thanks to Dr. Sebastian Osterroth for helping with the German translation of the abstract.

Many-thanks to the current and the past members of the Strömungs- und Materialsimulation (SMS) department at the Fraunhofer ITWM for providing a positive work environment.

Last but not the least, I would like to thank my parents (*Aai* and *Baba*) for their unconditional love and support.



---

## Contents

---

<b>Abstract.....</b>	<b>i</b>
<b>Kurzfassung.....</b>	<b>iii</b>
<b>Acknowledgements .....</b>	<b>v</b>
<b>List of Figures.....</b>	<b>xiii</b>
<b>List of Tables .....</b>	<b>xvii</b>
<b>1 Introduction.....</b>	<b>1</b>
1.1 Motivation .....	1
1.2 Basic terminologies .....	2
1.2.1 Packed bed/filter cake .....	2
1.2.2 Consolidation .....	3
1.2.3 Void fraction .....	3
1.2.4 Discrete Element Method (DEM) .....	3
1.2.5 Computational Fluid Dynamics (CFD).....	4
1.2.6 Two-way coupling .....	5
1.2.7 DEM-CFD coupling.....	5
1.2.8 Dilute/dense suspension.....	5
1.3 Literature survey .....	6
1.4 Experimental studies .....	6
1.4.1.1 Macroscopic properties.....	6
1.4.1.2 Microscopic properties .....	7
1.4.2 Numerical studies.....	7

1.4.2.1	Studies using the Eulerian-Eulerian approach .....	8
1.4.2.2	Studies using the Eulerian-Lagrangian approach .....	8
1.4.2.3	Numerical codes.....	10
1.5	Scope and goals of the thesis.....	10
1.5.1	Scope .....	10
1.5.2	Goals.....	11
1.5.3	Measurement of the particle-particle interaction parameters .....	11
1.5.4	Implementation and validation of the drag models .....	11
1.5.5	Numerical analysis of the packed bed/cake .....	11
1.5.5.1	Sensitivity of the particle-particle interaction parameters .....	11
1.5.5.2	Consolidation due to the fluid forces .....	11
1.6	Structure of the thesis .....	12
<b>2</b>	<b>Mathematical Modeling.....</b>	<b>15</b>
2.1	Introduction .....	15
2.2	Eulerian-Eulerian formulation.....	15
2.2.1	Fluid phase .....	16
2.2.2	Particulate phase.....	16
2.2.3	Limitations .....	16
2.3	Eulerian-Lagrangian formulation.....	17
2.3.1	Model A/B.....	18
2.3.2	Pressure gradient force .....	18
2.3.3	Shear stress force.....	20
2.3.4	Drag force.....	20
2.3.4.1	Spherical particles .....	20
2.3.4.2	Non-spherical particles .....	22
2.4	Lagrangian formulation.....	26
2.4.1	Lubrication force .....	27
2.4.2	DEM soft-sphere modelling .....	28
2.4.2.1	Normal contact force.....	30
2.4.2.2	Tangential contact force.....	31

2.4.2.3	Torque due to tangential contact forces .....	32
2.4.2.4	Resistive rolling angular momentum .....	33
2.4.2.5	Attractive forces .....	33
2.4.3	Multi-sphere DEM modeling .....	34
2.4.3.1	Basic properties .....	35
2.4.3.2	Contact forces .....	36
2.4.3.3	Contact torques .....	37
2.5	Time steps .....	37
2.5.1	Eulerian phase time steps .....	38
2.5.1.1	Courant-Friedrich-Levy (CFL) number .....	38
2.5.1.2	Particle momentum response .....	38
2.5.2	Lagrangian phase time steps .....	39
2.5.2.1	Rayleigh time step .....	39
2.5.2.2	Hertzian time step .....	39
2.6	Void fraction calculation .....	40
2.6.1	Spherical mono-dispersed .....	40
2.6.2	Spherical bi-dispersed .....	41
2.6.3	Non-spherical mono-dispersed .....	42
2.7	FVM numerical solver .....	42
2.8	DEM numerical solver .....	43
2.9	Limitations .....	44
<b>3</b>	<b>Experimental Studies .....</b>	<b>45</b>
3.1	Introduction .....	45
3.2	Coefficient of restitution .....	45
3.2.1	Experimental setup .....	46
3.2.2	Procedure .....	47
3.2.3	Validation .....	49
3.2.4	Sources of error .....	51
3.2.5	Results and discussion .....	51



3.3	Coefficient of sliding friction .....	52
3.3.1	Experimental setup .....	53
3.3.2	Procedure .....	54
3.3.3	Sources of error .....	55
3.3.4	Results and discussion .....	55
<b>4</b>	<b>Numerical Studies .....</b>	<b>59</b>
4.1	Introduction .....	59
4.2	Simulation setup .....	59
4.2.1	Domain configuration, boundary and initial conditions .....	60
4.2.2	Initial condition of the particles .....	60
4.3	Spherical particles .....	62
4.3.1	Fluid cell size effect .....	62
4.3.1.1	Particle momentum response .....	62
4.3.1.2	Volume averaging of the properties .....	63
4.3.2	Lubrication force .....	65
4.3.3	Sedimentation of mon-dispersed particles .....	66
4.3.3.1	Effects of the input parameters .....	66
4.3.3.2	Effects of the Young's modulus .....	67
4.3.3.3	Effects of the coefficient of restitution .....	68
4.3.3.4	Effects of the coefficient of frictions .....	69
4.3.3.5	Effect of the attractive forces .....	72
4.3.3.6	Consolidation due to the fluid forces .....	75
4.3.4	Sedimentation of the bi-dispersed particles .....	79
4.3.4.1	Effects of the mass fraction and the attractive forces .....	79
4.3.4.2	Consolidation due to the fluid forces .....	83
4.4	Non-spherical particles .....	87
4.4.1	Single particle .....	87
4.4.1.1	Validation .....	87
4.4.2	Sedimentation of the non-spherical suspensions .....	90
4.4.2.1	Validation .....	90

4.4.3	Effect of the sphericity and friction .....	92
4.4.4	Effect of the initial orientation .....	94
4.4.5	Consolidation due to the fluid forces .....	95
<b>5</b>	<b>Summary and Conclusions.....</b>	<b>99</b>
5.1	Summary .....	99
5.2	Conclusions .....	100
5.3	Recommendations for future work.....	102
	<b>Annexure.....</b>	<b>103</b>
A.1	Coefficient of sliding friction based on the measured shear forces .	103
	<b>Bibliography .....</b>	<b>107</b>
	<b>Index.....</b>	<b>123</b>
	<b>Publications .....</b>	<b>125</b>
	<b>Curriculum Vitae .....</b>	<b>127</b>
	<b>Lebenslauf.....</b>	<b>129</b>



---

## List of Figures

---

Fig. 1.1	Various stages of the cake filtration/formation process.....	2
Fig. 2.1	Graphical representation of the Eulerian-Eulerian continuous phases assumption.....	15
Fig. 2.2	Graphical representation of the different scales in the volume averaged Eulerian-Lagrangian formulations.....	17
Fig. 2.3	Graphical representation of the Archimedes force, the fluid acceleration force, the shear stress and the gravitational force acting on a particle. ....	19
Fig. 2.4	A non-spherical particle generated from two overlapping spherical sub-elements in a CFD fluid cell and the projected area diameters on the corresponding planes.....	24
Fig. 2.5	Imaginary spheres surrounding the particles.....	28
Fig. 2.6	Graphical representation of the notations used in the DEM soft-sphere modelling.....	29
Fig. 2.7	Graphical representation of the notations used in the DEM multi-sphere modelling. ....	35
Fig. 2.8	Graphical representation of the different regions in the divided void fraction model. ....	41
Fig. 3.1	Schematic of the experimental setup to measure the coefficient of restitution.....	47
Fig. 3.2	Frames recorded by the camera for a zirconium dioxide particle ( $d_p = 442.37 \mu\text{m}$ ) in water.....	48
Fig. 3.3	Measured velocity of a zirconium dioxide particle in water ( $d_p = 442.37 \mu\text{m}$ ).....	49

Fig. 3.4	Comparison of the experimentally measured terminal velocity with the terminal velocity predicted by the Eq. 3.4.....	50
Fig. 3.5	Variation in the coefficient of restitution with respect to the Stokes number.....	50
Fig. 3.6	Schematic of the experimental setup to measure the sliding coefficient.....	53
Fig. 3.7	Top view of the top open box and the top plate. ....	54
Fig. 3.8	Top plate with glued zirconium dioxide particles ( $d_p = 250 \mu\text{m}$ ).....	55
Fig. 3.9	A typical shear force displacement curve for the particle (zirconium dioxide $d_p = 1000 \mu\text{m}$ ) -plate in a wet contact. ....	56
Fig. 4.1	The computational domain, the initial conditions and the boundary conditions for the particle and the fluid domain.....	61
Fig. 4.2	Effect of the fluid size on the terminal velocity of a particle. ....	63
Fig. 4.3	Comparison of the normal restitution predicted by the DEM-CFD with the experimental measurements. ....	66
Fig. 4.4	The effect of the coefficients of sliding ( $\mu_s$ ) and rolling ( $\mu_r$ ) friction on the void fraction ( $\varepsilon$ ) of a filter cake. ....	70
Fig. 4.5	Fit of the model in Eq. 4.3 to the DEM-CFD simulation results. ....	72
Fig. 4.6	Variation of the void fraction and the mean coordination number with respect to the cohesion number. ....	73
Fig. 4.7	The frequency distribution of the coordination number.....	74
Fig. 4.8	Force network of the packed beds/cakes.....	75
Fig. 4.9	Comparison of the pressure drop obtained with the DEM-CFD simulations, Ergun equation with dry void fraction (0.41) and with void fraction predicted by DEM-CFD simulations and Eq. 4.8.....	76
Fig. 4.10	Effect of the fluid flow condition and the coefficient of sliding friction on the consolidation of the packed bed/cake .....	78
Fig. 4.11	The effect of the mass fraction ratio, the coefficient of sliding friction and the attractive force on the void fraction.....	81
Fig. 4.12	Final state of the sedimented mono and bi-dispersed particles with coefficient of friction set to 0.6. ....	82

---

Fig. 4.13	Effect of the particle mass fraction ratio on the void fraction of the dry packed beds/cakes.....	84
Fig. 4.14	Effect of the particle mass fraction ratio and the Reynolds number on the pressure drop per unit height.....	84
Fig. 4.15	Effect of the particle mass fraction ratio and the Reynolds number on the void fraction of the filter cakes. ....	85
Fig. 4.16	Variation in the projected diameter of the particle A over time.....	88
Fig. 4.17	Variation in the projected diameter of the particle B over time.....	89
Fig. 4.18	Graphical representation of the spherical (C) and non-spherical (D, E) particles. ....	90
Fig. 4.19	Effect of the sphericity and the coefficient of sliding friction on the void fraction. ....	93
Fig. 4.20	Final stage of the packed beds/cakes with the coefficient of sliding friction as 0.6.....	93
Fig. 4.21	Different initial orientations and the corresponding void fraction of the particle D.....	94
Fig. 4.22	Different initial orientations and the corresponding void fraction of the particle E. ....	95
Fig. 4.23	Effect of the sphericity on the pressure drop and the effect of the flow conditions on the consolidation.....	97



---

## List of Tables

---

Table 3.1	Summary of the experimentally measured coefficient of the sliding friction. ....	56
Table 4.1	Fluid phase boundary conditions .....	61
Table 4.2	Simulation parameters used in the study to investigate the effect of cell size on the volume averaged properties.....	64
Table 4.3	Effect of the fluid cell size to the particle size ratio on the pressure drop predicted DEM-CFD simulations .....	64
Table 4.4	Simulation parameters used in the study to investigate the effect of the Young's modulus on the void fraction of packed beds. ....	68
Table 4.5	Effect of the coefficient of restitution on the void fraction and the computation time.....	69
Table 4.6	Simulation parameters used in the study to investigate the effect of friction coefficients on the void fraction of the mono-dispersed glass particles .....	69
Table 4.7	The particle parameters to study the effect of attractive force.....	79
Table 4.8	The particle and the fluid properties used to study the bi-dispersed filter cake.....	83
Table 4.9	Particle properties of non-spherical particles.....	87
Table 4.10	Terminal velocity of non-spherical particles.....	88
Table 4.11	Properties of non-spherical particles.....	90
Table 4.12	Non-spherical parameters varied in the study.....	91
Table 4.13	Terminal velocity of suspensions.....	92
Table 4.14	Variation of pressure drop and void fraction with respect to the sphericity.....	96



Table A.1	Measured particle-plate dry contact coefficient of the sliding friction.	103
Table A.2	Measured particle-plate wet contact coefficient of the sliding friction.	104
Table A.3	Measured particle-particle dry contact coefficient of the sliding friction. ....	104
Table A.4	Measured particle-particle wet contact coefficient of the sliding friction. ....	105

---

# 1 Introduction

---

## 1.1 Motivation

Filtration is the process of separating one phase from the other phase with the help of a filtering (porous) medium.<sup>1</sup> The solid-fluid separation can be realized by the deposition of the dispersed solid phase (particles) within the filtering medium (depth filtration) or by the deposition of the solid phase on the surface of the filtering medium (cake formation). The empirical  $1/3^{\text{rd}}$  law suggests that the cake formation is observed when the particle size is bigger than  $1/3^{\text{rd}}$  of the size of the pores.<sup>1-3</sup> In the cake filtration, the deposited particles itself act as a filtering medium for the other particles.

The Fig. 1.1 illustrates the details of the cake and the depth filtration.<sup>4</sup> It starts with the particle suspension approaching the filter (porous) media (Fig. 1.1a). The particles which are smaller than the pores travel inside the filtering media. The particles larger than  $1/3^{\text{rd}}$  the pore size, start depositing on the surface of the filtering medium forming a filter cake (Fig. 1.1b-c). After some time only a few smaller particles can pass through the formed cake and the rest of the particles contribute to the cake growth (Fig. 1.1c-d). This process continues to a point where the pressure drop across the deposited particles is within the practical constraints (the economical and the design).<sup>5</sup>

The process of cake filtration is used in many process industries (mineral, chemical, food, pharmaceuticals, and petroleum) where large quantities of solids are to be recovered/filtered.<sup>5,6</sup> In fact, cake filtration is employed more often than the depth filtration.<sup>7</sup> Therefore, the present study is dedicated to the investigation of the filter cake formation process using DEM-CFD simulation with experimentally calibrated parameters.

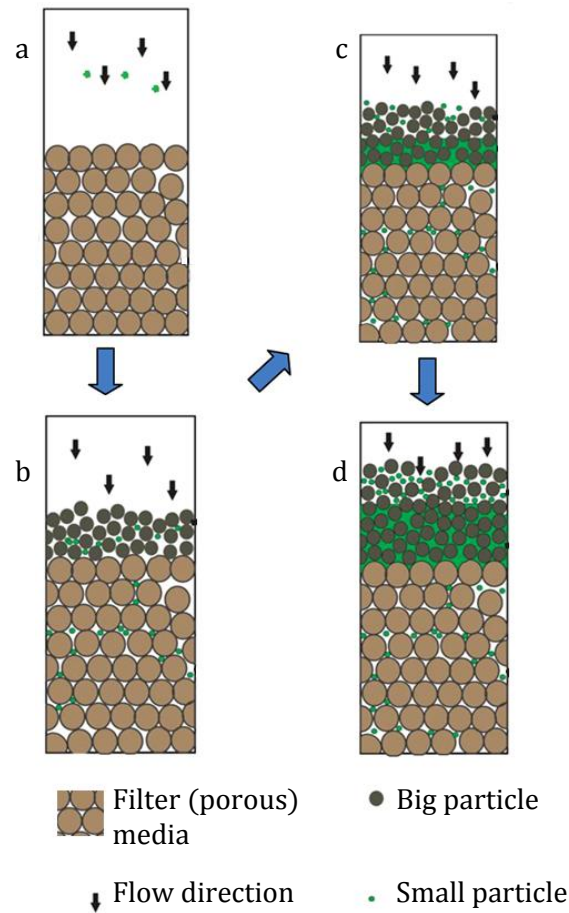


Fig. 1.1 Various stages of the cake filtration/formation process.

Original figure by Sacramento et. al.<sup>4</sup> reproduced with permission from Elsevier.

## 1.2 Basic terminologies

The basic terminologies used in this study are discussed in the following sub-sections.

### 1.2.1 Packed bed/filter cake

Wakao and Kagei<sup>8</sup> have defined a packed bed as *a heterogeneous system composed of solid particles and the fluid is flowing through the interstitial space between the particles*. In a filter cake, the fluid flows through the gaps between the particles which are piled up on the surface of a filtering medium.<sup>9</sup> Due to this similarity, the packed beds and the filter cakes are used as alternative terms to each other.

### 1.2.2 Consolidation

The particles rearrange their positions when the external forces (fluid/mechanical/electrostatic) are sufficient to overcome the particle-particle resistance (friction + cohesion/adhesion). This reduces the original void fraction which is termed as the consolidation of a packed bed/cake.<sup>2</sup> The consolidation can be quantified by measuring the decrease in the height, the non-linear behavior of the pressure drop or the mass flow rate across a packed bed/cake. Due to the external forces the particles (e.g. clay) itself can undergo change in the shape and size (deformation and breakage). This can also change the void fraction of the packed bed/cake.<sup>10</sup> The later scenarios are not considered in the present study.

### 1.2.3 Void fraction

Void fraction ( $\epsilon$ ), voidage, free volume or porosity is defined as the ratio of the fluid volume present in the region of interest to the total volume of that region.<sup>7,11–13</sup> In the context of the packed bed/cake, void fraction is one of the parameters which defines its physical structure. Whereas, in the mathematical modeling of the particle-fluid systems, it is a key parameter for determining the particle/fluid velocities and the inter-phase exchange (source) terms.

### 1.2.4 Discrete Element Method (DEM)

The Discrete Element Method<sup>14</sup> also known as the Distinct Element Method<sup>15</sup> (DEM) is a modelling approach in which the behavior of a system comprising of a large number of discrete/distinct bodies (elements) with arbitrary shapes can be studied.<sup>11,16</sup> It is a sub-set of the Lagrangian formulation where the motion of bodies are tracked using the Newton's laws of motion.

The DEM is employed in the scenarios where the impact between the bodies is non-elastic and/or there are considerable energy losses due to friction and other surface energies (cohesion/adhesion). Based on the physics and the computational resources either the *Hard-sphere*<sup>17</sup> or the *Soft-sphere*<sup>18</sup> DEM formulation could be used. The *Hard-sphere* DEM formulation is computationally efficient if there are two bodies in contact (binary contact). Such binary contacts are expected in the dilute flows. The *Soft-sphere* DEM formulation does not have any such restrictions and is applicable for

any number of simultaneous contacts.<sup>19</sup> In this study, DEM refers to the *Soft-sphere* formulation where an overlap between the contact surfaces, calculated based on contact models is used to predict the contact dynamics. Further details of the *Soft-sphere* formulation are presented in the sec. 2.4.2.

The *Soft-sphere* DEM can be extended to the non-spherical particles by using the following approaches.

1. The single element approach:

In the single element approach, the surface of the particle is represented by a set of equations. Different particle shapes can be generated by changing the parameters in these equations. The contact detection is the most challenging issue in the use of this approach. It requires solving a set of non-linear equations. For a flat surface, a large number of iterations are required. Whereas, sharp edges (corners) cannot be represented as the contact detection algorithm may have convergence issues.<sup>11,20</sup>

2. The multi-element approach:

The multi-element approach uses a number of sub-elements to construct a non-spherical particle.<sup>21–24</sup> If spheres are used as sub-elements, it is termed as the multi-sphere approach. Theoretically, by controlling the sub-spheres (the size and the position) any desired shape can be generated. In this approach, the contact detection algorithm and the force calculations are similar to spherical particles. Thus a DEM code with the capabilities to simulate spherical particles can be modified to incorporate the multi-sphere approach.<sup>14,25</sup> This is the approach used in this study. The mathematical details of this approach are presented in the sec. 2.4.3.

### 1.2.5 Computational Fluid Dynamics (CFD)

As defined by Versteeg and Malasekera<sup>26</sup> *Computational fluid dynamics (CFD) is the analysis of the systems involving fluid flow, heat transfer and associated phenomena such as chemical reactions by means of computer-based simulation.*

Here, the fluid governing equations (mass, momentum, energy, species conservation) are represented by a set of Partial Differential Equations (PDE's).<sup>27</sup> A numerical solution to the governing PDE's can be obtained by choosing a suitable discretization method. The Finite Difference Method<sup>28</sup> (FDM), the Finite Volume Method<sup>29</sup> (FVM),

and the Finite Element Method<sup>30</sup> (FEM) are a few commonly used discretization methods.<sup>31–34</sup> In this study, we restrict our discussions to the FVM.<sup>29</sup>

### 1.2.6 Two-way coupling

In the literature,<sup>11,35,36</sup> the one/two-way coupling refers to the strategy used for computing the solution to a particle-fluid system. The cardinal assumption of the one-way coupling strategy is that the fluid phase is immune to the particle phase. Whereas, in the two-way coupling there is no such assumption and the mutual-effects are considered.<sup>11</sup> The mathematical modelling of two-way coupling strategy is presented in the Chapter 2.

### 1.2.7 DEM-CFD coupling

Strictly speaking, the DEM can be either coupled with the FDM, the FVM, the FEM, etc. In the literature, these couplings are simply referred to as the DEM-CFD<sup>37–39</sup> or the CFD-DEM<sup>11,40,41</sup> coupling. In this study the DEM-CFD convention is used. This is because the numerical code used here is initiated by a DEM solver followed a two-way coupling with a CFD (FVM) solver.<sup>31,42,43</sup> The details of the solvers are provided in the sec. 2.7 and 2.8.

### 1.2.8 Dilute/dense suspension

In this section, the criteria used for differentiating a dilute particle suspension from a dense particle suspension are discussed.

#### 1. Collision:

If the ratio of the momentum response time of a particle to the time between the collisions is less than 1, then the suspension is classified as a dilute suspension. The momentum response time and the time between the collisions are dependent on the particle diameter, the number of particles, and the velocity.<sup>35</sup> There is no definite scaling parameter (e.g. void fraction) that can define a boundary between a dilute and a dense suspension.

#### 2. Semi-empirical drag correlations:

In the literature, there are a few semi-empirical drag correlations which are valid for the dilute or the dense suspensions. Gidaspow<sup>44,45</sup> has suggested that the Wen and Yu drag correlation<sup>46</sup> can be used for void fraction greater than 0.8. Whereas,

for a void fraction less than 0.8, the Ergun drag correlation<sup>47</sup> can be used. In this study, this criterion is used to differentiate the dilute suspensions from the dense suspensions.

### 1.3 Literature survey

Ruth et. al.<sup>48,49</sup> were the pioneers in the study of the packed bed/cake formation process and have proposed the classical packed bed/cake formation theory. Since then, there have been many successful attempts to study the packed bed/cake formation processes. The widely accepted theories proposed by Tien<sup>1</sup> and Tiller et. al.<sup>50-54</sup> are based on the following assumptions.

1. The packed bed/cake has uniform and ordered structure.
2. There are no variations (consolidation) in the already formed layers of the packed bed/cake.
3. The flow through the packed beds/cakes follows the Darcy law.<sup>55</sup>

Due to these assumptions, the theories are applicable to ideal packed beds/cakes. In order to extend the understanding of the real packed bed/cake formation process, researchers have explored the experimental<sup>56-59</sup> and the numerical<sup>60-65</sup> approaches. A brief review of this is presented in the following sub-sections.

### 1.4 Experimental studies

#### 1.4.1.1 Macroscopic properties

Most of the experimental studies in the literature have analyzed the macroscopic properties (void fraction, pressure drop, mass flow rate) of the packed beds/cakes. The experimental studies by Scott and Kilgour<sup>56</sup> have reported that the random loose void fraction of a dry (absence of fluid forces) packed bed/cake formed due to sedimentation of mono-dispersed glass particles ( $d_p = 250 \mu\text{m}$ ) is 0.4. Similar sedimentation experiments by Onoda and Liniger<sup>57</sup> have shown that the presence of the fluid increases the void fraction (0.43). Shapiro and Probstein<sup>58</sup> have shown that the void fraction of the packed bed/cake formed due to the sedimentation of the bi-dispersed particles is affected by the particle mass fraction ratio and the particle size ratio. Brod-

key and Hershey<sup>59</sup> have reported that the void fraction of the packed bed/cake is affected by the sphericity of the particles. Studies in the literature<sup>1,66–68</sup> have implied that consolidation of the packed bed/cake is a widely occurring phenomena.

#### 1.4.1.2 Microscopic properties

In the context of the packed bed/cake, the literature lacks the information about the microscopic particle-particle interaction properties in the presence of a liquid. The important microscopic properties are, the coefficient of restitution, the coefficient of frictions, and the work of adhesion.

There are a few independent attempts in the literature<sup>69–73</sup> to measure the coefficient of restitution in the presence of a liquid. The particle sizes used in these studies are greater than 1000  $\mu\text{m}$ . This is much larger than the particle sizes usually encountered in the cake formation process.

There are large datasets<sup>74,75</sup> available for the coefficient of friction in the dry conditions. The study by Joseph and Hunt<sup>72</sup> is the only known attempt to quantify the influence of a surrounding fluid on the values of the coefficient of frictions.

The work of adhesion is an important microscopic parameter affecting the structure of the packed bed/cake. Measuring the work of adhesion is very challenging and is sensitive to the measurement technique.<sup>76</sup> Further, it also depends on the method in which the fluid is added. If the fluid is added to the initially dry assembly of the spheres, the decrease in the work of adhesion is significantly lower than the cases in which the solution is vigorously stirred or when the spheres are added individually to a aqueous solution.<sup>77</sup>

The other microscopic properties like the size, size distribution and shape of the particles can be measured using various digital measurement techniques.<sup>78–80</sup>

#### 1.4.2 Numerical studies

The numerical studies in the literature are either based on the Eulerian-Eulerian or the Eulerian-Lagrangian approach. A brief review of the studies in the literature is presented in the following sub-sections.



### 1.4.2.1 Studies using the Eulerian-Eulerian approach

In the literature, the packed bed/cake formation process was studied by a very few researchers using the Eulerian-Eulerian approach.<sup>65,81,82</sup> In these studies, it was assumed that, the particle phase could be modelled as a continuous phase and the particle-particle/wall impulse transfer could be considered using some constitutive laws. The major challenges in the use of the Eulerian-Eulerian formulation are the availability of the constitutive laws, tracking the growth of the filter cake (moving boundary), and the breakdown of the continuous phase assumption in the dilute flow. Further, the particle-level details like the shape, the size distribution, the adhesion, the consolidation and the clustering are difficult to incorporate in the Eulerian-Eulerian approach.

### 1.4.2.2 Studies using the Eulerian-Lagrangian approach

Studies<sup>60–63</sup> have shown that Eulerian-Lagrangian approach could be used to overcome the limitations of the Eulerian-Eulerian approach. The particle-particle/wall interactions can be modelled using the Lagrangian approach (DEM).<sup>18</sup> The one-way coupling fails in the cases where the void fraction is not very high ( $\varepsilon < 0.9$ ).<sup>11</sup> The void fraction of the sedimenting solution and the corresponding packed bed/cake is low ( $0.3 \leq \varepsilon \leq 0.9$ ).<sup>1,2</sup> Hence, along with the particle-particle/wall interaction, the two-way particle-fluid interactions must be considered. The two-way coupling between the Eulerian and the Lagrangian phases could be carried out by using either the *resolved (fictitious domain) coupling approach* or the *volume averaged coupling approach*.<sup>11,41,83–85</sup>

In the *resolved coupling approach*, the interphase momentum exchange (source) term is calculated by integrating the viscous stress tensor over the surface of the particle.<sup>11,84,86</sup> Hence, no additional relations (drag laws) are needed for the closure in the Eulerian-Lagrangian formulation. In this approach, the control volumes occupied by the particles are marked as solids and the fluid governing equations are solved in remaining control volumes. The size of the control volume must be small enough to capture the surface of the particle within the acceptable accuracy. This leads to a very high computational effort and only a few particles can be considered in the simulations. In the packed beds/cakes there a large number of particles and the use of the *resolved coupling approach* is not practical.<sup>11,43,84</sup>

In the *volume averaged coupling approach*, the particles are smaller than the control volume used for the discretization of the fluid domain. Semi-empirical drag laws are used to have a closure between the Eulerian (fluid) and the Lagrangian (particle) phase.<sup>11,87</sup> Studies in the literature have shown that this approach can be used to analyze the systems with a large number of particles.<sup>38,88,89</sup> In the context of the packed beds/cakes very few attempts were made using the *volume averaged coupling approach*.<sup>60–62</sup> These studies were limited to the mono-dispersed particles and lack the complete 3D modelling.

Nevertheless, these studies have shown that the *two-way volume averaged coupling approach between the DEM and the CFD* is a promising approach to study the various aspects of the packed beds/cakes. This is the approach used in this study and the details are presented in the sec. 2.3.

### *Drag correlations*

The major challenge in the use of the *volume averaged coupling approach*, is the calculation of the fluid drag force on the particles. There are a large number of semi-empirical correlations to calculate the drag force on the mono-dispersed particles.<sup>46,47,90–92</sup> However, applying these models for a poly-dispersed particle system may result in an error up to 300 %.<sup>93–95</sup> Based on the literature survey, the Beetstra drag<sup>93,96</sup> model is identified as a suitable drag model for spherical, poly-dispersed particles. Further, in comparison to the other models, its implementation is relatively easy.<sup>11</sup> The details of the Beetstra drag<sup>93,96</sup> model are presented in the sec. 2.3.4.1.

For the non-spherical particles, the particle orientation, sphericity and the effect of the surrounding particles (similar to spherical particles) are important and must be incorporated in the drag force calculation. In the Lu, Wei and Wei<sup>97</sup> drag model all these factors are considered. Unlike the other non-spherical drag model,<sup>98–101</sup> the Lu, Wei and Wei<sup>97</sup> drag model considers the presence of the surrounding particles even in dilute phase. Similar to the Gidaspow drag model,<sup>46,47</sup> the Lu, Wei and Wei<sup>97</sup> model has a discontinuity at the void fraction of 0.8. A switch function can be used to smoothen the discontinuity.<sup>45</sup> This model is used in this study when non-spherical particles are considered and the details are discussed in sec. 2.3.4.2.

### 1.4.2.3 Numerical codes

Developing a robust numerical code from scratch with a *volume averaged two way coupling between the DEM and the CFD* demands a huge effort. Therefore, the survey of the already available numerical codes was carried out. It should be noted that numerical codes are constantly evolving with respect to the computational/model capabilities and the discussion here is based on the survey done at the start of this study (in October 2014).

The commercially supported codes EDEM-Fluent,<sup>32,102</sup> and STAR CCM+<sup>103</sup> and the open source codes MFiX,<sup>104</sup> and LIGGGHTS-OpenFOAM (CFDEM)<sup>31,42,43</sup> were the available options. They had similar capabilities and were based on the same mathematical models. They all lacked two way coupling suitable for the poly-dispersed and non-spherical particle-fluid systems.

Among the available open source codes, LIGGGHTS-OpenFOAM (CFDEM)<sup>31,42,43,105</sup> was chosen because, there were a sufficient number of validation proofs for the already available implementations, it had an inherent capability to handle computation with large number of particles, and offered a relative easy access to the source code for its modification and the implementation of new models.

## 1.5 Scope and goals of the thesis

### 1.5.1 Scope

As already stated, the focus of thesis is to study the packed bed/cake formation process using the experimental and numerical tools.

One of the way to classify the packed bed/cake formation is by monitoring the fluid pressure drop and/or the fluid velocity (mass flow rate). A constant pressure drop can be maintained across an evolving cake by using an actuating mechanism or a vacuum pump. In this case, the fluid mass flow rate across the filter cake varies. A constant inlet fluid velocity can be employed by using a positive displacement pump. This results in the variation of the pressure drop across the filter cake.<sup>7</sup> Gravitational force (sedimentation) can also be used to carry out the cake filtration.<sup>54</sup>

The structure of the packed bed/cake is dependent on the size, the size distribution, the shape and the microscopic particle-particle interaction parameters. Further, the change

in fluid conditions can lead to the consolidation of the packed bed/cake. The scope of this thesis is limited to the study of the above listed factors under the constant inlet fluid velocity and the sedimentation conditions.

### **1.5.2 Goals**

The major goals of the thesis are as follows:

### **1.5.3 Measurement of the particle-particle interaction parameters**

For the micron sized particles in a fluid, the literature lacks the information about the particle-particle/wall interaction parameters (coefficients of the restitution and frictions). Experimental measurement of these parameters is the first major goal of this thesis. The information from the experimental studies serves as an input to the numerical studies.

### **1.5.4 Implementation and validation of the drag models**

For performing the numerical analysis an appropriate drag model must be used in the volume averaged two-way coupling. Based on the literature survey the Beetstra<sup>93,96</sup> and the Lu, Wei and Wei<sup>97</sup> drag models are identified as the most suitable drag models for the mono/poly-dispersed, spherical particles and the mono-dispersed, non-spherical particles, respectively.

These drag models were not readily available in any of the numerical codes. The implementation and the validation of these drag models is the second goal of this thesis.

### **1.5.5 Numerical analysis of the packed bed/cake**

#### **1.5.5.1 Sensitivity of the particle-particle interaction parameters**

One of the goals of the numerical studies is to perform the sensitivity analysis of particle-particle interaction parameters using the experimental studies as the reference cases.

#### **1.5.5.2 Consolidation due to the fluid forces**

The other aim of the numerical analysis is to study the phenomenon of the consolidation due to the fluid forces. Here the goal is to answer the questions like, at what Reynolds number the already formed packed bed/cake undergoes consolidation? What is

the influence of the factors like the adhesion, the particle size, the mass fraction ratio, the sphericity, the orientation, etc. on the consolidation of the packed bed/cake?

## 1.6 Structure of the thesis

Chapter 1 is the introductory chapter of this thesis. The motivation, the basic terminologies, and the literature survey related to the study of the packed bed/cake formation is presented. The scope and the major goals of the thesis are formulated.

Chapter 2 reports the mathematical models used for the analysis of the packed bed/cake formation. At first the governing equations and the limitations of the Eulerian-Eulerian formulation are presented. This is followed by the mathematical description of the two-way volume averaged Eulerian-Lagrangian formulation. Then, the drag models for the poly-dispersed and the non-spherical particles are presented. After this, the DEM based on the soft-sphere approach for the spherical and the non-spherical particles (multi-sphere) is described in detail. This is followed by a short description of the numerical solvers used in this study.

In the Chapter 3 the details of the experiments performed to measure the particle-particle interaction parameters are presented. The measured parameters are the coefficient of the restitution and the coefficient of the sliding friction in dry and wet conditions. The qualitative values measured in these experiments serve as input parameters in the numerical studies.

In the Chapter 4 the results from the numerical studies are reported. At first the effect of the fluid cell size on the accuracy of the DEM-CFD simulation is presented. After this, the implementation of the lubrication force model is tested by comparing the simulation results to the experimental measurements.

Then, the sensitivity of the various factors affecting the structure of the packed beds/cakes due to spherical mono/bi-dispersed particles is presented. Here, the focus is on the sensitivity of the coefficient of frictions, the work of adhesion, the particle size ratio, the mass fraction, the fluid flow conditions, and the onset of consolidation. The experimental results available in the literature are used for the comparison of the macroscopic properties (void fraction) to obtain a set of realistic values. Then, the effect of the flow conditions (consolidation) on the structure of the packed bed/cake are reported.

Further, numerical studies related to the packed beds/cakes formed due to the non-spherical particles are presented. Here the focus is on the effect of the non-sphericity, the coefficient of friction, the orientation, fluid flow on the packed bed/cake.

In the Chapter 5 the conclusions drawn from the present work are summarized and some recommendations for the future work are proposed.



---

## 2 Mathematical Modeling

---

### 2.1 Introduction

In this Chapter, the mathematical modeling approaches for the two-phase (fluid-particle, particle laden) flows are discussed. As a starting point the Eulerian-Eulerian two phase formulation and its limitations are presented.

This is followed by the description of the volume averaged Eulerian-Lagrangian coupling. The mathematical formulation of the forces acting on the particles due to the fluid are then discussed. Thereafter, the Lagrangian formulation (the soft-sphere DEM approach) for the spherical and the non-spherical particles is described.

Then the Finite Volume Method (FVM) and the DEM solvers used in this study are discussed. The chapter is concluded by presenting the limitations of the Eulerian-Lagrangian formulation implemented in this study.

### 2.2 Eulerian-Eulerian formulation

One of the assumptions of the Eulerian-Eulerian (*“Two overlapping continua”*) approach is that both the phases could be modelled as continuous phases (Fig. 2.1).<sup>11,35</sup>

The mathematical formulations for the fluid and the particle phases based on the Eulerian-Eulerian approach are described in following sub-section.

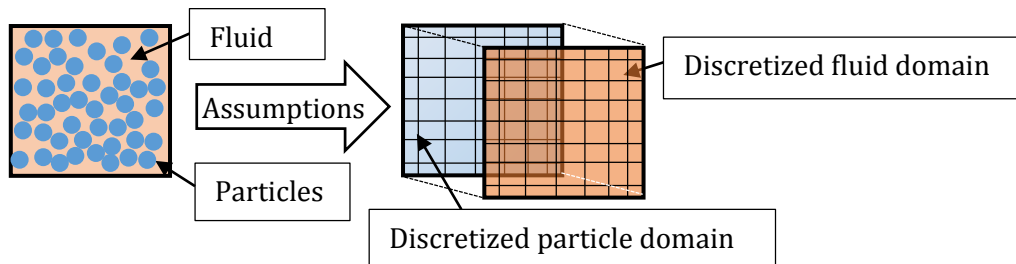


Fig. 2.1 Graphical representation of the Eulerian-Eulerian continuous phases assumption.



### 2.2.1 Fluid phase

The Eqs 2.1 and 2.2 represents the mass and the momentum conservation equations for the fluid phase, respectively.<sup>106</sup>

$$\frac{\partial(\rho_f \varepsilon)}{\partial t} + \nabla \cdot (\rho_f \varepsilon \vec{U}_f) = 0 \quad 2.1$$

$$\frac{\partial(\rho_f \varepsilon \vec{U}_f)}{\partial t} + \nabla \cdot (\rho_f \varepsilon \vec{U}_f \vec{U}_f) = - \nabla(p) - \nabla \cdot (\vec{\tau}_f) + \vec{S}_{pf} + \varepsilon \rho_f \vec{g} \quad 2.2$$

Here,  $\vec{U}_f$ ,  $\rho_f$ ,  $\varepsilon$ ,  $p$ , and  $\vec{\tau}_f$  are the velocity, the density, the fluid void fraction, the pressure, and the shear stress of the fluid phase, respectively. The details of the volume averaged source term due to the particle-fluid interactions ( $\vec{S}_{pf}$ ) are given the sec. 2.3.

### 2.2.2 Particulate phase

The particulate (particle) phase mass and the momentum equations in the Eulerian formulation are given by the Eqs. 2.3 and 2.4, respectively.<sup>106</sup>

$$\frac{\partial(\rho_p(1-\varepsilon))}{\partial t} + \nabla \cdot (\rho_p(1-\varepsilon) \vec{V}) = 0 \quad 2.3$$

$$\frac{\partial(\rho_p(1-\varepsilon) \vec{V})}{\partial t} + \nabla \cdot (\rho_p(1-\varepsilon) \vec{V} \vec{V}) = - \nabla \cdot \vec{\phi}_p - \vec{S}_{pf} + (1-\varepsilon) \rho_p \vec{g} \quad 2.4$$

Here,  $\vec{V}$ ,  $\rho_p$  and  $\vec{\phi}_p$  represents the velocity, the density and the total particle stress tensor (analogous to  $\nabla(p) + \nabla \cdot (\vec{\tau}_f)$ ) of the particulate phase, respectively. Obviously,  $(1-\varepsilon)$  represents the solid volume fraction.

### 2.2.3 Limitations

Several studies have shown that the effects like the clustering and the consolidation of the particulate phase cannot be captured by the Eulerian formulation.<sup>107–110</sup> Lagrangian formulation (sec. 2.4) can be used to capture these particle scale effects.

The void fraction in the packed bed/cake is low ( $0.3 \leq \varepsilon \leq 0.9$ ).<sup>107,111,112</sup> The two-way coupling between the fluid and the particle phase is necessary when the void fraction is low ( $\varepsilon < 0.9$ ). The two-way coupling based on the Eulerian-Lagrangian formulation is presented in the next section.

### 2.3 Eulerian-Lagrangian formulation

In the volume averaged Eulerian-Lagrangian formulation, the solution to the fluid phase is obtained at the fluid cell scale (control volume) whereas the particle-particle/wall interactions are calculated at the individual particle contact scale. Here, the fluid cell size is much larger than the particle size and the volume averaged quantities are used for the particle-fluid coupling (Fig. 2.2).

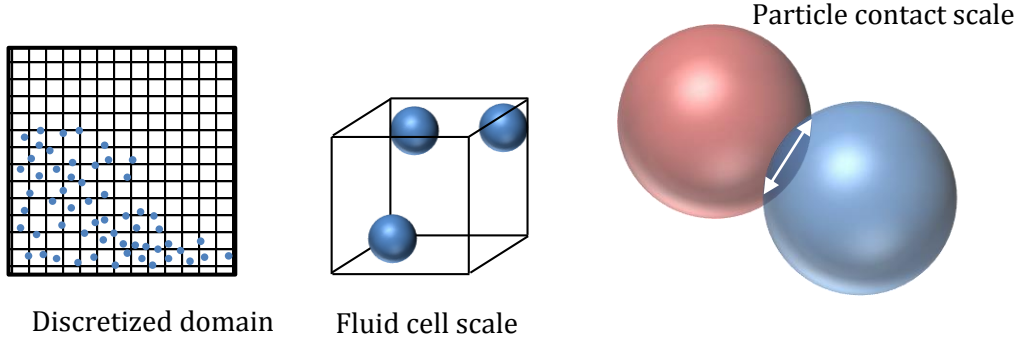


Fig. 2.2 Graphical representation of the different scales in the volume averaged Eulerian-Lagrangian formulations.

$S_{pf}$  which represents the volume average force of all the particle-fluid interaction forces is given by the Eq. 2.5.

$$\vec{S}_{pf} = - \frac{1}{V_{cell}} \left( \sum_{j=1}^{np} \left( \vec{f}_{pg}^j + \vec{f}_{ss}^j + \vec{f}_d^j \right) \right) \quad 2.5$$

Here,  $V_{cell}$  is the volume of the fluid cell and  $np$  is the number of particles in the fluid cell.

The fluid pressure gradient force  $\left(\overrightarrow{f_{pg}^j}, \text{sec. 2.3.2}\right)$  and the shear stress force  $\left(\overrightarrow{f_{ss}^j}, \text{sec. 2.3.3}\right)$  are the macro-level forces whereas the fluid drag force  $\left(\overrightarrow{f_d^j}, \text{sec. 2.3.4}\right)$  is a micro-level force.<sup>11</sup>

### 2.3.1 Model A/B

In the literature *Model A* refers to a formulation where the macro-level forces  $\left(\overrightarrow{f_{pg}^j}\right)$  and  $\left(\overrightarrow{f_{ss}^j}\right)$  are separated from the micro-level forces  $\left(\overrightarrow{f_d^j}\right)$  in the calculation of  $\overrightarrow{S_{pf}}$ . The fluid flow around the particles is unsteady and non-uniform  $\left(\overrightarrow{f_{ss}^j} \neq 0\right)$ . Whereas, *Model B* refers to the formulation where it is assumed that the fluid flow around the particle is steady and uniform  $\left(\overrightarrow{f_{ss}^j} \approx 0\right)$ .<sup>11,44,113–116</sup> Further, *Model A* assumes that the pressure is shared between the fluid and solid phases, while *Model B* assumes it is handled by the fluid phase only.<sup>116</sup>

*Model A* is a generalized formulation and is valid for all the particle-fluid systems whereas the applicability of the *Model B* is not tested for poly-dispersed and non-spherical suspensions.<sup>11,39,117–119</sup> This study is restricted to the mathematical formulation based on the *Model A*.

### 2.3.2 Pressure gradient force

The reasons for considering the pressure gradient force are:

- 1) The variation in the hydrostatic pressure leading to the Archimedes' force  $\left(\overrightarrow{f_a^j}\right)$  which is calculated using the Eq. 2.6.

$$\overrightarrow{f_a^j} = -V_{pj} \rho_f \overrightarrow{g} \quad 2.6$$

Here,  $V_{pj}$  and  $\rho_f$  are the volume of the particle  $j$  and the fluid density, respectively.

- 2) The presence of the fluid acceleration outside the boundary layer surrounding the particle results in the fluid acceleration force  $\left(\overrightarrow{f_{ac}^j}\right)$  given by the Eq. 2.7.

$$\vec{f}_{ac}^j = -V_{pj}\rho_f\vec{U}_f\nabla\cdot\vec{U}_f \quad 2.7$$

Here,  $\vec{U}_f$  is the fluid velocity, and  $\rho_f$  is the fluid density.

The graphical representation of these forces is shown in the Fig. 2.5.

The total pressure gradient force  $\left(\vec{f}_{pg}^j\right)$  acting on a particle in a fluid can be calculated using the pressure (p) gradient as shown in the Eq. 2.8.<sup>106,114,120</sup>

$$\vec{f}_{pg}^j = \vec{f}_a^j + \vec{f}_{ac}^j = -V_{pj}(1 - \epsilon)\nabla(p) \quad 2.8$$

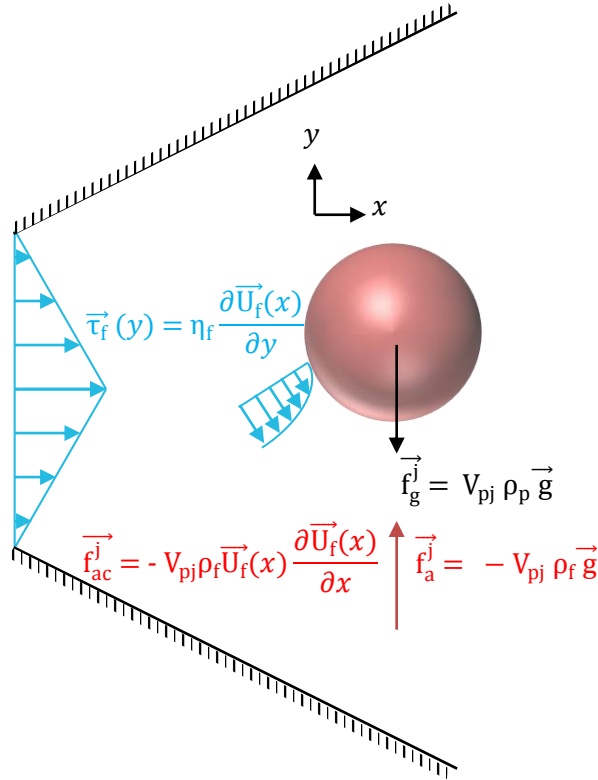


Fig. 2.3 Graphical representation of the Archimedes force, the fluid acceleration force, the shear stress and the gravitational force acting on a particle.

### 2.3.3 Shear stress force

The shear stress force ( $\vec{f}_{ss}^j$ , Fig. 2.5) is due to the viscous nature of the fluid and is given by the Eq. 2.9.<sup>39</sup>

$$\vec{f}_{ss}^j = -V_{pj}(1 - \varepsilon)\nabla \cdot (\vec{\tau}_f) \quad 2.9$$

Here,  $V_{pj}$ ,  $\varepsilon$ , and  $\vec{\tau}_f$  are the volume of the particle  $j$ , the void fraction and the fluid shear stress, respectively.

### 2.3.4 Drag force

The major challenge lies in the modelling of the fluid drag force on the particles. There are a large number of semi-empirical correlations to calculate the drag force on the mono-dispersed particles.<sup>46,47,90–92</sup> However, applying these models for a poly-dispersed particle system may result in an error up to 300%.<sup>93–95</sup>

Further, for the non-spherical particle, the particle orientation, sphericity and the effect of the surrounding particles are important and must be incorporated in the drag model. In the following sub-sections, a generalized poly-dispersed drag model for spherical particles (sec. 2.3.4.1) and a drag model applicable for mono-dispersed, non-spherical particles (sec. 2.3.4.2) are presented.<sup>93,94,96,97</sup>

#### 2.3.4.1 Spherical particles

In this study, the simulations concerning the spherical particles are carried out using the poly-dispersed drag correlation suggested by Beetstra.<sup>93</sup> The drag force on a particle is given by the Eq. 2.10.

$$\vec{f}_d^j = 3\pi\eta_f d_{pj}\beta_j\varepsilon(\vec{U}_f - \vec{V}_j) \quad 2.10$$

Here,  $\eta_f$ ,  $d_{pj}$ , and  $(\vec{U}_f - \vec{V}_j)$  are the dynamic viscosity of the fluid, diameter of the particle and the relative velocity between the fluid and the particle, respectively.

The poly-dispersity correction factor  $\beta_j$  is given by the Eqs. 2.11.

$$\beta_j = \left( \varepsilon y_i + (1 - \varepsilon) y_i^2 + 0.022(1 - \varepsilon)(y_i^2 - y_i) \right) F_j \quad 2.11$$

This expression for  $\beta_j$  is valid until the diameter ratio ( $y_i$ ) given by the Eq. 2.12 is less than 4.

$$y_i = \frac{d_{pi}}{\langle d \rangle} \quad 2.12$$

In the Eq. 2.11,  $F_j$  is calculated using the Eq. 2.13.

$$F_j = 10 \frac{1 - \varepsilon}{\varepsilon^2} + \varepsilon^2 (1 + 1.5\sqrt{1 - \varepsilon}) + \frac{0.413 \langle \text{Re}_p \rangle_j}{24\varepsilon^2} \left( \frac{\varepsilon^{-1} + 3\varepsilon(1 - \varepsilon) + 8.4 \langle \text{Re}_p \rangle_j^{-0.343}}{1 + 10^{3(1 - \varepsilon)} \langle \text{Re}_p \rangle_j^{-0.5 - 2(1 - \varepsilon)}} \right) \quad 2.13$$

The mean Reynolds number ( $\langle \text{Re}_p \rangle_j$ ) is given by the Eq. 2.14.

$$\langle \text{Re}_p \rangle_j = \frac{\varepsilon \rho_f |\vec{U}_f - \vec{V}_j| \langle d \rangle}{\eta_f} \quad 2.14$$

Here, the mass weighted mean particle diameter ( $\langle d \rangle$ ) is given by the Eq. 2.15.

$$\frac{1}{\langle d \rangle} = \sum_{i=1}^k \frac{\chi_i}{d_{pi}} \quad 2.15$$

Here,  $i$  represents the index of the particle fraction corresponding to the diameter  $d_{pi}$  and  $k$  is the number of such different size fractions.

The mass weightage ( $\chi_i$ ) is calculated by using the Eq. 2.16.

$$\chi_i = \frac{\rho_{pi} n_{pi} d_{pi}^3}{\sum_{i=1}^k \rho_{pi} n_{pi} d_{pi}^3} \quad 2.16$$

Here,  $np_i$  is the number of particles in a fluid cell with the diameter  $d_{pi}$  and density  $\rho_{pi}$ .

### 2.3.4.2 Non-spherical particles

According to the Lu, Wei and Wei<sup>97</sup> semi-empirical drag correlation, if the void fraction of the fluid cell is greater than 0.8, a dilute drag correlation (Eq. 2.17) can be used. If the void fraction is less than 0.8 the drag force can be calculated using the Ergun drag equation (Eq. 2.31).

Similar to the Gidaspow drag model<sup>46,47</sup> a switch function can be used to smoothen the discontinuity at the void fraction of 0.8.<sup>45</sup> The details of the drag force in the dilute and the dense flows are described in the following sub-sections.

#### *Dilute flow*

The fluid drag force on a particle  $j$  with the sphericity greater than 0.6 and present in a fluid cell with a void fraction ( $\epsilon$ ) greater than 0.8 is calculated using the Eq. 2.17.<sup>97</sup>

$$\vec{f}_d^j = V_{pj}(1 - \epsilon) \left( \frac{3\rho_f \epsilon C d_j^{ns} \lambda_j |\vec{U}_f - \vec{V}_j|}{4d_{pvj}} \right) (\vec{U}_f - \vec{V}_j), \epsilon \geq 0.8 \quad 2.17$$

Here,  $V_{pj}$ , and  $(\vec{U}_f - \vec{V}_j)$  are the volume, and the relative velocity of the non-spherical particle  $j$ .

The volume equivalent diameter ( $d_{pvj}$ ) is calculated using the Eq. 2.18.

$$d_{pvj} = \left( \frac{6V_{pj}}{\pi} \right)^{1/3} \quad 2.18$$

The non-spherical drag coefficient  $Cd_j^{ns}$  is given by the Eq. 2.19.

$$Cd_j^{ns} = \frac{24}{Re_{pj}^{ns} K_{1j}} (1 + 0.1118 (Re_{pj}^{ns} K_{1j} K_{2j})^{0.6567}) + \frac{0.4305 Re_{pj}^{ns} K_{1j} K_{2j}^2}{Re_p^{ns} K_{1j} K_{2j} + 3305} \quad 2.19$$

Here, the non-spherical particle Reynolds number ( $Re_{pj}^{ns}$ ) is calculated using the Eq. 2.20.

$$Re_{pj}^{ns} = \frac{\varepsilon \rho_f |\vec{U}_f - \vec{V}_j| d_{pvj}}{\eta_f} \quad 2.20$$

The first correction factor,  $K_{1j}$  is given by the Eq. 2.21.

$$K_{1j} = \frac{1}{\frac{d_{prj}}{3d_{pvj}} + \frac{2}{3\psi_j^{0.5}}} \quad 2.21$$

Here,  $d_{prj}$  is the diameter of a circle whose area is equal to the projected area of the non-spherical particle on the corresponding plane. For a non-spherical particle made up of two equal sub-spheres the projected diameters are calculated using the Eq. 2.22.

$$d_{prj} = \sqrt{\frac{4}{\pi} \left( 2\pi R_{se}^2 - \left( 2R_{se}^2 \cos^{-1} \left( \frac{\zeta_{se}}{2R_{se}} \right) - \frac{\zeta_i \sqrt{4R_{se}^2 - \zeta_{se}^2}}{2} \right) \right)} \quad 2.22$$

Here,  $\zeta_{se}$  and  $R_{se}$  are the distance between the centers of the sub-spheres projected on the corresponding planes and the radius of the sub-sphere, respectively.



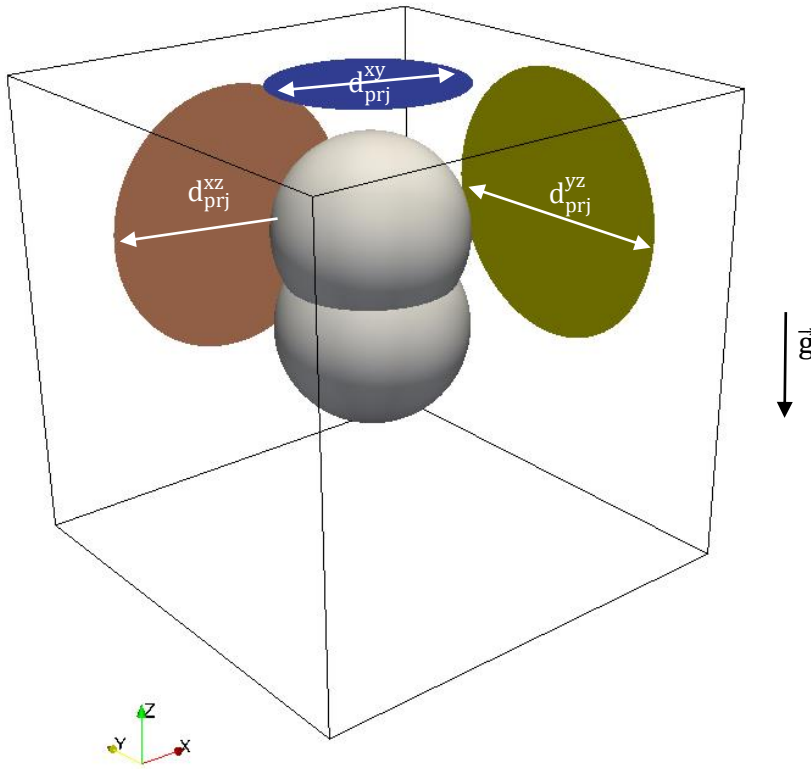


Fig. 2.4 A non-spherical particle generated from two overlapping spherical sub-elements in a CFD fluid cell and the projected area diameters on the corresponding planes.

The sphericity  $\psi_j$  is given by the Eq. 2.23.<sup>121</sup>

$$\psi_j = \frac{\pi^{1/3}(6V_{pj})^{2/3}}{A_{pj}} \quad 2.23$$

Here  $A_{pj}$  is the actual surface area of the non-spherical particle.

The second correction factor,  $K_{2j}$  is given by the Eq. 2.24.

$$K_{2j} = 10^{1.8148(-\log_{10}(\psi_j)^{0.5743})} \quad 2.24$$

The effect of the surrounding particles (suspension) on a particle  $j$  is introduced in the Eq. 2.17 by considering the suspension correction factor  $\lambda_j$  given by the Eq. 2.25.

$$\lambda_j = \varepsilon^2 + (\gamma_j - 2)n_j \quad 2.25$$

Here,  $\gamma_j$  is given by the Eq. 2.26.

$$\gamma_j = \frac{1.002}{\psi_j^{2.145}} - 0.0429 \exp(\log(\text{Re}_{tj}/\psi_j^{3.1618})/3.749) \quad 2.26$$

Here, the terminal Reynolds number ( $\text{Re}_{tj}$ ) is given by the Eq. 2.27.

$$\text{Re}_{tj} = \frac{u_{tj} \rho_p d_{pvj}}{\eta_f} \quad 2.27$$

The magnitude of terminal velocity ( $u_{tj}$ ) of the non-spherical particle is calculated using the Eq. 2.28.<sup>122</sup>

$$u_{tj} = \frac{1}{\left( \frac{18}{d_{*j}^2} + \frac{2.3343 - 1.7439\psi_j}{d_{*j}^{0.5}} \right) \left( \frac{\rho_f^2}{g\eta_f(\rho_p - \rho_f)} \right)^{1/3}} \quad 2.28$$

$d_{*j}$  used here is given by the Eq. 2.29.

$$d_{*j} = d_{pvj} \left( \frac{g\rho_f(\rho_p - \rho_f)}{\eta_f^2} \right)^{1/3} \quad 2.29$$

The index function  $n_j$  used in the Eq. 2.25 is calculated using the Eq. 2.30.

$$\log(n_j) = -0.0153(\log(\text{Re}_{tj}\psi_j))^2 - 0.0279\log(\text{Re}_{tj}\psi_j) + 1.6896 \quad 2.30$$

### *Dense flows*

For the void fraction less than 0.8, the Ergun drag equation is used (Eq. 2.31).<sup>97</sup>

$$\vec{f}_d^j = V_{pj}(1 - \varepsilon) \left( \frac{150(1 - \varepsilon)\eta_f}{\varepsilon(\psi_j d_{pvj})^2} + \frac{1.75|\vec{U}_f - \vec{V}_j|\rho_f}{\psi_j d_{pvj}} \right) (\vec{U}_f - \vec{V}_j), \varepsilon < 0.8 \quad 2.31$$

Here,  $V_{pj}$ ,  $\psi_j$ ,  $d_{pvj}$ ,  $(\vec{U}_f - \vec{V}_j)$  are the volume, the sphericity, the volume equivalent diameter and the relative velocity of the particle  $j$ , respectively. It should be noted that, the viscous coefficient as 150 and inertial coefficient as 1.75 in the Eq. 2.31 are valid for the particle Reynolds number (Eq. 2.20) less than 5. When the Reynolds number in between 5 and 80, the viscous and the inertial coefficient as 182 and 1.92 must be used. In the cases where Reynolds number greater than 80 the recommended coefficients are 225 and 1.61, respectively.<sup>123</sup>

## 2.4 Lagrangian formulation

In the Lagrangian formulation, the motion of a particle in the body fixed reference, is predicted by solving the linear momentum (Eq. 2.32) and the angular momentum (Eq. 2.33) equations.

$$m_j \frac{d\vec{V}_j}{dt} = \vec{f}_g^j + \vec{f}_d^j + \vec{f}_{pg}^j + \vec{f}_{ss}^j + \vec{f}_{lu}^j + \sum_{l \in CL} \vec{f}_c^{j,l} \quad 2.32$$

Here,  $m_j$ , and  $\vec{V}_j$ , are the mass and the linear velocity of the particle  $j$ , respectively. The term  $\vec{f}_g^j$  represents the gravitational force acting on a particle  $j$ .

The coupling to the flow is reflected by the drag force  $(\vec{f}_d^j, \text{sec. 2.3.4})$ , the pressure gradient force  $(\vec{f}_{pg}^j, \text{Eq. 2.8})$  and the fluid particle shear stress force  $(\vec{f}_{ss}^j, \text{Eq. 2.9})$ .  $\vec{f}_{lu}^j$  is the lubrication force which is explained in the sec. 2.4.1 and the details of the contact force  $(f_c^{j,l})$  are discussed in the sec. 2.4.2.

The angular momentum equation reads,

$$I_j \frac{d\vec{\omega}_j}{dt} + \vec{\omega}_j \times (I_j \vec{\omega}_j) = \sum_{l \in CL} (\vec{M}_t^{j,l} + \vec{M}_r^{j,l}) \quad 2.33$$

Here,  $I_j$ , and  $\vec{\omega}_j$  are the moment of inertia, and the angular momentum of the particle  $j$ . The second term on the left hand side of the Eq. 2.33 is zero if the body fixed frame of reference and the global frame of reference coincide.<sup>11</sup> For numerical calculations, global frame of reference is used for spherical particle and a body fixed frame of reference for non-spherical particles.<sup>42,124</sup>

The torque due to tangential contact forces ( $\vec{M}_t^{j,l}$ ) and the resistive rolling angular momentum ( $\vec{M}_r^{j,l}$ ) are calculated for each contact pair listed in the contact list CL using the DEM soft-sphere modelling approach (sec. 2.4.2).<sup>11,18,125,126</sup>

### 2.4.1 Lubrication force

The lubrication force is a hydrodynamic viscous force arising due to the radial pressure generated by the squeezing of the fluid between two solid surfaces.<sup>127</sup> According to the lubrication theory,<sup>73,128</sup> the lubrication force acting between the two surfaces ( $j, l$ ) is given by the Eq. 2.34.

$$\vec{f}_{lu}^{j,l} = (-6\pi\eta_f R^{*,j,l} v_{rn}^{j,l} A_l) \vec{n}^{i,l} \quad 2.34$$

Here,  $\eta_f$ ,  $R^{*,j,l}$ , and  $v_{rn}^{j,l}$ , are the dynamic fluid viscosity, the equivalent radius (Eq. 2.41), and the relative normal velocity.  $A_l$  is the amplification factor given by the Eq. 2.35.<sup>129</sup>

$$A_l = \frac{R^{*,j,l}}{h} - 0.2 \ln\left(\frac{h}{R^{*,j,l}}\right) - \frac{1}{21} \ln\left(\frac{h}{R^{*,j,l}}\right) + \frac{0.24h}{R^{*,j,l}} + 1.048 \quad 2.35$$

Here,  $h$  is the distance between the surfaces. The Fig. 2.5 shows the projection of an imaginary sphere surrounding the particles. If any other surface comes inside the imaginary sphere, the lubrication force is calculated using Eq. 2.34.

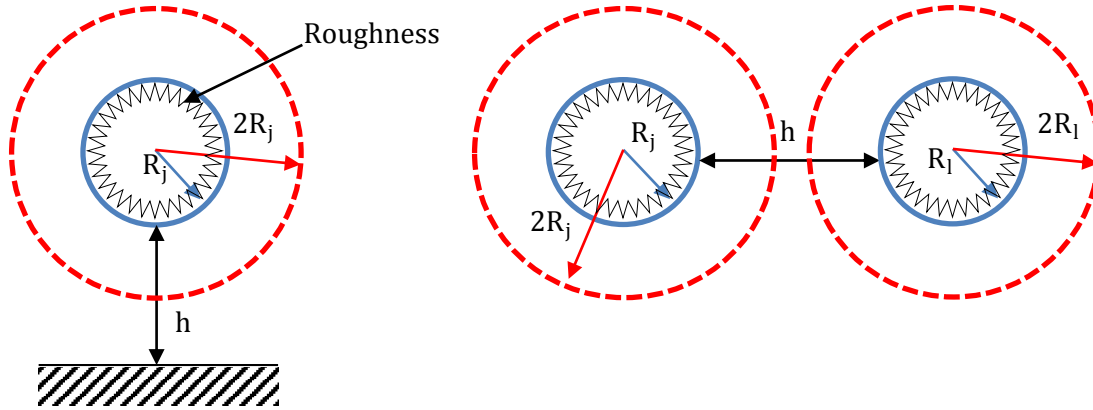


Fig. 2.5 Imaginary spheres surrounding the particles.

The radius of the imaginary sphere is twice the particle radius. It should be noted that, if the distance between the surfaces ( $h$ ) is zero, the lubrication force calculated by the Eq. 2.34 is infinite. In this study, this condition is avoided by considering a cutoff distance ( $0.001R_j$ ). For a distance ( $h$ ) less than the cutoff distance the lubrication force is assumed to be constant. A similar approach is used in the literature.<sup>41,129–132</sup> The surface roughness effect can be included by extending the cutoff lubrication force to a point where the overlap between the surfaces is equal to the average roughness of the particle.<sup>129,131,132</sup>

### 2.4.2 DEM soft-sphere modelling

The Fig. 2.6 shows the graphical representation of the notations used for two spherical particles in contact under the soft-sphere assumptions. The DEM soft-sphere modelling is based on the following assumptions.

- 1) The surfaces in contact are deformable, but they regain their original shape once they detach.
- 2) The interaction between the bodies in contact via a very small contact area (overlap,  $\delta_n^{j,l} \ll R_j, R_l$ ) which is calculated using the Eq. 2.36.

$$\delta_n^{j,l} = R_j + R_l - |\vec{x}_j - \vec{x}_l| \quad 2.36$$

Here,  $R_j$ ,  $R_l$  and  $\vec{x}_j$ ,  $\vec{x}_l$  are the radii and the position vectors of the spheres  $j$  and  $l$ , respectively.

- 3) The overlap not only depends of the particle positions but also on the physical properties of the particles.
- 4) The total contact force ( $\vec{f}_c^{j,l}$ , Eq. 2.37) can be calculated using the force-displacement laws.<sup>11,18,113,114</sup>

$$\vec{f}_c^{j,l} = \vec{f}_{cn}^{j,l} + \vec{f}_{ct}^{j,l} \quad 2.37$$

Here,  $\vec{f}_{cn}^{j,l}$ ,  $\vec{f}_{ct}^{j,l}$  are the normal and the tangential contact forces which are discussed in the following sub-sections.

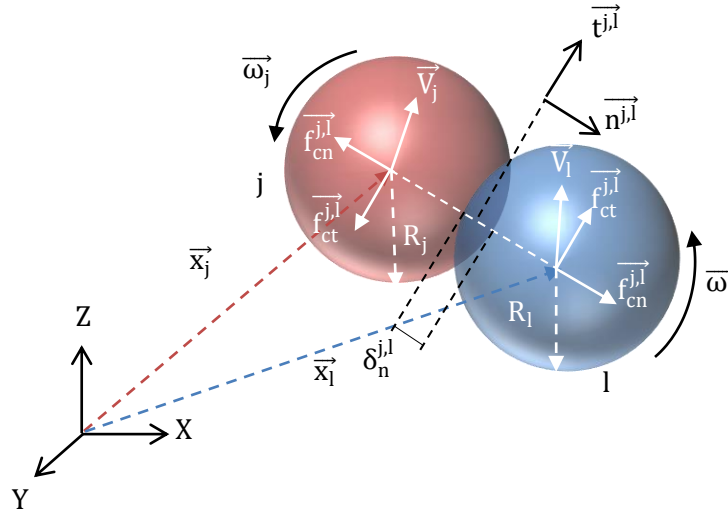


Fig. 2.6 Graphical representation of the notations used in the DEM soft-sphere modelling.

### 2.4.2.1 Normal contact force

The normal contact force  $\left(\overrightarrow{f_{cn}^{j,l}}\right)$  is given by the Eq. 2.38.<sup>126,133,134</sup>

$$\overrightarrow{f_{cn}^{j,l}} = \overrightarrow{f_{cn}^{el,j,l}} + \overrightarrow{f_{cn}^{dis,j,l}} \quad 2.38$$

Here,  $\overrightarrow{f_{cn}^{el,j,l}}$  and  $\overrightarrow{f_{cn}^{dis,j,l}}$  are the elastic and the dissipative normal contact forces. The details of these forces are presented in the following sub-sections.

#### *Elastic component of normal contact force*

According to the combined Hertz-Mindlin and Deresiewicz viscoelastic model,<sup>126,133</sup>

the elastic component of the normal contact force  $\left(\overrightarrow{f_{cn}^{el,j,l}}\right)$  is given by the Eq. 2.39.

$$\overrightarrow{f_{cn}^{el,j,l}} = \left( \frac{4}{3} E^{*j,l} \sqrt{R^{*j,l}} (\delta_n^{j,l})^{3/2} \right) \overrightarrow{n^{j,l}} \quad 2.39$$

Here,  $\delta_n^{j,l}$  is the normal overlap (Eq. 2.36).

The effective Young's modulus  $\left(E^{*j,l}\right)$  is given by the Eq. 2.40.

$$\frac{1}{E^{*j,l}} = \frac{(1 - \nu_j^2)}{E_j} + \frac{(1 - \nu_l^2)}{E_l} \quad 2.40$$

$\nu$  is the Poisson's ratio.

The effective radius  $\left(R^{*j,l}\right)$  is given by the Eq. 2.41.

$$\frac{1}{R^{*j,l}} = \frac{1}{R_j} + \frac{1}{R_l} \quad 2.41$$

The unit normal vector for the particles in contact is given by the Eq. 2.42.

$$\overrightarrow{n^{j,l}} = \frac{\overrightarrow{x_j} - \overrightarrow{x_l}}{|\overrightarrow{x_j} - \overrightarrow{x_l}|} \quad 2.42$$

### *Dissipative component of normal contact force*

The dissipative component of the normal contact force  $\left(\overrightarrow{f_{cn}^{dis,j,l}}\right)$  describing the viscous damping is given by Eq. 2.43.<sup>134</sup>

$$\overrightarrow{f_{cn}^{dis,j,l}} = \left( -2 \ln(e_n) \left( \sqrt{\frac{5E^{*,j,l}m^{*,j,l}}{3((\ln(e_n))^2 + \pi^2)}} \right) (R^{*,j,l}\delta_n^{j,l})^{1/4} v_{nr}^{j,l} \right) \overrightarrow{n^{j,l}} \quad 2.43$$

Here,  $e_n$  is the coefficient of the normal restitution,  $v_{nr}^{j,l}$  is the normal relative velocity and  $m^{*,j,l}$  is the effective mass given by Eq. 2.44.

$$\frac{1}{m^{*,j,l}} = \frac{1}{m_j} + \frac{1}{m_l} \quad 2.44$$

### **2.4.2.2 Tangential contact force**

The total tangential contact force  $\left(\overrightarrow{f_{ct}^{j,l}}\right)$  is limited by the Coulomb's law as shown in the Eq. 2.45.<sup>11,133</sup>

$$\overrightarrow{f_{ct}^{j,l}} = \left( \min \left( \mu_s \left| \overrightarrow{f_{cn}^{el,j,l}} \right|, \left| \overrightarrow{f_{ct}^{el,j,l}} + \overrightarrow{f_{ct}^{dis,j,l}} \right| \right) \right) \overrightarrow{t^{j,l}} \quad 2.45$$

Here,  $\overrightarrow{f_{ct}^{el,j,l}}$  and  $\overrightarrow{f_{ct}^{dis,j,l}}$  are the elastic and the dissipative tangential contact forces. The details of these forces are as follows.

### *Elastic component of tangential contact force*

The elastic component of the tangential contact force  $\left(\overrightarrow{f_{ct}^{el,j,l}}\right)$  is given by the Eq. 2.46.

$$\overrightarrow{f_{ct}^{el,j,l}} = \left( 8G^{*,j,l} \left( \sqrt{R^{*,j,l}\delta_n^{j,l}} \right) \delta_t^{j,l} \right) \overrightarrow{t^{j,l}} \quad 2.46$$



Here,  $G^{*,l}$  is the equivalent shear modulus (Eq. 2.47).

$$\frac{1}{G^{*,l}} = \frac{2(2 - \nu_j)(1 + \nu_j)}{E_j} + \frac{2(2 - \nu_l)(1 + \nu_l)}{E_l} \quad 2.47$$

According to the theory proposed by Mindlin and Deresiewicz,<sup>133</sup> the tangential elastic force depends on the loading history. Di Renzo and Di Maio<sup>125,135</sup> have argued that this dependency can be incorporated in the DEM simulations by using a time incremental approach for the calculation of the tangential overlap ( $\delta_t^{j,l}$ ) as given in the Eq. 2.48.

$$\delta_t^{j,l} = \left| \overrightarrow{\delta_{t0}^{j,l}} + \overrightarrow{v_{tr}^{j,l}} t_p \right| \quad 2.48$$

Here,  $\overrightarrow{\delta_{t0}^{j,l}}$ ,  $\overrightarrow{v_{tr}^{j,l}}$  and  $t_p$  are the tangential displacement in the previous time step, the tangential velocity and the time step, respectively.

#### *Dissipative component of tangential contact force*

The dissipative component of the tangential contact force ( $\overrightarrow{f_{ct}^{dis,j,l}}$ ) is similar to the dissipative normal force except, it also depends on the tangential relative velocity ( $\overrightarrow{v_{tr}^{j,l}}$ ) and is given by the Eq. 2.49.<sup>133,134</sup>

$$\overrightarrow{f_{ct}^{dis,j,l}} = \left( -2 \ln(e_n) \left( \sqrt{\frac{20E^{*,l}m^{*,l}}{3((\ln(e_n))^2 + \pi^2)}} \right) (R^{*,l}\delta_n^{j,l})^{1/4} \overrightarrow{v_{tr}^{j,l}} \right) \overrightarrow{t_{j,l}} \quad 2.49$$

#### **2.4.2.3 Torque due to tangential contact forces**

Since the tangential contact forces are to be transferred from the point of the contact to the center of the particle, a rotational torque ( $\overrightarrow{M_t^{j,l}}$ , Eq. 2.50) is introduced.<sup>11</sup>

$$\overrightarrow{M}_t^{j,l} = -R_j \overrightarrow{n}^{j,l} \times \overrightarrow{f}_{ct}^{j,l} \quad 2.50$$

Here,  $R_j$  is the radius of the particle. The contribution of the overlap is neglected in the calculation of this moment.

#### 2.4.2.4 Resistive rolling angular momentum

For the calculation of the resistive rolling angular momentum, a constant torque model proposed by Zhou et al.<sup>136</sup> is used (Eq. 2.51).

$$\overrightarrow{M}_r^{j,l} = -\mu_r R^{*j,l} \left| \overrightarrow{f}_{cn}^{j,l} \right| \widehat{\omega}_r^{j,l} \quad 2.51$$

In this model, the direction of the torque is always opposite to the relative rotation of the bodies in contact.  $\mu_r$  is the coefficient of rolling friction and  $\widehat{\omega}_r^{j,l}$  is the relative angular velocity given by the Eq. 2.52 .

$$\widehat{\omega}_r^{j,l} = \frac{\overrightarrow{\omega}^j - \overrightarrow{\omega}^l}{\left| \overrightarrow{\omega}^j - \overrightarrow{\omega}^l \right|} \quad 2.52$$

#### 2.4.2.5 Attractive forces

The contact attractive force is important when it is comparable to or greater than the gravitational force. In such cases, the normal contact force along with the attractive force  $\left( \overrightarrow{f}_{cnwa}^{j,l} \right)$  is given by the Eq. 2.53.<sup>137</sup>

$$\overrightarrow{f}_{cnwa}^{j,l} = \overrightarrow{f}_{cn}^{el,j,l} + \overrightarrow{f}_{cn}^{JKR,j,l} + \overrightarrow{f}_{cn}^{dis,j,l} \quad 2.53$$

Here,  $\overrightarrow{f}_{cn}^{JKR,j,l}$  is the contact attractive force proposed by Johnson, Kendall and Roberts<sup>138</sup> (JKR) and is given by the Eq. 2.54. This model is used by number of studies in the literature.<sup>137,139</sup>

$$\overrightarrow{f_{cn}^{JKR,j,l}} = -\frac{3}{2}\pi R^{*j,l}W_a\overrightarrow{n^{j,l}} \quad 2.54$$

Here,  $W_a$  is the work of adhesion.

When the attractive forces are considered, the critical force i.e. the force beyond which sliding starts is updated from  $\mu_s\overrightarrow{f_{cn}^{el,j,l}}$  to  $\mu_s\overrightarrow{f_{cnwa}^{el,j,l}}$  in the Eq. 2.45.<sup>120</sup>

Further, the influences of the attractive forces are considered in the torque due to the tangential contact forces (Eq. 2.55).

$$\overrightarrow{M_t^{j,l}} = -R_j\overrightarrow{n^{j,l}} \times \overrightarrow{f_{ctwa}^{j,l}} \quad 2.55$$

The resistive rolling angular momentum with the attractive forces is given by the Eq. 2.56.

$$\overrightarrow{M_r^{j,l}} = -\mu_r R^{*j,l} \left| \overrightarrow{f_{cnwa}^{j,l}} \right| \widehat{\omega_r^{j,l}} \quad 2.56$$

### 2.4.3 Multi-sphere DEM modeling

In the multi-element approach, the complex surface of a particle is constructed by using sub-elements.<sup>21–24</sup> If non-interacting spheres are used as sub-elements it is called as the multi-sphere approach. Theoretically, by controlling the sub-spheres (size, position), the desired particle shape can be generated. The notations used in the multi-sphere DEM modelling are shown in the Fig. 2.7.

The governing equations are the same as present in the sec. 2.4. but the complete modelling requires additional calculation of the basic properties (sec. 2.4.3.1). Further vector additions of the contact forces (sec. 2.4.3.2) and the torques (sec. 2.4.3.3) are needed.<sup>14,25</sup>

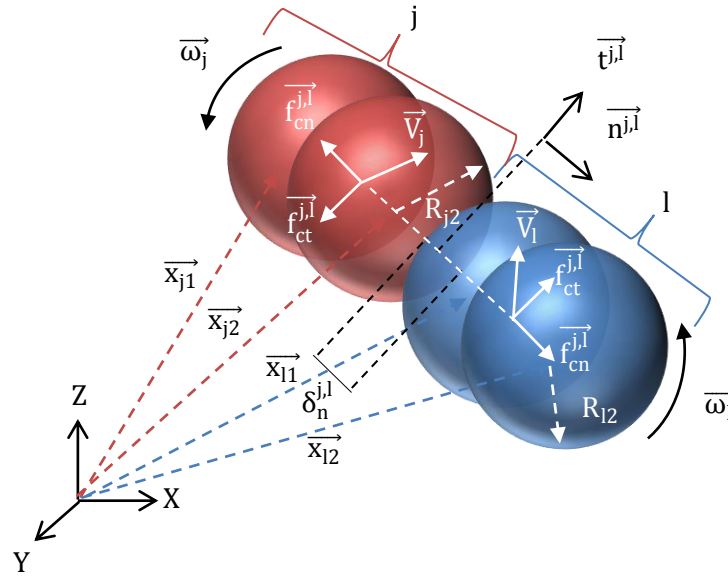


Fig. 2.7 Graphical representation of the notations used in the DEM multi-sphere modelling.

### 2.4.3.1 Basic properties

#### *Mass*

The mass of a non-spherical particle is calculated using the Eq. 2.57.

$$m_j = \sum_{se=1}^{Ns} m_{se} \quad 2.57$$

Here,  $N_s$  is the number of sub-spheres in the non-spherical particle,  $m_{se}$  is the overlap corrected mass of the sub-sphere.

#### *Center of mass*

The coordinates of the center of mass of a non-spherical particle  $(\bar{X}_j, \bar{Y}_j, \bar{Z}_j)$  are given by the Eq. 2.58.

$$\bar{X}_j = \frac{\sum_{se=1}^{Ns} m_{se} \bar{x}_{se}}{\sum_{se=1}^{Ns} m_{se}}, \bar{Y}_j = \frac{\sum_{se=1}^{Ns} m_{se} \bar{y}_{se}}{\sum_{se=1}^{Ns} m_{se}}, \bar{Z}_j = \frac{\sum_{se=1}^{Ns} m_{se} \bar{z}_{se}}{\sum_{se=1}^{Ns} m_{se}} \quad 2.58$$

Here,  $\bar{x}_{se}$ ,  $\bar{y}_{se}$ , and  $\bar{z}_{se}$  are the overlap corrected components of the center of mass of the sub-sphere se.

### *Principle inertias*

The principle inertias ( $I_{xxj}^{ns}$ ,  $I_{yyj}^{ns}$ ,  $I_{zzj}^{ns}$ ) of a non-spherical particle are calculated using the Eqs. 2.59-2.61.

$$I_{xxj}^{ns} = \sum_{se=1}^{Ns} I_{se} + \sum_{se=1}^{Ns} m_{se} (y_{se}^2 + z_{se}^2) \quad 2.59$$

$$I_{yyj}^{ns} = \sum_{se=1}^{Ns} I_{se} + \sum_{se=1}^{Ns} m_{se} (x_{se}^2 + z_{se}^2) \quad 2.60$$

$$I_{zzj}^{ns} = \sum_{se=1}^{Ns} I_{se} + \sum_{se=1}^{Ns} m_{se} (x_{se}^2 + y_{se}^2) \quad 2.61$$

Here,  $I_{se}$  is the overlap corrected inertia of the sub-sphere se.  $x_{se}$ ,  $y_{se}$  and  $z_{se}$  are the components of the vector between the center of mass of the non-spherical particle and the center of mass of the sub-sphere.

### **2.4.3.2 Contact forces**

The contact force ( $\vec{f}_c^{j,l}$ ) acting on the non-spherical particle j is the vector sum of contact forces acting on all the sub-spheres of that non-spherical particle (Eq. 2.62).

$$\vec{f}_c^{j,l} = \sum_{se=1}^{Ns} \vec{f}_c^{jse,lke} = \sum_{se=1}^{Ns} \left( \vec{f}_{cn}^{jse,lke} + \vec{f}_{ct}^{jse,lke} \right) \quad 2.62$$

For a contact between the sub-sphere se of the non-spherical particle j and the sub-sphere ke of the non-spherical particle l, the total contact force ( $\vec{f}_c^{jse,lke} = \vec{f}_{cn}^{jse,lke} + \vec{f}_{ct}^{jse,lke}$ ) is calculated based on the already discussed soft-sphere modeling approach (secs. 2.4.2.1 and 2.4.2.2).

### 2.4.3.3 Contact torques

The theory behind the calculations of the contact torques is already presented for spherical particles in the secs. 2.4.2.3 and 2.4.2.4.

The only differences are:

- 1) The vector addition of the tangential torque  $\left(\overrightarrow{M_t^{j,l}}\right)$  as shown in the Eq. 2.63.

$$\overrightarrow{M_t^{j,l}} = \sum_{se=1}^{Ns} \left( -R_{jse} \overrightarrow{n^{jse,lke}} \times \overrightarrow{f_{ct}^{jse,lke}} \right) \quad 2.63$$

And,

- 2) The Eq. 2.64 representing the rolling torque resistance.

$$\overrightarrow{M_r^{j,l}} = \sum_{se=1}^{Ns} \left( -\mu_r R_{jse}^* \left| \overrightarrow{f_{cn}^{jse,lke}} \right| \widehat{\omega_r^{jse,lke}} \right) \quad 2.64$$

## 2.5 Time steps

In this section, the various time steps involved in the coupled DEM-CFD simulations are discussed.

In general,

$$t_{CFL} \gg Y_e t_{res} = N_c t_p \quad 2.65$$

Here,  $t_{CFL}$  and  $t_{res}$  are the Eulerian (fluid) phase time steps based on the Courant-Friedrich-Levy (CFL) number and the particle momentum response time criteria, respectively.  $Y_e$  is a fractional value in the range of 0.05 to 0.1.<sup>26,31,140</sup>

$t_p$  is the Lagrangian phase time step and  $N_c$  is the number of Lagrangian phase time steps after which the Lagrangian phase solution is coupled with the Eulerian phase solution. The value of  $N_c$  ranges from 5 to 1000 and is dependent on various factors like the void fraction, the particle Reynolds number, etc.<sup>11,116</sup>

### 2.5.1 Eulerian phase time steps

The value of the Eulerian phase time step is a fraction of the minimum time step based on the Courant-Friedrich-Levy (CFL) number and the particle momentum response criteria.

#### 2.5.1.1 Courant-Friedrich-Levy (CFL) number

A solver based on the PISO algorithm is used to solve the Eulerian phase. For the stability of the PISO algorithm, the Courant-Friedrich-Levy (CFL) number ( $C_0$ ) must be less than 1. CFL based Eulerian phase time step is given by the Eq. 2.66.<sup>26,31,140</sup>

$$t_{\text{CFL}} = \frac{\Delta H}{|\vec{U}_f|} \quad 2.66$$

Here,  $\Delta H$  is the length of the fluid cell in the direction of the flow and  $\vec{U}_f$  is the corresponding fluid velocity.

#### 2.5.1.2 Particle momentum response

Particle momentum response time is the time required by the particle to respond to the changes in the fluid flow. Under the assumption of the Stokes flow, the time required by the particle to reach 63.2% of the fluid velocity is given by the Eq. 2.67.<sup>116</sup>

$$t_{\text{res}} = -\frac{\rho_p d_p^2}{18\eta_f} \ln \left( 1 - \frac{|\vec{V}^{\text{in}}|}{|\vec{U}_f^c|} \right) \quad 2.67$$

Here,  $\vec{V}^{\text{in}}$  is the initial velocity of the particle, and  $\vec{U}_f^c$  is the changed velocity of the fluid.

### 2.5.2 Lagrangian phase time steps

The time step for the Lagrangian phase ( $t_p$ ) is given by the Eq. 2.68.<sup>11</sup>

$$t_p = Y_l \cdot \min(t_{\text{Ray}}, t_{\text{Her}}) \quad 2.68$$

Here, the fraction  $Y_l$  typically ranges between 0.1 to 0.4.<sup>116,124</sup>  $t_{\text{Ray}}$  and  $t_{\text{Her}}$  are the Rayleigh (sec. 2.5.2.1) and the Hertzian (sec. 2.5.2.2) time steps, respectively.

#### 2.5.2.1 Rayleigh time step

The particle dynamics is affected by the prorogation of the disturbance waves through the body or along the surface of the body. Rayleigh waves are the surface waves which carry 2/3<sup>rd</sup> of the disturbances.<sup>141</sup> An estimate of the time required for the Rayleigh way to travel the distance between the particle in contact is given by the Eq. 2.69.<sup>11,124,142,143</sup>

$$t_{\text{Ray}} = \frac{\pi R_{\min}}{0.613\nu + 0.8766} \sqrt{\frac{\rho_p}{G}} \quad 2.69$$

Here,  $\rho_p$ ,  $\nu$ ,  $G$  and  $R_{\min}$  are the density, Poison's ratio, shear modulus and the minimum radii of the particles in contact.

#### 2.5.2.2 Hertzian time step

The contact force in the soft-sphere DEM approach is based on the assumption that there is a slight overlap between the particles in contact. The Lagrangian time step should be small enough to capture the overlap. For the Hertzian contact model,<sup>126</sup> the time interval of overlap is given by the Eq. 2.70.<sup>11,124</sup>

$$t_{\text{Her}} = 2.86 \left( \frac{(m^{*j,l})^2}{R^{*j,l} (E^{*j,l})^2 v_{\text{nr,max}}^{j,l}} \right)^{0.2} \quad 2.70$$

Here,  $m^{*j,l}$ ,  $R^{*j,l}$ ,  $E^{*j,l}$  are the equivalent mass radius and Young's modulus of the particles in contact.  $v_{\text{nr,max}}^{j,l}$  is the maximum normal relative velocity.



## 2.6 Void fraction calculation

The simulation results are sensitive to the calculation of the void fraction. For a fluid control volume with  $n_p$  number of particles, the void fraction of the fluid cell can be calculated using the Eq. 2.71.

$$\varepsilon = 1 - \frac{1}{V_{\text{cell}}} \sum_{i=1}^{n_p} \varphi_i V_{p_i} \quad 2.71$$

Here,  $V_{\text{cell}}$  is the volume of the fluid cell,  $V_{p_i}$  is the volume of the particle  $i$ .  $\varphi_i$  is the volume fraction weightage of the particle  $i$  associated with the fluid control volume.  $\varphi_i$  is 1 when particle is completely inside a fluid control volume. The value of  $\varphi_i$  must be calculated as accurately as possible when the particle is partly in a fluid control volume.

Even though the analytical methods available in the literature<sup>144,145</sup> are accurate in calculating the  $\varphi_i$ , their implementation is challenging for arbitrary shaped particles in arbitrary fluid control volumes.<sup>11,146</sup>

The non-analytical approaches<sup>40,115,147,148</sup> are simpler and can be used for all shapes of particles and fluid control volumes. One of the non-analytical method is *Divided void fraction method*. In this method the particle is divided into smaller sub-regions. Each of the sub-region is associated with the weights based on the volume it covers.

In the following sections, the void fraction calculation based on the *Divided void fraction method* for the spherical mono-dispersed, the spherical bi-dispersed and the non-spherical mono-dispersed particles are described in detail.

### 2.6.1 Spherical mono-dispersed

In the *Divided void fraction method*, each spherical particle is divided into 29 sub-regions of equal volume. Then the centroids of all the sub regions are calculated. The graphical representation of the 29 regions with the corresponding centroids is shown in the Fig. 2.8.<sup>43</sup>

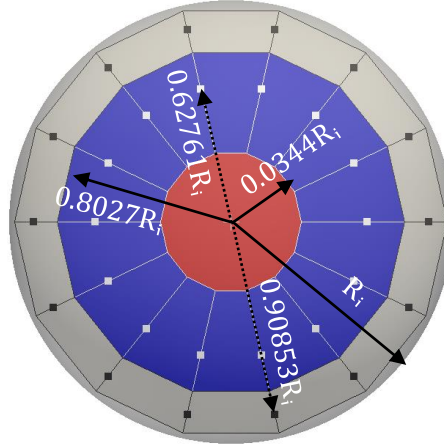


Fig. 2.8 Graphical representation of the different regions in the divided void fraction model.

### 2.6.2 Spherical bi-dispersed

The first region is a sphere of radius of  $0.0344R_i$  with the centroid at the center of the particle. The next 14 regions are the equally divided regions of an imaginary annular volume bounded by the lower radius of  $0.0344R_i$  and the higher radius of  $0.8027R_i$ . The locus of centroid of these 14 regions is at  $0.62761R_i$ . Similarly, the next 14 regions are the equally divided regions of an imaginary annular volume with lower radius of  $0.8027R_i$  and the higher bound of  $R_i$  the centroid of these regions lies on the locus of  $0.90853R_i$ .<sup>43</sup> Thus, when a particle is partly in a fluid control volume,  $\varphi_i$  can be calculated based on the position of the centroids relative to the fluid cell.<sup>43</sup>

For the calculation of the drag force based on the Beetstra drag model (sec. 2.3.4.1), the contribution of each size of the particles to the total void fraction must be known. Hence, in addition to already available *Divided void fraction model* a void fraction model called as the *Divided void fraction big* is implemented. This model calculates the void fraction contribution of the big size particles ( $\varepsilon_b$ ) only.

$$\varepsilon_b = 1 - \frac{1}{V_{\text{cell}}} \sum_{i=1}^{np_b} \varphi_i V_{pi} \quad 2.72$$

Here,  $np_b$  is the number of particles in a fluid control volume corresponding to the largest diameter.

The void fraction contribution by the smaller particles ( $\epsilon_s$ ) is calculated using the Eq. 2.73.

$$\epsilon_s = 1 - (\epsilon_b - \epsilon) \quad 2.73$$

### 2.6.3 Non-spherical mono-dispersed

In the case of the non-spherical particles, the void fraction is calculated based on the mathematical formulation given by the Eq. 2.74.

$$\epsilon = 1 - \frac{1}{V_{\text{cell}}} \left( \sum_{i=1}^{np} \sum_{se=1}^{Ns} w_{se} \phi_{se} V_{pi} \right) \quad 2.74$$

In the implementation, the *Divided void fraction model* is modified to incorporate the volume/mass weightage of each sub-element ( $w_{se}$ ) which is 0.5 for a non-spherical particle with sub-spheres of equal radius and density. The volume fraction weightage of the sub-element ( $\phi_{se}$ ) is calculated based on the divided void fraction method as explained in the sec. 2.6.1.

## 2.7 FVM numerical solver

The *pisoFoam solver*, available in OpenFOAM is modelled for single phase, incompressible, transient, turbulent flows.<sup>31</sup> The *piso-* in *pisoFoam* stands for Pressure-Implicit with Splitting of Operators (PISO) algorithm proposed by Issa.<sup>149</sup> The discretization of the governing fluid mass and the momentum equation (PDEs) is based on the Finite Volume Method (FVM).<sup>26,31,140</sup>

The basic idea behind the PISO algorithm is as follows:

At low CFL numbers the linear pressure-velocity coupling in the fluid momentum equations is much stronger than the non-linear pressure-velocity coupling in the con-

vection term of the fluid momentum equation. Therefore, a number of pressure corrector steps can be performed without updating the discretization of the momentum equation.<sup>140,149,150</sup>

Goniva and Kloss<sup>42</sup> have used the framework of the *pisoFoam solver* and modified it for the volume averaged DEM-CFD coupling. This was done by including the void fraction in fluid mass and momentum equations and adding a particle-fluid source term to the fluid momentum equation.

For the computational reasons, the particle-fluid source term ( $\vec{S}_{pf}$ ) is decomposed into the implicit and the explicit part as shown in the Eq. 2.75.

$$\vec{S}_{pf} = - \frac{\left| \sum_j^{np} (\vec{f}_d^j) \right| \vec{U}_f}{V_{cell} |\vec{U}_f - \langle \vec{V} \rangle|} + \frac{\left| \sum_j^{np} (\vec{f}_d^j) \right| \langle \vec{V} \rangle}{V_{cell} |\vec{U}_f - \langle \vec{V} \rangle|} \quad 2.75$$

Here, the first term on the right hand side is the implicit part and the second term is the explicit part. This distinction exists because the fluid velocity  $\vec{U}_f$  is the velocity of the current fluid time step whereas the cell ensemble averaged particle velocity ( $\langle \vec{V} \rangle$ ) is from the previous DEM time step at which the two solutions were coupled.<sup>42,116</sup>

It should be noted that the implemented particle-fluid source term, considers only the drag force. The contribution of the pressure gradient and the shear stress force is included in the implementation by multiplying the pressure and shear stress in the fluid momentum equation with the void fraction of the fluid control volume. The modified solver is named as *cfDEM solverPiso*. This solver is available in the open source library CFDEM.<sup>43</sup>

## 2.8 DEM numerical solver

LIGGGHTS<sup>42,124</sup> (LAMMPS Improved for General Granular and Granular Heat Transfer Simulations) is an open source DEM solver based on LAMMPS (Large-scale Atomic/Molecular Massively Parallel Simulator) written in the C++ programming language. LIGGGHTS can be compiled on machines with parallel computation capabilities which supports message-passing parallelism (MPI).<sup>124</sup>

For spherical particles, the soft-sphere approach discussed in the sec. 2.4.2 is already available in LIGGGHTS. In a multi-particle system, the soft-sphere approach needs to know possible contact pairs (list). Optimizing the creation of a contact list (CL) is itself a challenging task. The all-particle-pair<sup>11</sup> algorithm is not suitable for systems with large number of particles. Therefore, LIGGGHTS uses a cell-based-algorithm which is briefly described here.

The contact list (CL) in LIGGGHTS is prepared by first dividing the whole computational domain into smaller regions called as bins.<sup>42</sup> The size of the bins has a significant effect on the computational effort. Each particle in the domain is associated with a bin and imaginary boxes slightly larger than the particle are used for searching the possible contact pairs. The size of the imaginary box and the velocity of the particle determines the frequency to update the CL. For non-contact forces like the lubrication force, the search to prepare the CL is carried out for a larger distance  $(2R_j)$ .<sup>42,124</sup>

## 2.9 Limitations

The limitations of the present implementations in the LIGGGHTS-OpenFOAM (CFDEM) frame work are listed here.

1. As volume averaged coupling is used, the local particle-fluid interactions are not considered in the mass and the momentum equations of the fluid phase.
2. The current implementation of the Beetstra<sup>93,96</sup> drag model is limited to bi-dispersed particles.
3. In the implementation of the Lu, Wei and Wei<sup>97</sup> drag model, the calculation of the projected diameter is restricted to two overlapping sub-spheres of equal radii. Further, the properties like the volume equivalent diameter, sphericity are manually calculated. Hence, very complex shaped non-spherical particles cannot be simulated.
4. The JKR attractive force<sup>138</sup> is considered only when the surfaces are in contact. The non-contact attractive/repulsive forces are not considered in the implementation.

---

## 3 Experimental Studies

---

### 3.1 Introduction

In this chapter, the experimentally measured particle-particle/wall coefficient of restitution ( $e_n$ ) and the coefficient of sliding friction ( $\mu_s$ ) are reported. The aim of these experiments is to acquire qualitative values or empirical correlations which will serve as inputs to the numerical studies.

### 3.2 Coefficient of restitution

There are a few attempts in the literature to quantify the dependency of the coefficient of normal restitution ( $e_n$ ) to the Stokes number (St).<sup>69–73</sup> Here, the coefficient of normal restitution is defined as the ratio of the particle's normal velocity after collision to the particle's normal velocity before collision.<sup>73,128</sup> For a particle in a viscous fluid, the Stokes number (St, Eq. 3.1) represents the comparative strength of the inertial and the viscous forces acting on the particle.<sup>69,73,128,151</sup>

$$St = \frac{mV_{imp}}{6\pi\eta_f R^2} \quad 3.1$$

Here,  $m$ ,  $V_{imp}$ ,  $R$  and  $\eta_f$  are the mass, the impact velocity, the radius of the particle and the dynamic viscosity of the fluid, respectively.

Based on the various experimental data available in the literature,<sup>69–71,152,153</sup> Legendre et al.<sup>69</sup> have suggested that the relation between the Stokes number and the coefficient of restitution is given by the Eq. 3.2.

$$e_n = \alpha \times \exp\left(-\frac{\beta}{St}\right) \quad 3.2$$

Here,  $\alpha$  and  $\beta$  are the empirical constants. They depend on the factors like the particle type (solid/liquid), the particle size, the material (Poisson's ratio and Young's modulus), the roughness, the type of contacts (area/point), etc.

The best fit to the experimental data in the literature is obtained with the values of  $\alpha$  and  $\beta$  as 0.91 and 35, respectively.<sup>69</sup> These are valid for the particles with diameter greater than 1000  $\mu\text{m}$ . The typical size of the particles encountered in the packed beds/cakes is less than 1000  $\mu\text{m}$ .<sup>154</sup> In the present study, we perform the experiments to obtain the values of the  $\alpha$  and  $\beta$  for the zirconium dioxide particles in the diameter range of 200 to 1000  $\mu\text{m}$ . The details of this are provided in the following sections.

### 3.2.1 Experimental setup

The schematic of the experimental setup is shown in the Fig. 3.1. The key components of the setup are:

- 1) A vacuum nozzle, used to hold a particle.
- 2) A PYREX<sup>TM</sup> glass container<sup>155</sup> with a cross section of 10 × 10 mm.
- 3) A titanium plate which acts as the bottom of the container. The thickness and the average roughness of the plate are 2 mm and 0.64  $\mu\text{m}$ , respectively
- 4) A LED light source<sup>156</sup> for the illumination.
- 5) A high speed digital camera<sup>157</sup> with a max frame rate of 42000 fps and a max resolution of 1920 x 1280 pixels for recording the particle motion.
- 6) A valve used to release the vacuum pressure in the nozzle.
- 7) A data storage and processing unit.

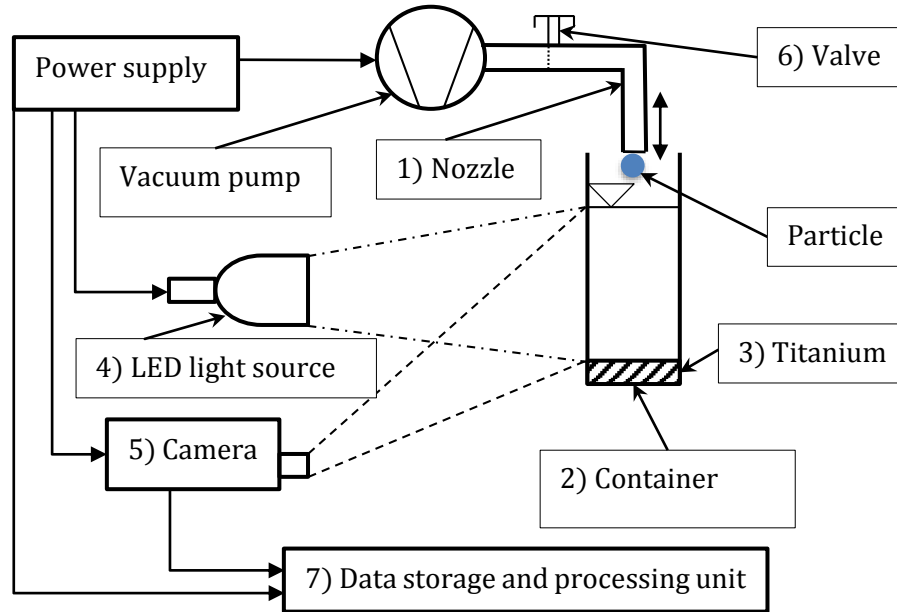


Fig. 3.1 Schematic of the experimental setup to measure the coefficient of restitution.

### 3.2.2 Procedure

For the measurement of the coefficient of restitution, first the container is filled with a fluid (water, ethanol or air). Then a particle of a known material and diameter (zirconium dioxide,  $\rho_p = 6.06 \text{ gm/cm}^3$ ,  $d_p = 200 \text{ to } 1000 \text{ }\mu\text{m}$ ) is loaded at the tip of the vacuum nozzle. Then, the nozzle is lowered to a point where its tip is just below the fluid surface. At this point the light source and the camera are switched on. The focus of the camera is adjusted and a reference image is stored. Then, with the help of the valve, the vacuum pressure in the nozzle is released. This releases the particle, allowing it to undergo sedimentation.

The camera continuously records and stores the frames for post processing. The Fig. 3.2 shows sample frames of the recording at:

- The initial position of the particle (start of the recording).
- An intermediate frame showing the particle approaching the bottom plate.
- A frame showing the impact of the particle with the bottom plate.
- A frame showing the particle after impact.

The post processing of the recordings is done with the help of a Matlab<sup>158</sup> script. The Matlab script scales the pixels to the actual distance using a reference image. The velocity of the particle ( $\vec{u}_p$ ) is given by Eq. 3.3.



$$\vec{u}_p = \vec{d}_{bf} f_r \quad 3.3$$

Here,  $\vec{d}_{bf}$  and  $f_r$  are the displacement of the particle between successive frames and the frame rate, respectively.

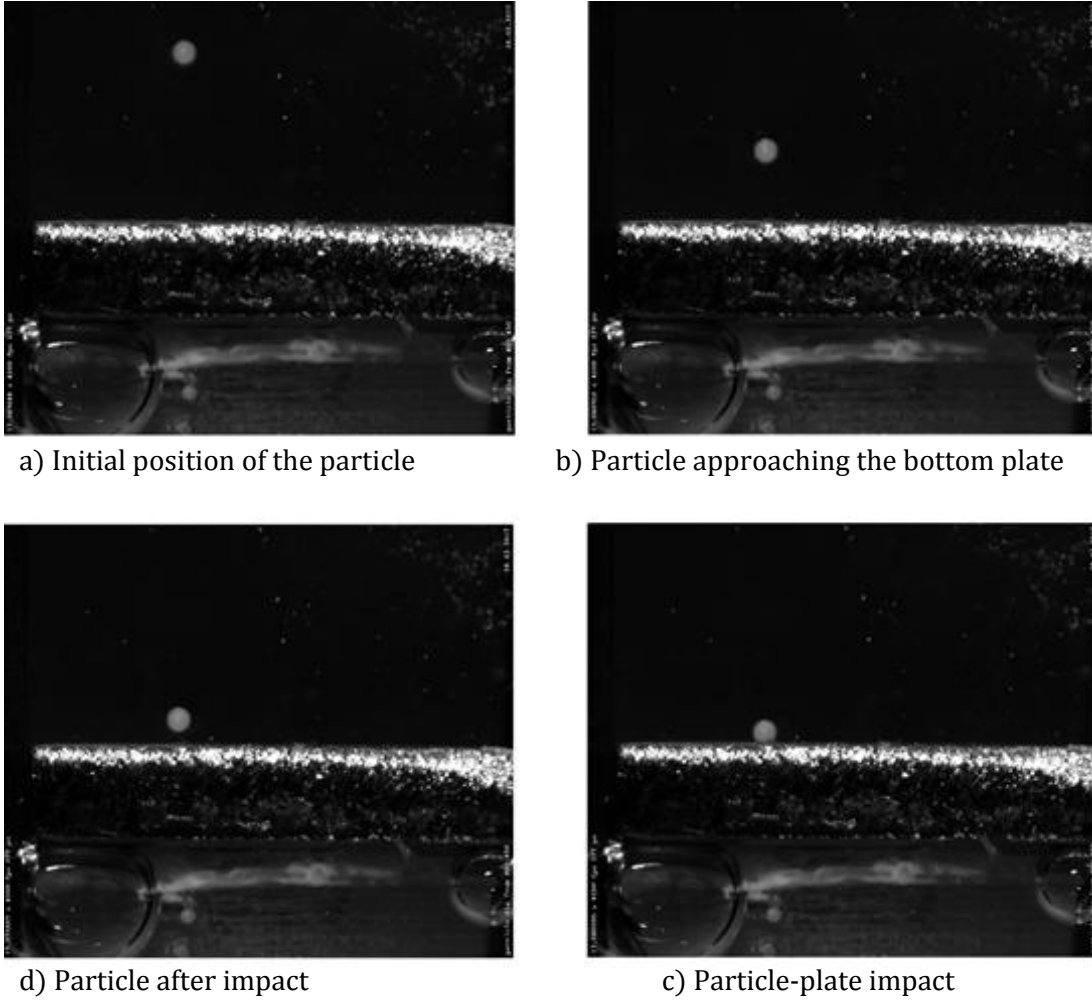


Fig. 3.2 Frames recorded by the camera for a zirconium dioxide particle ( $d_p = 442.37 \mu\text{m}$ ) in water.

### 3.2.3 Validation

There are various correlations in the literature<sup>159–163</sup> to obtain the terminal velocity of a sedimenting particle. The correlation proposed by Turton and Clark<sup>163</sup> is given by the Eq. 3.4.

$$u_t = \frac{1}{\left( \left( \frac{18}{d_*^2} \right)^{0.824} + \left( \frac{0.321}{d_*} \right)^{0.412} \right)^{1.214} \left( \frac{\rho_f^2}{g\eta_f(\rho_p - \rho_f)} \right)^{1/3}} \quad 3.4$$

Here,  $\rho_f$  and  $\eta_f$  are the density and the dynamic viscosity of the fluid,  $\rho_p$  is the particle density.  $d_*$  is given by the Eq. 3.5.

$$d_* = d_p \left( \frac{g\rho_f(\rho_p - \rho_f)}{\eta_f^2} \right)^{1/3} \quad 3.5$$

The Fig. 3.3 shows the experimentally measured velocity a particle (zirconium dioxide,  $d_p = 442.37 \mu\text{m}$ ) in water. The experimentally measured average terminal velocity ( $u_t^{\text{exp}}$ ) of this particle (region b, Fig. 3.3) is 15.17 cm/s. It is observed that the measured terminal velocity is in close agreement with the Eq. 3.4 (15.35 cm/s).

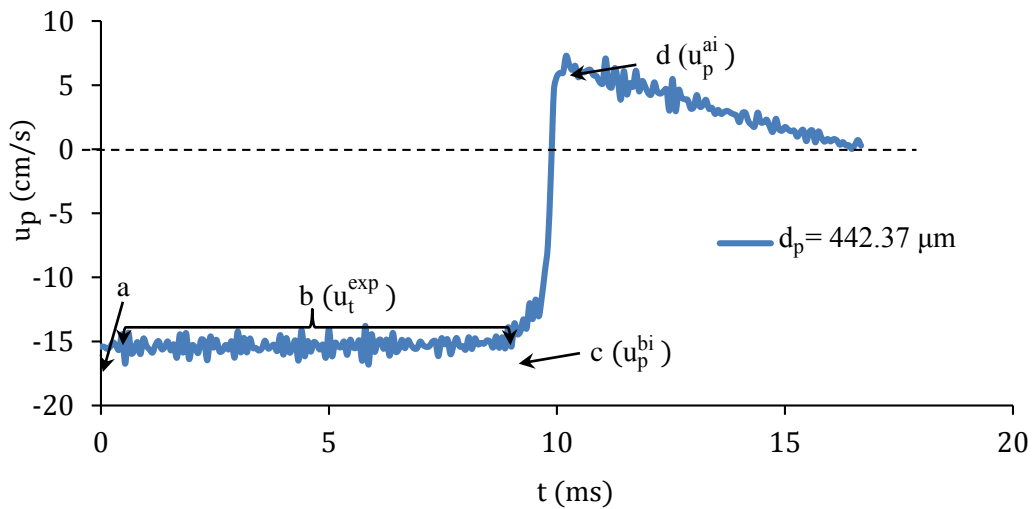


Fig. 3.3 Measured velocity of a zirconium dioxide particle in water ( $d_p = 442.37 \mu\text{m}$ ).

Further, the Fig. 3.4 shows that the experimentally measured sedimentation velocities of all the particles are within the  $\pm 10\%$  error associated with the correlations available in the literature.<sup>159–162</sup> Thus the experimental procedure is validated for the measurement of the particle velocity in a viscous fluid. For the particles in the air, sedimentation velocity is not achieved so the data is not included in the Fig. 3.4.

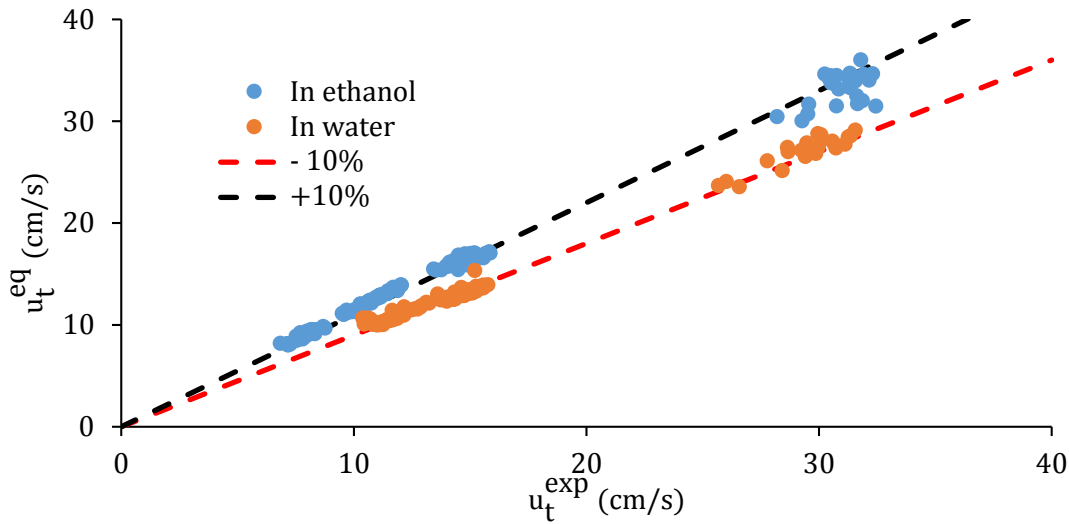


Fig. 3.4 Comparison of the experimentally measured terminal velocity with the terminal velocity predicted by the Eq. 3.4.

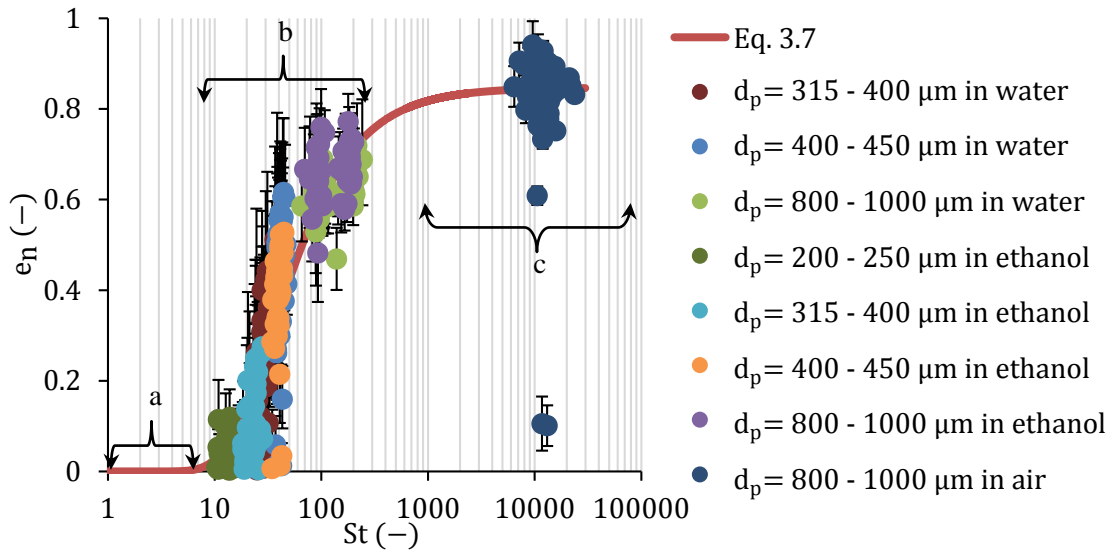


Fig. 3.5 Variation in the coefficient of restitution with respect to the Stokes number.

### 3.2.4 Sources of error

One of the uncontrollable sources of errors is the inconsistent point/area of impact. Even though the position of the vacuum nozzle is fixed, due to the fluid forces acting on the particles the point/area of impact cannot be controlled. Under the same conditions, this can lead to different topology of the surfaces in contact and eventually different values of the coefficient of restitution.

The light source generates heat energy which can influence the properties of the fluid. This error is minimized by changing the fluid after each reading.

Further, the Matlab script processes the data at the pixel scale, this introduce an error when the particle and the bottom share a pixel at the point of impact. The cumulative error of all these errors is shown in the Fig. 3.5 with the help of the error bars.

### 3.2.5 Results and discussion

The experimental coefficient of restitution is calculated using the Eq. 3.6.

$$e_n = \frac{|\overrightarrow{u_p^{ai}}|}{|\overrightarrow{u_p^{bi}}|} \quad 3.6$$

Here,  $\overrightarrow{u_p^{bi}}$  and  $\overrightarrow{u_p^{ai}}$  are the velocities of the particle before and after the impact (Fig. 3.3).

The Fig. 3.5 shows the variation of the coefficient of the normal restitution ( $e_n$ ) with respect to the Stokes number (St). It is observed that the zirconium dioxide particles do not show any appreciable coefficient of restitution for a Stokes number less than 7 (part a, Fig. 3.5). Whereas, for the Stokes number greater than 1000 the coefficient of restitution has an average value of 0.846 (part c, Fig. 3.5). This value corresponds to dry coefficient of normal restitution. In the experiments the maximum achieved impact velocity was 56 cm/s. The coefficient of restitution shows a huge variation from 0 to 0.72 for the Stokes number in the range of 7 to 250 (part b, Fig. 3.5). The Eq. 3.7 is based on the regression analysis of the experimental data and captures the complete variation.

$$e_n = 0.846 \times \exp\left(-\frac{34.8}{St}\right) \quad 3.7$$

This equation is similar to the one obtained by Legendre et al.<sup>69</sup> but the values of the coefficient of restitution for zirconium dioxide particles ( $d_p = 200 - 1000 \mu\text{m}$ ) are lower by 8%.

The possible reasons are:

- a) The data used by Legendre et al.<sup>69</sup> was based on the glass particles larger than  $1000 \mu\text{m}$ . Here, zirconium dioxide particles in the range of  $200$  to  $1000 \mu\text{m}$  are used.
- b) The roughness of the particles used by Legendre et al.<sup>69</sup> is not known. The zirconium dioxide particles used in the present experiments have an average roughness of  $0.01$  times the particle radius.
- c) For the micron sized particles, the inertial forces are comparable to the attractive forces. The presence of the attractive forces provides additional damping when the surfaces are in contact. This results in a lower value for the coefficient of restitution.
- d) The initial energy to the particle in the experimental data<sup>70</sup> used by Legendre et al.<sup>69</sup> was provided with the help of a string attached to the particle (pendulum like motion). In this case, the gravitational force was acting in the tangential direction to the point/area of contact. In the present configuration it acts in the perpendicular direction to the point/area of contact. This difference in the direction of the gravitational force also contributes for lower values of the coefficient of restitution recorded in our experiments.

### 3.3 Coefficient of sliding friction

When the bodies in contact have a sliding motion, a resistance is offered by the contact point/area at rest (static) and during the sliding (kinetic) of the bodies.<sup>164–166</sup> For the dry surfaces in contact, large data sets<sup>74,75</sup> for the coefficient of sliding friction ( $\mu_s$ ) are available in the literature.

There are very few studies in the literature which report the coefficient of sliding friction between the particles in the presence of the fluid. In the experimental study of Joseph and Hunt<sup>72</sup> the theory of oblique impacts<sup>153,167</sup> was used to study the effect of

the surrounding liquid on the coefficient of the sliding friction. The theory of oblique impacts, needs the measurement of the particle velocities (the linear and the angular velocities). Some of techniques to measure the particle velocities are:

1. Connecting a string to a particle (pendulum motion). The trajectory of the string can be used to calculate the linear and angular velocities.
2. Marking the particle with the reference points. The linear and the angular velocities are calculated by tracking the reference points.

Both these techniques are not practical for the micron sized particles (250 to 1000  $\mu\text{m}$ ). Hence, we use a technique where the normal sliding force is measured. The details of this technique are presented in the following sections.

### 3.3.1 Experimental setup

The schematic of the experimental setup is as shown in the Fig. 3.6. It consists of:

- 1) A top open box (stainless steel,  $220 \times 80 \times 5$  mm, Fig. 3.7).
- 2) A top plate ( $60 \times 60 \times 10$  mm, Fig. 3.7).
- 3) Adjustable weights ( $W$ , 17.78, 22.95 and 26.08 N), for the application of the normal load.
- 4) A string to pull the top plate at a constant shear velocity.
- 5) A force measurement device,<sup>168</sup> with a max measurable force of 49.05 N.
- 6) A data storage and processing device.

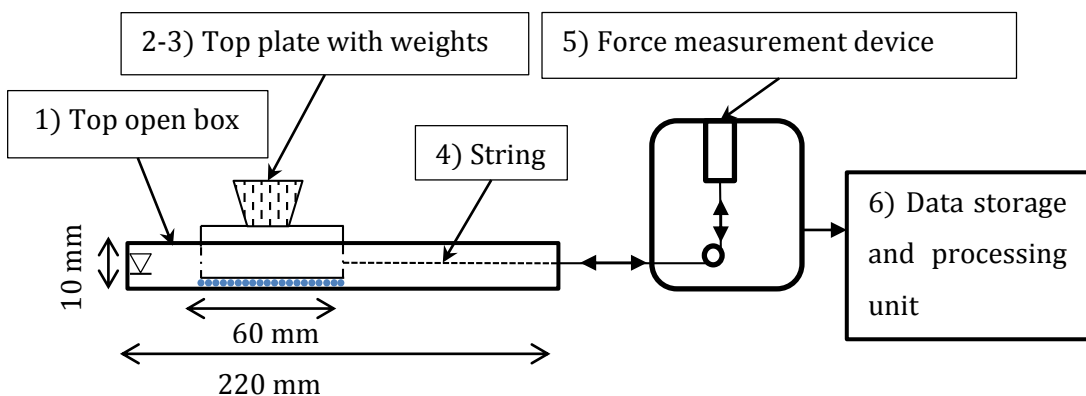


Fig. 3.6 Schematic of the experimental setup to measure the sliding coefficient.

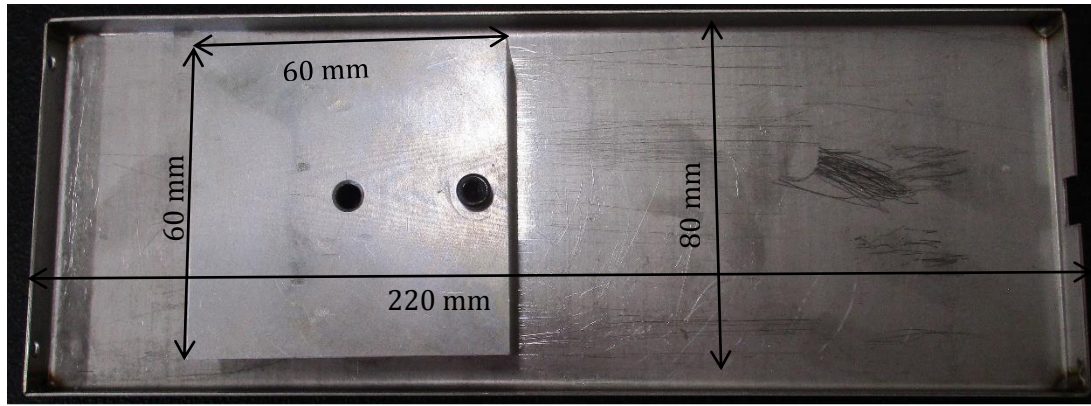


Fig. 3.7 Top view of the top open box and the top plate.

### 3.3.2 Procedure

For the measurement of the coefficient of sliding friction, mono-dispersed zirconium dioxide particles ( $d_p = 250 - 1000 \mu\text{m}$ ) are glued<sup>169</sup> to the top plate such that the surface of the plate is occupied by the particles and only a single layer of particles is formed (Fig. 3.8). The particles are also glued to the bottom plate of the top open box when the particle-particle sliding friction is measured.

A string which applies a shear force ( $\vec{f}_s$ ) is connected to the top plate. Then the top plate is placed on the bottom plate. This is followed by the placement of the weights on the top plate. The other end of the string is connected to the force measurement devices.<sup>168</sup>

The force measurement device pulls the top plate to a distance ( $X_s$ ) of 80 mm. The sliding shear velocity ( $U_s$ ) of 1 mm/s is maintained. Wet conditions are obtained by filling the top open box with water up to a height of 2 mm.



Fig. 3.8 Top plate with glued zirconium dioxide particles ( $d_p = 250 \mu\text{m}$ ).

### 3.3.3 Sources of error

Errors can arise due to the inconsistent distribution of the normal load (weights) to the particles. This error is minimized by taking readings at 3 different weights ( $W$ , 17.78, 22.95 and 26.08 N) and each experiment is repeated 3 times. The difference in the surface roughness and the number of contacts can affect the shear force. The sensitivity of such factors is minimized by using a sufficiently large number of mono-dispersed particles on the top and bottom plate.

### 3.3.4 Results and discussion

The shear force ( $\vec{f}_s$ ) required to sustain a constant shear velocity ( $U_s$ ) of 1 mm/s is recorded by the force measuring device. The Fig. 3.9 shows a sample recording of the measured and the averaged shear force ( $\overline{f}_s$ ) for the particles ( $d_p = 1000 \mu\text{m}$ ) in contact with the plate in the wet conditions. Fluctuations are observed in the measurement of the shear force. This is due to the well-known stick-slip phenomenon for two sliding surfaces.<sup>170</sup>

The values of the calculated coefficient of sliding friction based on the measured shear forces are given in the Annexure A.1. The summary of the measured coefficient of the sliding friction is given in the Table 3.1.



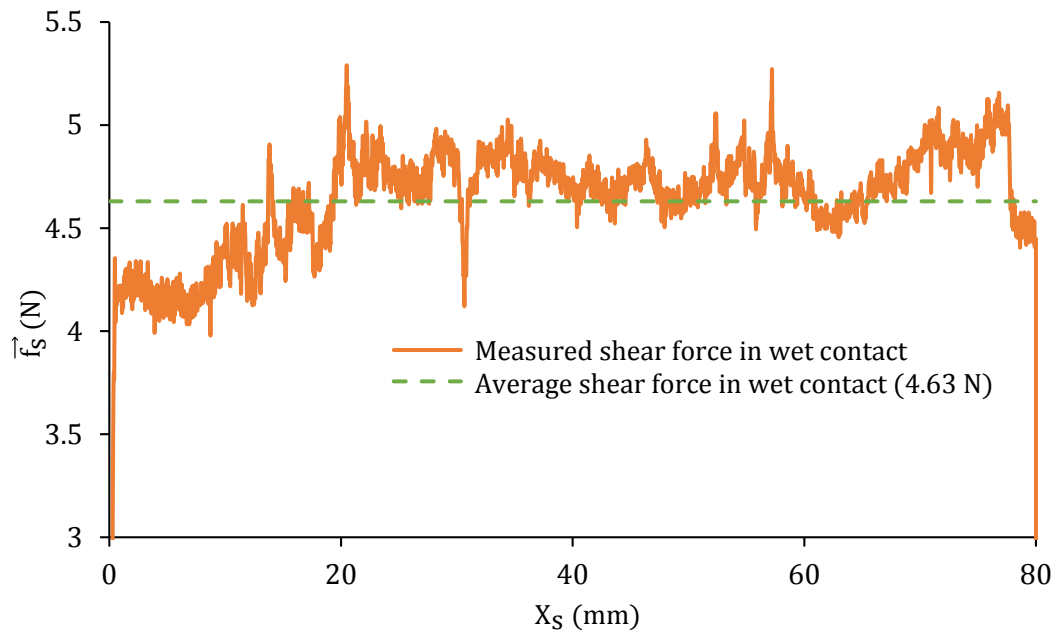


Fig. 3.9 A typical shear force displacement curve for the particle (zirconium dioxide  $d_p = 1000 \mu\text{m}$ ) -plate in a wet contact.

Table 3.1 Summary of the experimentally measured coefficient of the sliding friction.

Object 1	Object 2	Contact	Average coefficient of friction
-	-	-	$\mu_s$
Particles	Plate	Dry	0.252
Particles	Plate	Wet	0.222
Particles	Particles	Dry	0.301
Particles	Particles	Wet	0.285

It is observed that, in general the coefficient of sliding friction between the particle-plate is lower than the particle-particle contact. Further, there is only a slight reduction in the coefficient of the sliding friction due to the presence of water.

This can be explained as follows, the thickness of the fluid present between the surfaces in contact is given by the Eq. 3.8.<sup>171</sup>

$$h_m = 4.338R \left( \frac{\eta_f U_s \hat{\eta}}{R} \right)^{5/7} \left( \frac{W}{E^* R^2} \right)^{-1/21} \quad 3.8$$

Here,  $R$ ,  $\eta_f$ ,  $U_s$ ,  $W$  and  $E^*$  are the radius of the particle, the dynamic viscosity of the fluid, the sliding velocity, the normal weight and the effective Young's modulus, respectively.  $\hat{\eta}$  is the strained viscosity which is calculated using Eq. 3.9.<sup>172</sup>

$$\hat{\eta} = \frac{\left(\frac{\eta_f^P}{\eta_f^0}\right)^{\frac{1}{16}} - 1}{P} \quad 3.9$$

Here,  $\eta_f^0$  and  $\eta_f^P$  are the dynamic viscosity of the fluid at a reference pressure (0) and at the contact pressure (P), respectively. Based on the data for water given by Cooper and Dooley,<sup>173</sup> the calculated value of  $\hat{\eta}$  is less than  $1.7 \times 10^{-11}$  suggesting that under the present experimental conditions, there is no layer ( $h_m \approx 0$ ) of water between the surfaces in contact.

Thus, the conducted experiments and the theory in the literature suggest that the presence of water has an insignificant amount of effect on the values of the coefficient of sliding friction.

The values of the coefficient of sliding friction obtained from the experiments are useful input parameters in the DEM-CFD simulations.



---

## 4 Numerical Studies

---

### 4.1 Introduction

The details of the numerical studies based on the volume averaged DEM-CFD approach are reported in this chapter. At first the simulation setup is described. Followed by an exercise to find an optimal ratio of the fluid cell size to the particle diameter. Thereafter, the implemented lubrication model is verified by comparing the coefficient of restitution predicted by the simulations to the experimentally measured values in the previous Chapter.

Then, the influence of the various factors on the packed beds/cakes is numerically studied. The types of particles considered in the numerical study are:

- 1) Spherical mono-dispersed
- 2) Spherical bi-dispersed
- 3) Non-spherical mono-dispersed

Based on the simulation data, correlations between the input parameters and the macroscopic properties (void fraction) are obtained.

### 4.2 Simulation setup

The simulation setup is defined by the domain configuration, the boundary and the initial conditions for the fluid and the particle phase. For the particle phase, the method used to generate the initial position of the particles is also important. The details describing the simulation setup are presented in this section.

### 4.2.1 Domain configuration, boundary and initial conditions

The boundary conditions for the vertical faces of the domain are periodic for both the phases. The periodic condition for the particle phase allows the particle-particle interactions between the particles that may be in contact across the vertically opposite faces and if the particle center crosses the vertical face, it re-enters from the vertically opposite face.<sup>42</sup> For the particles the bottom face acts as a wall in all the simulations.

In the sedimentation simulations, the fluid boundary conditions at the top and the bottom face are set to *outlet* and *wall*, respectively. Whereas in the simulations where the consolidation of the packed bed/cakes due to the fluid forces is studied, the top face has a prescribed constant *inlet velocity* ( $\overrightarrow{U_f^{\text{inlet}}}$ ) and a *pressure outlet boundary* condition is prescribed for the bottom face. The acceleration due to gravity acts in the negative Z direction.

The graphical representation and the mathematical formulation of the boundary conditions are provided in the Fig. 4.1 and the Table 4.1, respectively.

### 4.2.2 Initial condition of the particles

The initial positions of all the particles are randomly generated in the whole computational domain at the first particle (DEM) time step. The Park-Miller<sup>174</sup> algorithm is used for the generation of the particle positions with an additional criteria that the initial position of the particles is such that the particles should not overlap. At first all the big particles are generated based on the specified mass fraction ratio of the mixture at the randomly generated particle center positions. This is followed by the generation of the small particles based on the mass fraction ratio. On each of the processor assigned to the sub-domains, the random generation is carried out to reproduce the same distribution of the mass fraction/position of the particles. A sample of randomly generated particles is shown in the Fig. 4.1. The initial velocities of the particles are set to zero.

Table 4.1 Fluid phase boundary conditions

Case	Top		Bottom		Vertical sides
	$p$	$U_f$	$p$	$U_f$	
Sedimentation	$p = 0$	$\nabla \cdot (\overline{U_f}) = 0$	$\nabla p = 0$	$\overline{U_f} = 0$	Periodic
Consolidation	$\nabla p = 0$	$\overline{U_f} = \overline{U_f^{\text{inlet}}}$	$p = 0$	$\nabla \cdot (\overline{U_f}) = 0$	

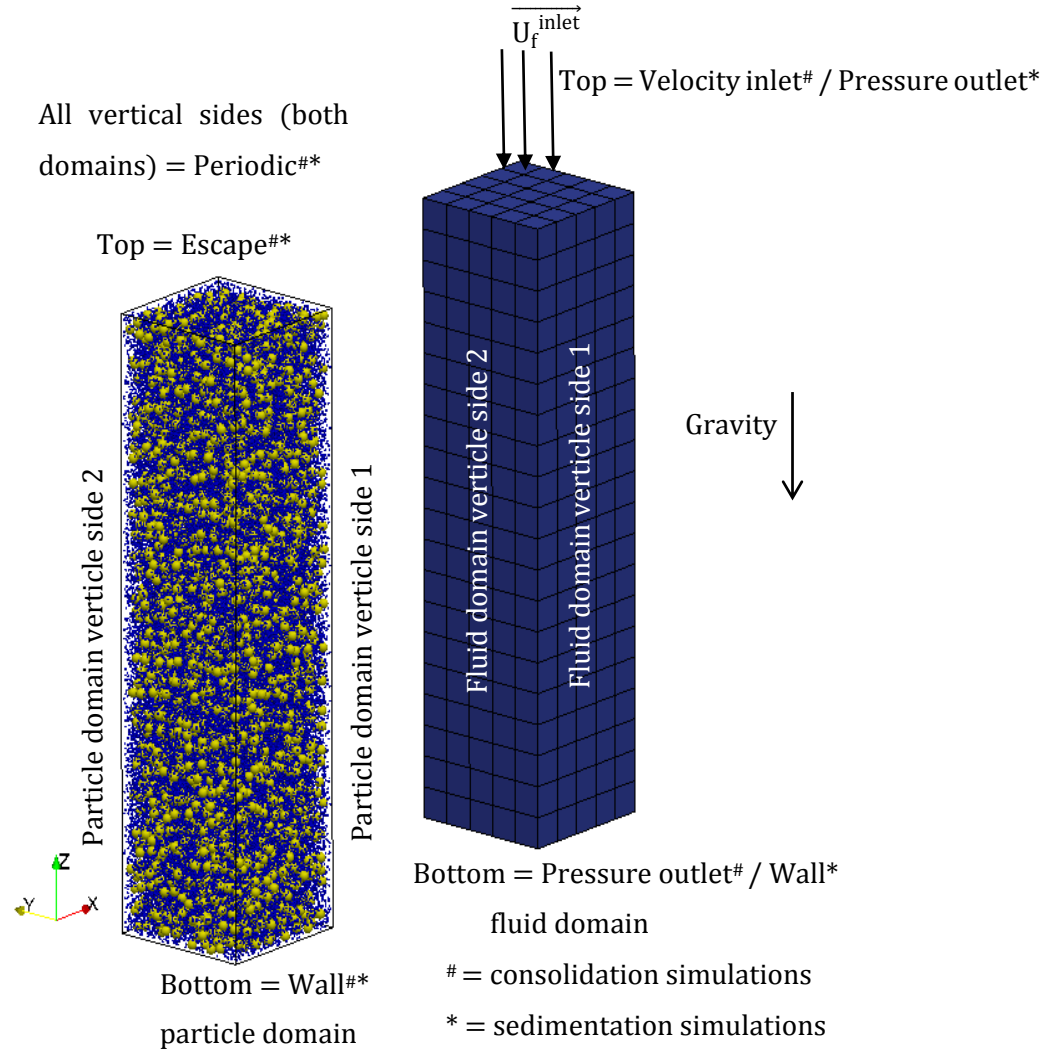


Fig. 4.1 The computational domain, the initial conditions and the boundary conditions for the particle and the fluid domain.

## 4.3 Spherical particles

### 4.3.1 Fluid cell size effect

In the volume averaged Eulerian-Lagrangian coupling, the cell size ( $h$ ) of the fluid cell (control volume) must be much larger than the particle diameter ( $d_p$ ). Studies in the literature have shown that the fluid cell affects the accuracy of the predictions. The *single particle momentum response* and the *volume averaging of the properties* are the two major criteria for which the cell size must be optimized. Therefore, two sets of numerical studies are carried out to find the optimal cell size to the particle diameter ratio. These studies are presented in the following sections.

#### 4.3.1.1 Particle momentum response

In the first study, the effect of the fluid cell size on the particle momentum response is studied. This is done by comparing the sedimentation velocity of a particle ( $d_p = 250 \mu\text{m}$ ,  $\rho_p = 6.06 \text{ g/cm}^3$ ) with the semi-empirical prediction by the Eq. 3.4.<sup>163</sup> The fluid considered here is ethanol ( $\rho_f = 0.789 \text{ g/cm}^3$ ,  $\eta_f = 0.0011 \text{ Pa}\cdot\text{s}$ ).

The Fig. 4.2 shows that, for the cell size to particle diameter ratio ( $h/d_p$ ) of 1, the particle velocity has an increasing trend accompanied by unrealistic oscillations. When the ratio is 2 the particle velocity stabilizes, but there are some unrealistic oscillations. For the ratio of 2.5, the magnitude of the unrealistic oscillations is reduced and the particle velocity stabilizes around a value of 8.38 cm/s this is higher than the terminal velocity of 8.19 cm/s predicted by the semi-empirical Eq. 3.4.<sup>163</sup> For the ratio of 3 the unrealistic oscillations are minimal and the particle velocity stabilizes around a value of 8.17 cm/s. This is in close agreement value predicted by the Eq. 3.5. For  $h/d_p = 5$  there are no oscillations, but the terminal value predicted by the simulations is 8.38 cm/s.

Thus, the studies show that the cell size to particle diameter ratio ( $h/d_p$ ) of 3 is sufficient enough to predict the particle momentum response.

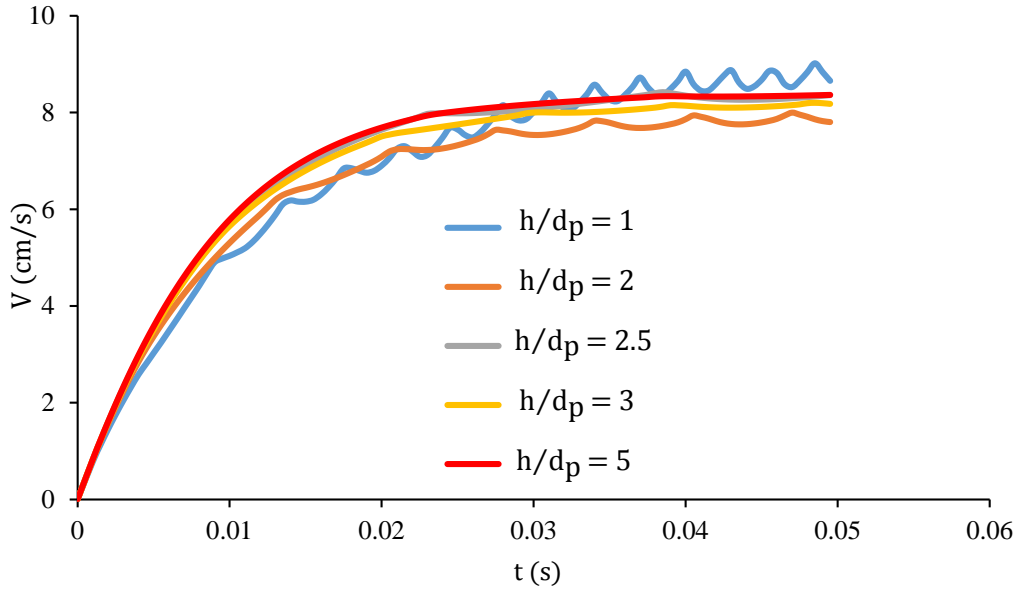


Fig. 4.2 Effect of the fluid size on the terminal velocity of a particle.

#### 4.3.1.2 Volume averaging of the properties

In the second study, the effect of the fluid cell size on the volume averaged properties is studied by comparing the pressure drop per unit height predicted by the DEM-CFD simulations with the Ergun equation (Eq. 4.1).

$$\frac{\Delta P}{H} = 182 \frac{\eta_f (1 - \varepsilon)^2 U_f}{\varepsilon^3 d_p^2} + 1.92 \frac{(1 - \varepsilon) \rho_f U_f^2}{\varepsilon^3 d_p} \quad 4.1$$

Here,  $\eta_f$ ,  $U_f$  and  $\varepsilon$  are the dynamic viscosity, velocity and the void fraction of the fluid phase.  $d_p$  is the particle diameter and  $H$  is the height of the packed bed/cake.

The simulations are carried out in two stages.

##### *First stage*

In the first stage of the simulations, a packed bed/cake is formed by sedimenting the mono-dispersed zirconium dioxide particles (Table 4.2) under the influence of the gravitational force only. The formed packed bed/cake has an average void fraction of



0.403 which is calculated using the height (H) measured as the position (z component) of the topmost particle.

Table 4.2 Simulation parameters used in the study to investigate the effect of cell size on the volume averaged properties

Property	Symbol	Values
Coefficient of restitution (-)	$e_n$	0.1
Coefficient of rolling friction (-)	$\mu_r$	0.002
Coefficient of sliding friction (-)	$\mu_s$	0.3
DEM time step (s)	$t_p$	$5 \times 10^{-7}$
Particle diameter ( $\mu\text{m}$ )	$d_p$	250
Poisson's ratio (-)	$\nu$	0.3
Total mass of the particles (g)	$m_p$	10
Young's modulus (GPa)	E	0.1

### *Second stage*

In the second stage the packed bed/cake bed is subjected to a fluid flow (ethanol,  $\rho_f = 0.789 \text{ gm/cm}^3$ ,  $\eta_f = 0.0011 \text{ Pa}\cdot\text{s}$ ,  $U_f = 0.01 \text{ cm/s}$ ). The fluid boundary conditions corresponding to the consolidation case (Table 4.1) are employed. The fluid cell size is varied and the pressure drop predicted by the DEM-CFD simulations are reported in the Table 4.3.

Table 4.3 Effect of the fluid cell size to the particle size ratio on the pressure drop predicted DEM-CFD simulations

$h/d_p$ (-)	Pressure drop per unit height (Pa/m)		Error (%)
	DEM-CFD	Eq. 4.1	
2	16526.22		5.23
2.5	16945.18	17437.44	2.82
3	17398.92		0.22
5	17405.09		0.18

It is observed that as the fluid cell size to the particle size ratio increase, the percentage error in the pressure drop per unit height is decreased. For the fluid cell size to the

particle size ratio of 3 the error is less than 1 %. Further for the ratio of 5 the decreases in the error is minimal. Feng<sup>175</sup> has suggested that cell size to the particle diameter ratio of 23 predicts the volume averaged properties with the least error and there is no certainty that an increase in the cell size will decrease the error. This is because in the study of Feng,<sup>175</sup> the void fraction of the fluid cell is calculated by assuming that the complete particle is in the fluid cell where its center lies. This assumption introduces large errors in the calculation of the volume averaged properties.

In the present study, the void fraction is calculated using the divided void fraction method (sec. 2.6) which has a higher accuracy in the prediction of the volume averaged properties. Therefore, very high cell size to the particle diameter ratio is not required. Thus, these studies have shown that the particle diameter ratio ( $h/d_p$ ) of 3 is a reasonable choice for the volume averaged DEM-CFD coupling. Therefore, this ratio is used in the simulation studies.

#### 4.3.2 Lubrication force

The Fig. 4.3 shows that the coefficient of the normal restitution ( $e_n$ ) predicted by the classical lubrication theory<sup>73,127</sup> is much higher than the value obtained in our experiments (sec. 3.2). This is due to two main reasons:

- 1) At higher Reynolds number ( $>3$ ) the effect of the lubrication force is amplified and an amplification factor must be considered in the modeling of the lubrication force.
- 2) The influence of the surface roughness of the particles must be considered in the theoretical modeling and numerical simulations.

In the DEM-CFD simulation these two effects are considered. The mathematical modelling of this is already presented in the sec. 2.4.1.

In the DEM-CFD simulation, a zirconium dioxide particle ( $d_p = 200 - 800 \mu\text{m}$ ) is allowed to sediment in ethanol. The average roughness of the zirconium dioxide particle is assumed to be 0.01 times the particle radius. The particle-wall contact coefficient of restitution is set to an experimentally obtained value of 0.846. The effective coefficient of normal restitution (lubrication + contact) in the DEM-CFD simulations is calculated using the Eq. 4.2.

$$e_n = \frac{|\overrightarrow{u_p^{al}}|}{|\overrightarrow{u_p^{bl}}|} \quad 4.2$$

Here,  $\overrightarrow{u_p^{bl}}$  is the particle velocity just before it enters the lubrication region and  $\overrightarrow{u_p^{al}}$  is the particle velocity after it comes out of the lubrication region.

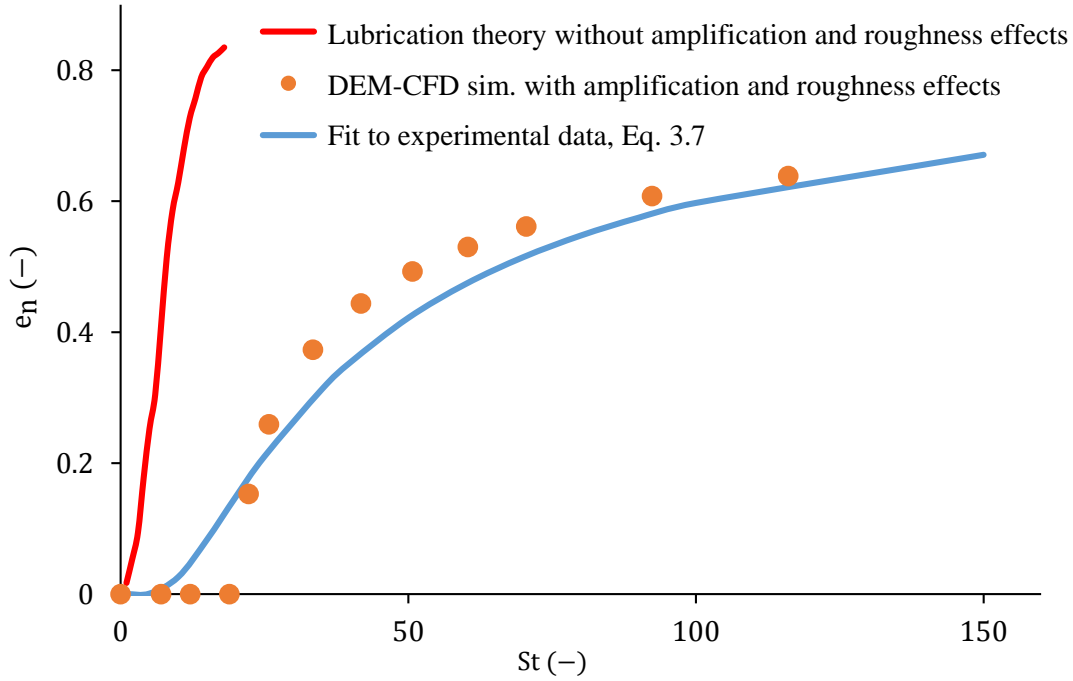


Fig. 4.3 Comparison of the normal restitution predicted by the DEM-CFD with the experimental measurements.

The Fig. 4.3 shows that the coefficient of the normal restitution predicted by the DEM-CFD is in close agreement with the experimental fit given by the Eq. 3.7. Thus, the mathematical model for the lubrication force and its implementation is validated

### 4.3.3 Sedimentation of non-dispersed particles

#### 4.3.3.1 Effects of the input parameters

The DEM simulations can predict the particle dynamics if the used contact model correctly describes the particle-particle/wall interactions and the input parameters of this model are close to the real material properties.<sup>14,176–178</sup>

The input parameters are listed as:

1. The Poisson's ratio ( $\nu$ ) and the Young's modulus ( $E$ ) representing the elastic stiffness of the particles.
2. The coefficient of normal restitution ( $e_n$ ) describing the energy loss due to viscous or plastic contact deformation.
3. The coefficients of frictions characterizing the sliding ( $\mu_s$ ) and rolling resistances ( $\mu_r$ ).
4. The work of adhesion ( $W_a$ ) which is a parameter in an adhesion model to consider the attractive forces.

The sensitivities of these input parameters are discussed in the following sections.

#### 4.3.3.2 Effects of the Young's modulus

The value of Young's modulus for glass spheres is in the range of 1 to 200 GPa.<sup>179–181</sup> Such high values of Young's modulus will lead to a lower contact time and a higher computational effort for the DEM simulation whereas a lower Young's modulus will reduce the computational effort but will increase the overlap. When the overlap is high, the void fraction is misrepresented. This affects the fluid velocity, the pressure fields and the interphase momentum transfer. As a thumb rule to avoid such misrepresentation, overlap should not exceed 2 % of the particle diameter. Based on the overlap criteria, a study by Norouzi et al.<sup>11</sup> has shown that for non-cohesive particles a Young's modulus in the range of 0.1 to 1 GPa is a good compromise between the computational effort and the accuracy.

The Young's modulus with a value of 0.1 GPa, Poisson's ratio of 0.3, and particle density of 2.5 g/cm<sup>3</sup> are used in the simulations where contact attractive force is neglected. Here, the choice of the Young's modulus and the Poisson's ratio in the simulation is justified as the change in the void fraction with the increase in the Young's modulus (0.1 to 1 GPa) for the mono-dispersed glass particles (Details in Table 4.4) falling under the influence of the gravity (in the absence of the fluid forces) is 0.0018.

Table 4.4 Simulation parameters used in the study to investigate the effect of the Young's modulus on the void fraction of packed beds.

Property	Symbol	Values
Coefficient of restitution (-)	$e_n$	0.91
Coefficient of rolling friction (-)	$\mu_r$	0.002
Coefficient of sliding friction (-)	$\mu_s$	0.3
DEM time step (s)	$t_p$	$(10^{-7}, 10^{-8})$
Total mass of the particles (g)	$m_p$	$2.9321 \times 10^{-3}$
Particle diameter ( $\mu\text{m}$ )	$d_p$	40
Work of adhesion ( $\text{mJ/m}^2$ )	$W_a$	(0, 5)

For the cohesive particles, Liu et al.<sup>182</sup> have shown that the prediction of properties like the minimum fluidization velocities are sensitive to the value of the Young's modulus. In such cases, an appropriate scaling parameter<sup>139</sup> (e.g. cohesion number) is used in this work to address the effect of the Young's modulus (sec. 4.3.3.5).

#### 4.3.3.3 Effects of the coefficient of restitution

The value of the coefficient of restitution can either be calculated for each particle based on the lubrication theory (sec. 2.4.1) or a constant equivalent value for all the particles calculated using the Eq. 3.2 could be used.

Both the approaches are explored to find out their influence on the final void fraction of the packed bed/cake. The glass particles ( $\rho_p = 2.5 \text{ g/cm}^3$ ,  $d_p = 40 \mu\text{m}$ ,  $m_p = 5.856 \times 10^{-4} \text{ g}$ ) are allowed to sediment in water. The coefficient of the sliding and rolling frictions are set to 0.6 and 0.02, respectively. The final void fraction of the sedimented packed bed/cake and the corresponding computation time is shown in the Table 4.5.

Table 4.5 Effect of the coefficient of restitution on the void fraction and the computation time

Case (-)	Void fraction (-)	Computation time (hrs)
Constant equivalent value	0.439	104
Lubrication theory	0.438	240

It is observed that the final void fraction in both the cases is nearly equal, but the computation time in the case where the coefficient of restitution is calculated using the lubrication theory is 2.33 times the case in which an average constant restitution is used. Thus, it can be concluded that using a constant equivalent coefficient of restitution is a cheaper alternative in terms of the computational effort.

#### 4.3.3.4 Effects of the coefficient of frictions

The sensitivity of the friction (sliding and rolling) on the void fraction of a mono-dispersed filter cake is investigated here by performing simulation studies. The sedimentation experiments of Onoda and Liniger<sup>57</sup> are used as a reference for the sensitivity analysis of the coefficients of friction. The particle diameter in these experiments was 250  $\mu\text{m}$ , and the particle-particle interactions were dominated by the sliding and rolling mechanisms. Hence, attractive forces are neglected in the simulations. The simulations are performed under the sedimentation conditions. The fluid properties ( $\rho_f = 1.01 \text{ g/cm}^3$ ,  $\eta_f = 1.03 \text{ mPa}\cdot\text{s}$ ) corresponding to glycerin with 5 % water at a temperature of 25°C are used.<sup>183</sup> Details of the other parameters used in this study are given in the Table 4.6.

Table 4.6 Simulation parameters used in the study to investigate the effect of friction coefficients on the void fraction of the mono-dispersed glass particles

Property	Symbol	Values
Coefficient of sliding friction (-)	$\mu_s$	(0.03, 0.1, 0.3, 0.6, 0.9)
Coefficient of rolling friction (-)	$\mu_r$	(0.002, 0.02, 0.2)
DEM time step (s)	$t_p$	$10^{-6}$
Fluid time step (s)	$t_f$	$2 \times 10^{-4}$
Total mass of the particles (g)	$m_p$	0.71

The Fig. 4.4 shows the variation of the void fraction with respect to the coefficients of sliding and rolling friction obtained by DEM-CFD simulation. The void fraction increases with the increase in the coefficients of frictions. There is a considerable increase in the void fraction ( $\Delta\varepsilon = 0.041$ ) when the values of the coefficients of friction are increased from nearly frictionless ( $\mu_s = 0.03$ ,  $\mu_r = 0.002$ ,  $\varepsilon = 0.379$ ) to a considerable frictional resistance ( $\mu_s = 0.3$ ,  $\mu_r = 0.002$ ,  $\varepsilon = 0.42$ ).

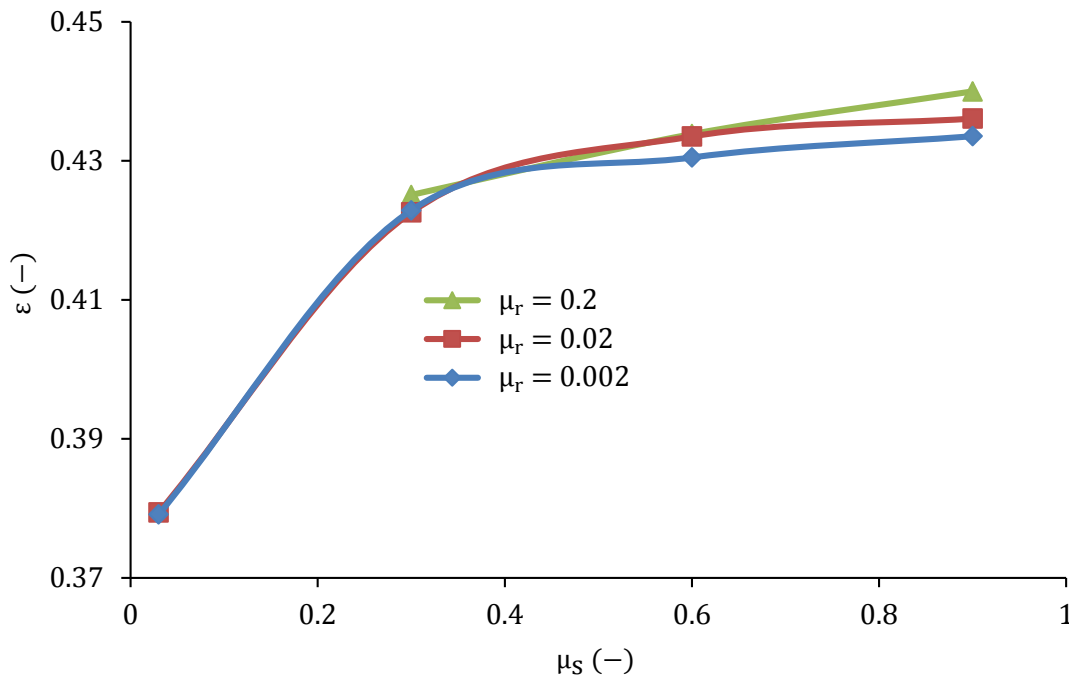


Fig. 4.4 The effect of the coefficients of sliding ( $\mu_s$ ) and rolling ( $\mu_r$ ) friction on the void fraction ( $\varepsilon$ ) of a filter cake.

This can be explained as follows, when the coefficients of friction are low ( $\mu_s = 0.03$ ,  $\mu_r = 0.002$ ) the particles slide and roll over each other to form a dense packing, whereas higher values of coefficient of frictions offer higher resistance to sliding and rolling which results in a bridge like structure. The formation of the particle bridges results in a higher value of void fraction.

It is also observed that the effect of the coefficient of rolling friction is negligible for the values of coefficient of sliding friction less than 0.6. Setting the coefficient of sliding and rolling friction to 0.6 and 0.002, respectively, gives a void fraction of

$0.43^{+0.001}_{-0.001}$  (deviation based on the difference in height measurements in the 5 different simulations by changing the initial seed of the random generator). The sedimentation experiments of Onoda and Liniger<sup>57</sup> have shown that the packing of similar mono-dispersed spherical glass particles result in a void fraction of  $0.43^{+0.003}_{-0.001}$ . This value is higher as compared to the similar experiments under dry conditions performed by Scott and Kilgour.<sup>56</sup> This is due to the presence of the liquid in the experiments of Onoda and Liniger<sup>57</sup> which leads to lower energy of the particles before impact (lower sedimentation velocity). This lower energy before the impact and the loss of energy during impact restricts the movement (sliding, rolling) of the particles leading to a higher void fraction.

The Eq. 4.3 represents a correlation between the void fraction ( $\varepsilon$ ) and the coefficients of frictions ( $\mu_s, \mu_r$ ). This equation is based on a regression analysis of the simulation data.

$$\frac{\varepsilon}{\varepsilon^*} = \frac{11.651 + 1.162 \left( \frac{\mu_s + \mu_r}{\mu_s^* + \mu_r^*} \right)^{1.496}}{11.865 + \left( \frac{\mu_s + \mu_r}{\mu_s^* + \mu_r^*} \right)^{1.496}} \quad 4.3$$

Here  $\varepsilon^*$ ,  $\mu_s^*$ , and  $\mu_r^*$  are the minimum void fraction (0.379) corresponding to the minimum values of the coefficient of sliding (0.03) and rolling friction (0.002), respectively.

The Fig. 4.5 shows a comparison between the simulation results and the approximation according to Eq. 4.3, which can be used to predict the void fraction in the absence of the attractive forces.



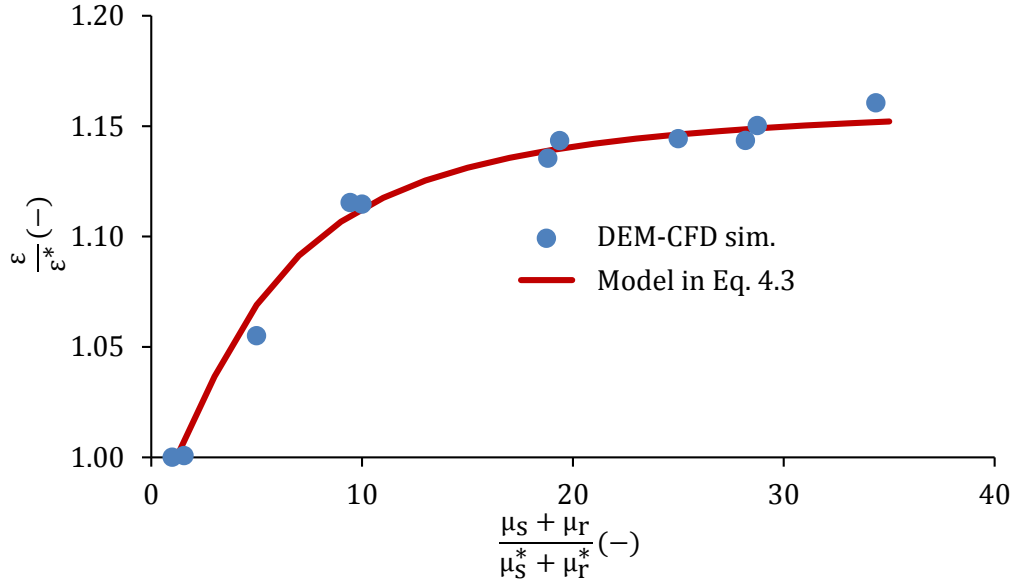


Fig. 4.5 Fit of the model in Eq. 4.3 to the DEM-CFD simulation results.

#### 4.3.3.5 Effect of the attractive forces

Numerical studies in the literature<sup>60,63,184</sup> have shown that higher the ratio of the particle-particle attractive forces to the gravitational force, higher is the void fraction of the packed bed/cake. In DEM, the particle-particle attractive forces are calculated based on the JKR theory and lower values of Young's modulus are used in order to reduce the computational effort. The correlations available in the literature<sup>60,63,184</sup> do not consider the effects due to the models used in the simulations and the compromised Young's modulus. In this study, these influences are considered by using the cohesion number given by the Eq. 4.4.<sup>139</sup>

$$Cn = \frac{0.211}{(\rho_p - \rho_f)g} \left( \frac{W_a^5}{(E^*)^2 (R^*)^8} \right)^{1/3} \quad 4.4$$

Here,  $W_a$  is the work of adhesion,  $E^*$  and  $R^*$  the effective Young's modulus and the effective radius of the particles in contact.  $\rho_f$  is the fluid density. The derivation of the cohesion number corresponding to the JKR theory is found in the work of Behjani et al.<sup>139</sup> Simulations are carried out to find a correlation between the void fraction of the packed bed/cake.

In the simulations, glass particles ( $\rho_p = 2.5 \text{ g/cm}^3$ ,  $d_p = 160 \text{ }\mu\text{m}$ ,  $m_p = 0.03211 \text{ g}$ ,  $\mu_r = 0.002$ ,  $e_n = 0.1$ ) are allowed to sediment in the water ( $\rho_f = 1 \text{ g/cm}^3$  and  $\eta_f = 1 \text{ mPa}\cdot\text{s}$ ) and the cohesion number is varied by changing the work of adhesion. Based on the regression analysis of the simulation data, a correlation between the void fraction and the cohesion number is given by the Eq. 4.5.

$$\varepsilon = \frac{0.0579\varepsilon^* + 0.7\text{Cn}^{0.4731}}{0.0579 + \text{Cn}^{0.4731}} \quad 4.5$$

Here,  $\varepsilon^* = 0.438$  is the void fraction of the packed bed/cake at  $\text{Cn} = 0$ . The comparison between the void fraction predicted by the Eq. 4.5 and the simulations is shown in the Fig. 4.6. Further, the void fraction is sensitive to the coefficient of friction and a lower void fraction is achieved with a decrease in the coefficient of frictions (Fig. 4.6).

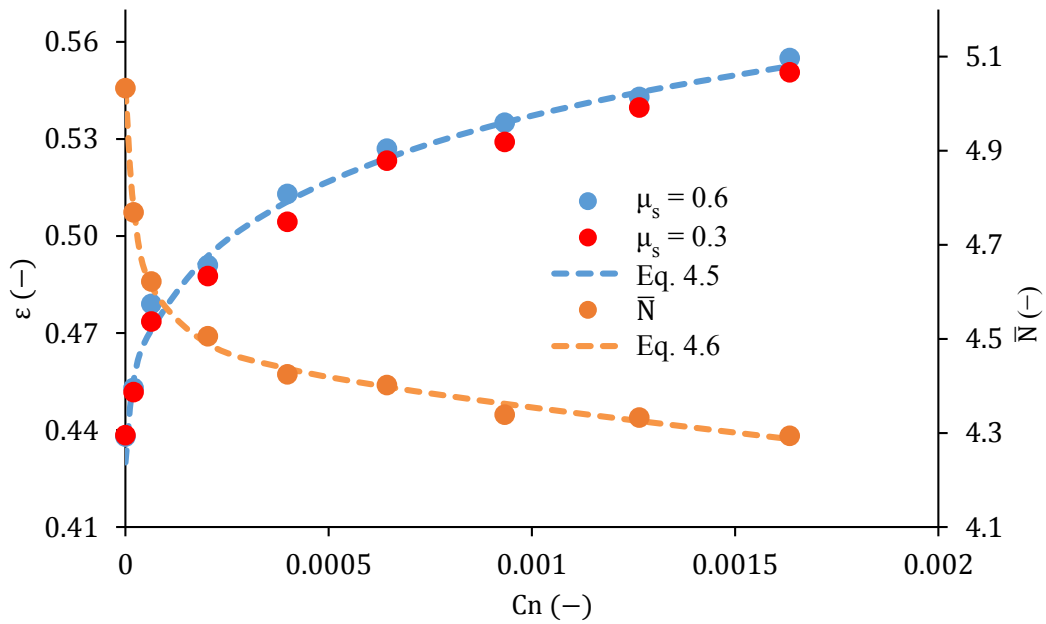


Fig. 4.6 Variation of the void fraction and the mean coordination number with respect to the cohesion number.

Unlike the gravitational force, the attractive force has no preferred direction. It depends on the number of contact surfaces and their positions. Theoretically, the coordination number (the number of contacts for a particle) is in the range of 1 to 12.<sup>185</sup> For the

simulated packed beds/cakes the coordination number has a frequency distribution as shown in the Fig. 4.7. It is observed that most of the particle in a packed bed/cake have the coordination number in the range of 3 to 7. The cohesion number influence the distribution of the coordination number. In general, the mean coordination number decreases with an increase in the cohesion number.

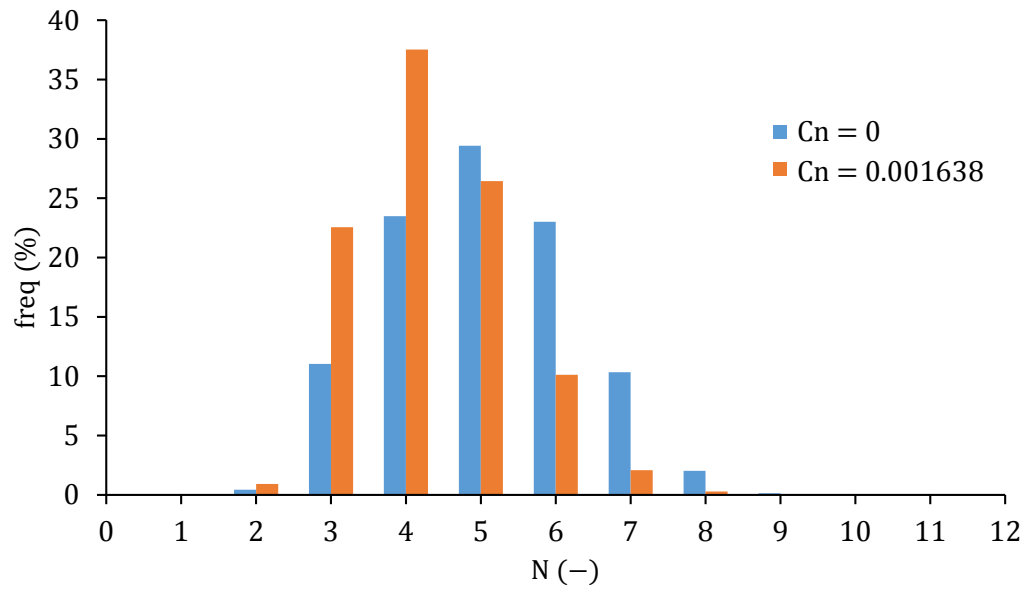


Fig. 4.7 The frequency distribution of the coordination number.

Based on the simulation data, the Eq. 4.6 shows the relationship between the mean coordination number and the cohesion number.

$$\bar{N} = \frac{5.033 + 158982Cn}{1 + 35838Cn + 827082Cn^2} \quad 4.6$$

The Fig. 4.8 shows the force network of the packed beds/cakes at the cohesion number of 0 and 0.001638. Here the solid lines are the connections between the centers of the particles in contact through which the forces are transmitted.

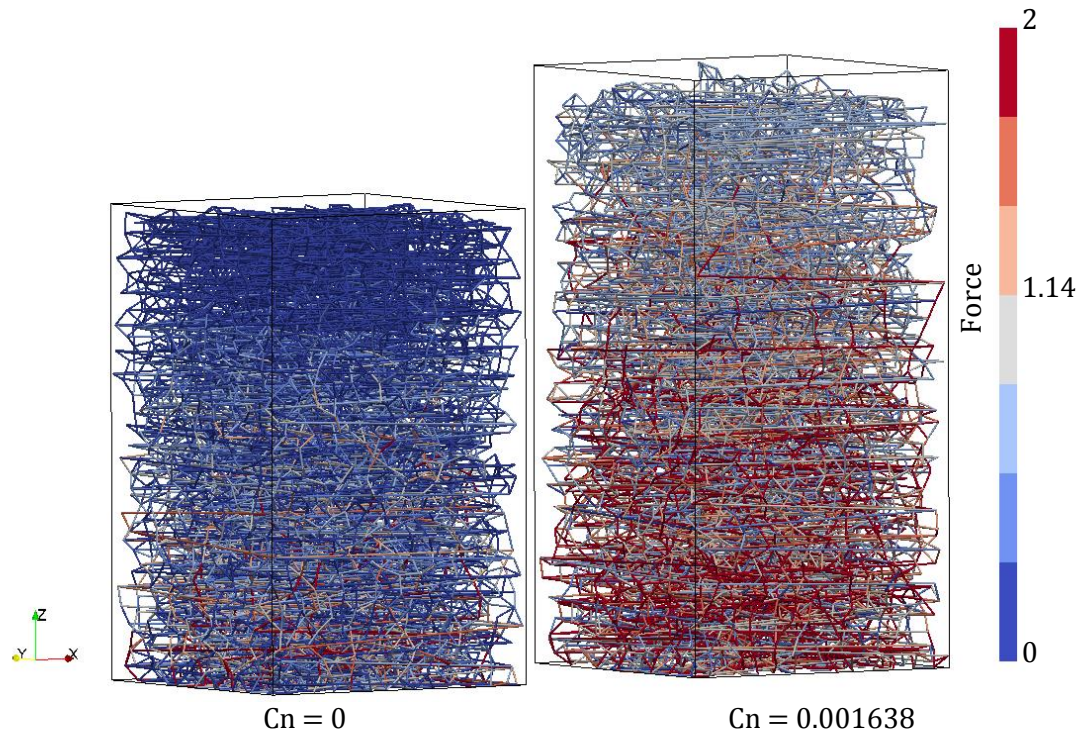


Fig. 4.8 Force network of the packed beds/cakes.

The magnitude of the force in the lower layers is higher. This is because the particles in the lower layers have to support the weights of the particles in the layer above them. Further, the particle-particle attractive force increases the magnitude of the forces in the links resulting in the stability of the packed bed/cake at a higher void fraction.

#### 4.3.3.6 Consolidation due to the fluid forces

The effects of the flow conditions on the packed beds/cakes are studied by first creating packed beds/cakes (particle structures) where the gravitational force is considered and the fluid and the attractive forces are neglected. The formed dry packed beds/cakes are subjected to different flow conditions by providing different fluid velocities at the top face (consolidation simulations). Depending on the fluid flow through the filter cake and the particle-particle interactions, the particles are free to re-arrange which can result in a change in void fraction (consolidation).

The pressure drop per unit height across the mono-dispersed particle structure formed due to glass particles with the properties given in Table 4.6 is studied. The particles

without the fluid forms a dry packed bed/cake with a void fraction ( $\varepsilon_d$ ) of 0.41 when the coefficient of sliding and rolling friction are set to 0.6 and 0.002, respectively.

The fluid is assumed to be glycerin with 5 % water at a temperature of 25°C ( $\rho_f = 1.01 \text{ g/cm}^3$ ,  $\eta_f = 1.03 \text{ mPa}\cdot\text{s}$ ).

The pressure drop per unit height based on the initial void fraction at different Reynolds numbers (Eq. 4.7) using the Ergun equation<sup>47</sup> (Eq. 4.1) are plotted in the Fig. 4.9.

$$\text{Re}_p = \frac{\rho_f U_f \langle d_p \rangle}{\eta_f} \quad 4.7$$

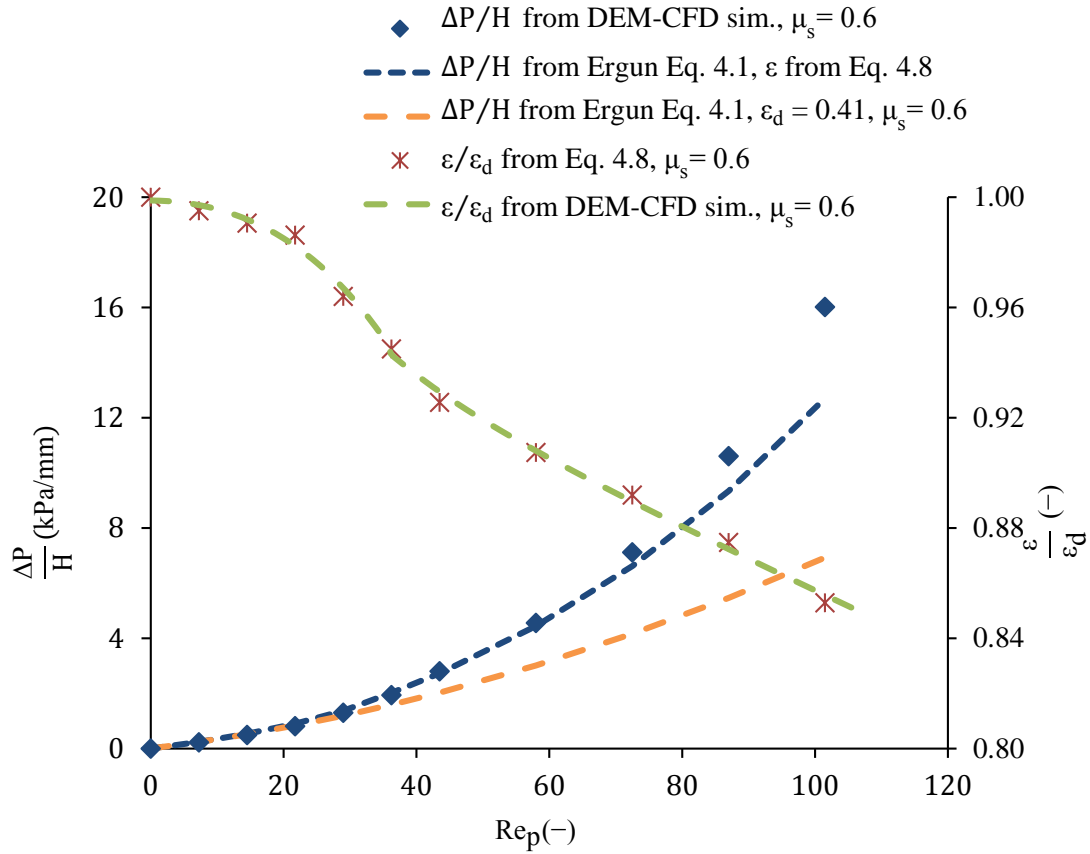


Fig. 4.9 Comparison of the pressure drop obtained with the DEM-CFD simulations, Ergun equation with dry void fraction (0.41) and with void fraction predicted by DEM-CFD simulations and Eq. 4.8.

Fig. 4.9 shows that for Reynolds number less than 29, the simulated pressure drop per unit height is in agreement with the one calculated using the initial void fraction of the dry packed bed/cake in the Ergun equation<sup>47</sup> but for the Reynolds number greater than 29 the pressure drop calculated using the Ergun equation is lower than the DEM-CFD prediction. The higher pressure drop per unit height obtained in the simulations is due to the consolidation of the packed bed/cake owing to the fluid forces.

The evidence of consolidation can be seen from the variation of the void fraction ratio ( $\varepsilon/\varepsilon_d$ ) with respect to the Reynolds number (Fig. 4.9) where a considerable drop is observed in the void fraction for a Reynolds number greater than 29. The Eq. 4.8 represents a correlation for the final consolidated void fraction ( $\varepsilon$ ).

$$\frac{\varepsilon}{\varepsilon_d(0.41)} = \begin{cases} \frac{0.998 - 0.01048 \cdot Re_p}{1 - 0.0104 \cdot Re_p + 0.0000264 \cdot Re_p^2} & 5 < Re_p < 29 \\ 0.964 - 0.00109 \cdot Re_p + \frac{24.135}{Re_p^2} & 29 \leq Re_p < 80 \end{cases} \quad 4.8$$

Here,  $\varepsilon_d(0.41)$  is the initial dry void fraction.

The Fig. 4.9 also shows the use of the Eq. 4.8 to predict the consolidation effect observed in the DEM-CFD simulations for the Reynolds number in the range of 5 to 80, beyond which the coefficient (182, 1.92) suggested by Fand et al.<sup>123</sup> are not valid and the pressure drop per unit height is lower than the DEM-CFD simulations. It should also be noted that the Eq. 4.8 is valid when the coefficient of sliding friction is 0.6.

The consolidation of the formed packed bed/cake is also sensitive to the coefficient of friction. In order to understand this sensitivity further simulations are performed, the coefficient of sliding friction is varied and is set to values of 0.3 and 0.1 (Table 4.6). The initial void fractions of the packed bed/cake formed under dry conditions with the coefficient of frictions 0.3 and 0.1 are 0.403 and 0.381, respectively.

The formed dry packed beds/cakes are subjected to different fluid flow conditions. The pressure drops per unit height and the corresponding void fractions are shown in the Fig. 4.10. It is observed that the Reynolds number beyond which a considerable consolidation is observed decreases from 29 ( $\mu_s = 0.6$ ) to 21.75 ( $\mu_s = 0.3$ ) and 14.75

( $\mu_s = 0.1$ ). Further, for the same Reynolds number the formed packed bed/cake undergoes greater amount of consolidation with the reduction in the coefficient of sliding friction.

The consolidated void fraction reaches a value of 0.2626 ( $\varepsilon/\varepsilon_d = 0.687$ ) at the Reynolds number of 58, when the coefficient of friction is set to 0.1. This value is very close to the lowest theoretical value of 0.259 (random packing for mono-dispersed spheres).<sup>185</sup> Hence, in order to adhere to the theoretical limit the pressure drop per unit height beyond the Reynolds number of 58 is calculated by using the void fraction value of 0.259 in the Ergun equation (Fig. 4.10).

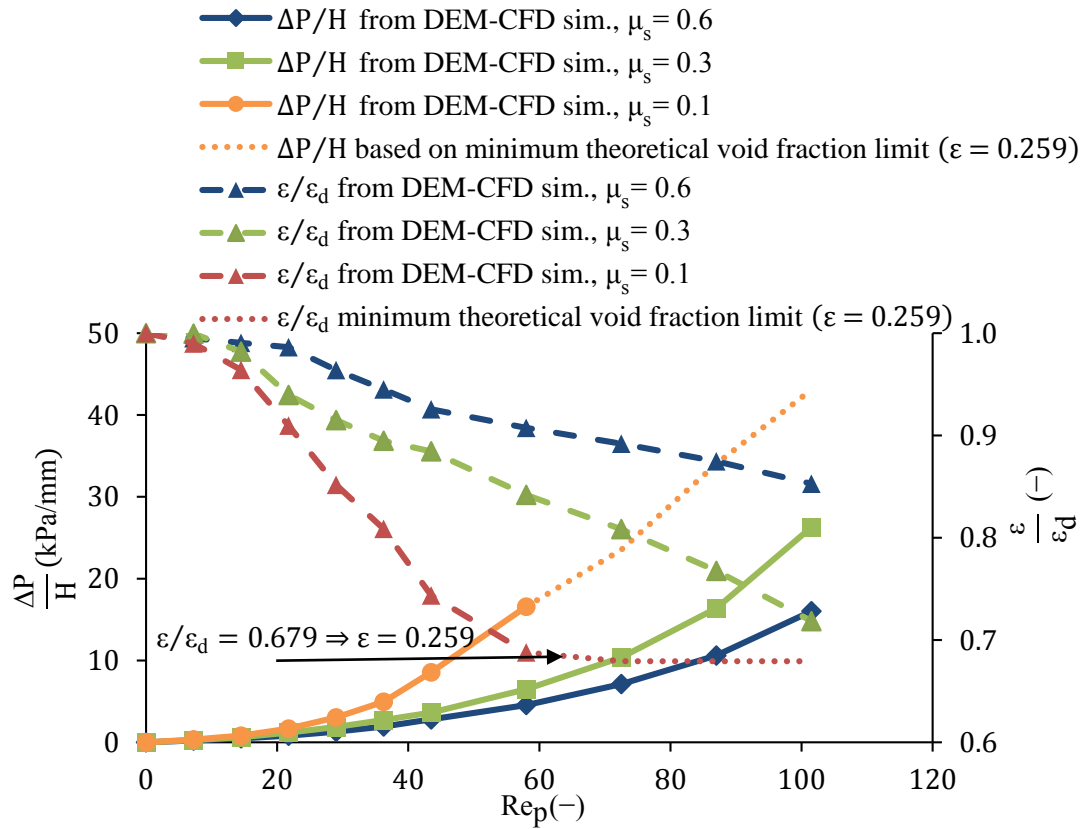


Fig. 4.10 Effect of the fluid flow condition and the coefficient of sliding friction on the consolidation of the packed bed/cake

### 4.3.4 Sedimentation of the bi-dispersed particles

#### 4.3.4.1 Effects of the mass fraction and the attractive forces

In this section, the effects of the mass fraction and the attractive forces on the formation of the packed bed/cake are discussed. The particle size ratio ( $d_b : d_s$ ) is 4 : 1. The particles are sedimenting in glycerin ( $\rho_f = 1.01 \text{ g/cm}^3$ ,  $\eta_f = 1.4 \text{ mPa}\cdot\text{s}$ ) with 5 % water at a temperature of  $11.5^\circ\text{C}$ .<sup>183</sup> The parameters used in this study are summarized in Table 4.7.

Table 4.7 The particle parameters to study the effect of attractive force

Property	Symbol	Values
Coefficient of sliding friction (-)	$\mu_s$	(0.3, 0.6)
Coefficient of rolling friction (-)	$\mu_r$	0.02
Big particle dia. ( $\mu\text{m}$ )	$d_{pb}$	160
Small particle dia. ( $\mu\text{m}$ )	$d_{ps}$	40
Work of adhesion ( $\text{mJ/m}^2$ )	$W_a$	(0, 5)
DEM time step (s)	$t_p$	$10^{-7}$
Fluid time step (s)	$t_f$	$10^{-5}$
Total mass of particles (g)	$m_p$	$(5.856 \times 10^{-4}, 0.03211)$
Mass fraction ratio (-)	$m_b : m_s$	(0 : 1, 0.25 : 0.75, 0.35 : 0.65, 0.5 : 0.5, 1 : 0)

Fig. 4.11 shows the effect of the attractive force, the coefficient of sliding friction and the particle mass fraction ratio on the void fraction of the sedimented packed beds/cakes. The experimental results of Shapiro and Probst<sup>58</sup> are used as the reference values for the sensitivity study. When the attractive forces are neglected the DEM-CFD simulations predicted lower void fractions as compared to the experimental values obtained in the work of Shapiro and Probst.<sup>58</sup> This shows that there are additional forces between the particles which are increasing the void fraction. These forces can be the frictional forces between the particles, but as shown by the simulation studies in this work (Eq. 4.3), even increasing the coefficients of friction



will not predict the higher void fraction observed in the experiments of Shapiro and Probststein.<sup>58</sup> The other dominant forces between the particles in contact are the surface attractive forces. We consider these forces using the JKR theory.<sup>138</sup> The value of work of adhesion ( $W_a$ ) as  $5 \text{ mJ/m}^2$  is used in the JKR model. This value calculated using the Eq. 4.9.

$$W_a = \frac{A}{24\pi D_0^2} \quad 4.9$$

Here, the minimum separation distance  $D_0$  for silica glass particle is set to  $0.4 \text{ nm}$  and the Hamaker constant ( $A$ ) of  $6 \times 10^{-20} \text{ J}$  (silica glass surfaces in air) is used.<sup>77,186,187</sup> It is found in the literature, that the presence of the aqueous fluid tends to decrease the Hamaker constant and the decrease is sensitive to the method by which the aqueous fluid is added.<sup>77,186</sup> For example, if the fluid is added to the initially dry assembly of the spheres the decrease is significantly lower than the cases in which the solution is vigorously stirred or when the spheres are added individually to the aqueous solution.<sup>77</sup> The measurement of the actual value of the Hamaker constant in aqueous solution is beyond the scope of this study.

The Fig. 4.11 shows that when the attractive forces are considered with a work of adhesion of  $5 \text{ mJ/m}^2$ , the predicted void fraction is higher than the case in which it was neglected. For the smaller mono-dispersed particles with the coefficient of sliding friction set to  $0.6$ , the increase in the void fraction is significant ( $\Delta\epsilon = 0.0562$ ) whereas the bigger mono-dispersed particles show only a marginal increase in the void fraction ( $\Delta\epsilon = 0.002$ ).

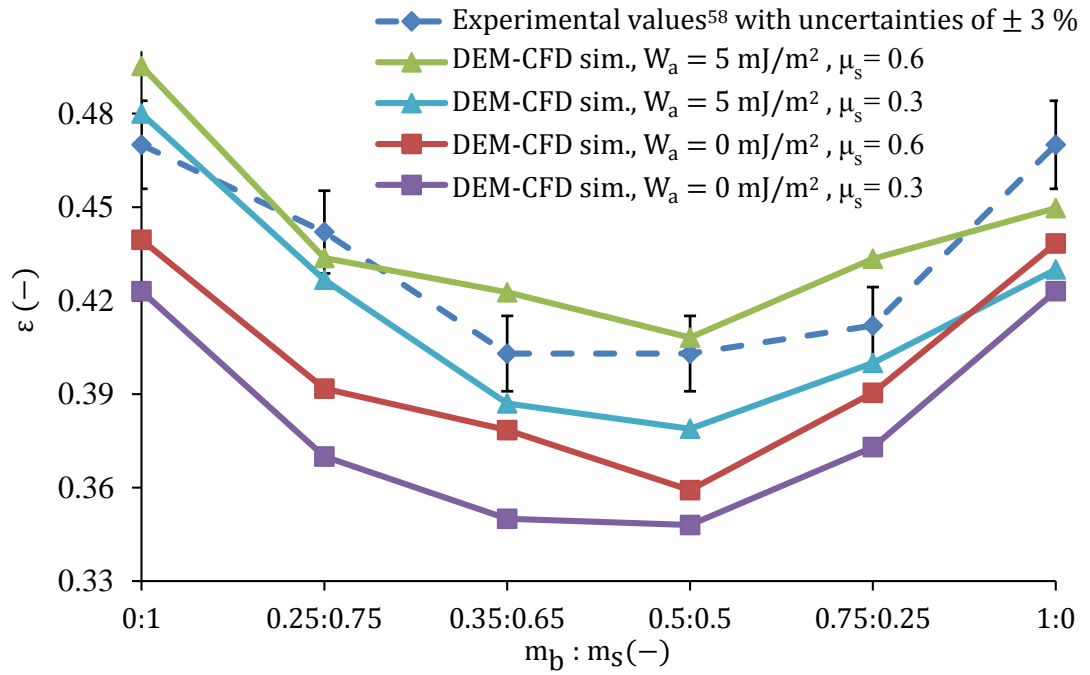


Fig. 4.11 The effect of the mass fraction ratio, the coefficient of sliding friction and the attractive force on the void fraction.

This can be explained as follows, the dynamics of the particle-particle interactions depends on the comparative strengths (ratio) of the attractive JKR force and the gravitational force. For the size ratio (4:1) under consideration, the effect of the attractive force on the smaller particles is higher on the bigger particles by a factor of  $k$ . The factor  $k$  depends on the definition of the comparative strengths (ratio). If it is based on the Bond number,<sup>188</sup> then  $k$  is 16. If the strength is defined based on the cohesion number<sup>139</sup> (Eq. 4.4), then  $k$  is 40. The simulation predicts a void fraction of 0.495 for mon-dispersed glass particles ( $d_p = 40 \mu\text{m}$ ,  $W_a = 5 \text{ mJ/m}^2$ ,  $\mu_s = 0.6$ ) which is in close agreement with the value (0.492) given by the Eq. 4.5. This shows the predictive nature of the Eq. 4.5 and suggests that factor based on the cohesion number is applicable in the scaling of the attractive forces.

The final stage of the sedimented particles with the coefficient of sliding friction set to 0.6 is shown in the Fig. 4.12. A similar trend is observed when the coefficient of sliding friction set to 0.3.

The influence of the attractive forces in the filter cake formed due to bi-dispersed particles is considerably more complex. The experimental study shows that for a mass

fraction ratio in the range of 0.35 : 0.65 to 0.75 : 0.25 the bi-dispersed void fraction remains nearly constant, but the simulations show that there is a decrease in the void fraction when the mass fraction ratio changes from 0.35 : 0.65 to 0.5 : 0.5 and an increase in the void fraction when the mass fraction value is set to 0.75 : 0.25. A possible improvement in the predictions of the simulations can be achieved by using different values of work of adhesion based on a constant cohesion number<sup>139</sup> for the interaction between the big-big, big-small and small-small particle contacts. The challenge here is to incorporate the interdependency between the cohesion number and the coordination number with the inclusion of the size ratio. This needs further investigation which, will be addressed in future studies.

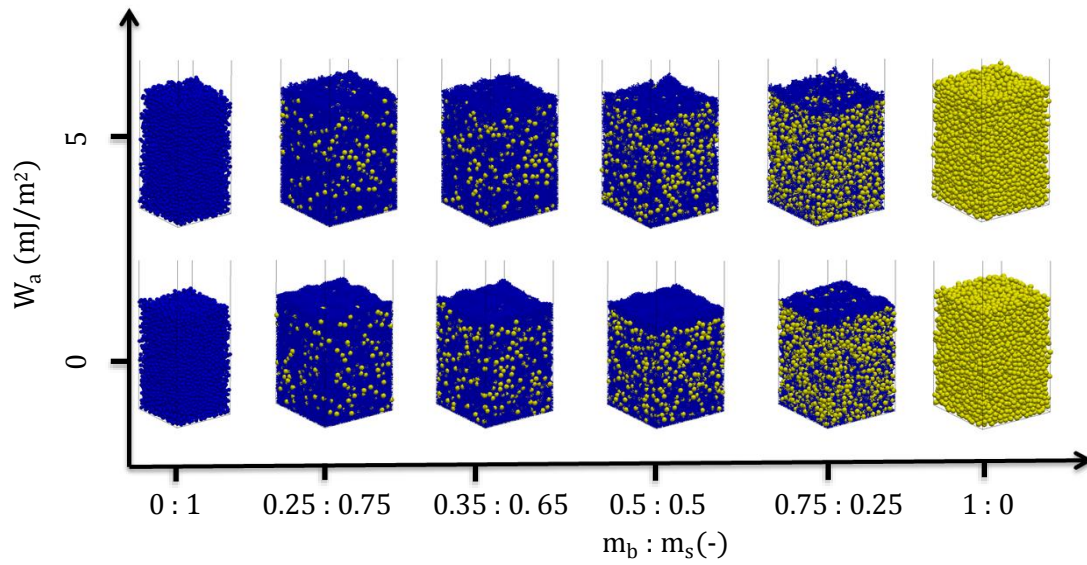


Fig. 4.12 Final state of the sedimented mono and bi-dispersed particles with coefficient of friction set to 0.6.

#### 4.3.4.2 Consolidation due to the fluid forces

For the bi-dispersed particles with the particle size ratio ( $d_{pb} : d_{ps}$ ) of 2 : 1. The effect of different particle mass fraction ratio ( $m_b : m_s$ ) under different flow conditions is investigated. The mass weighted mean particle diameter ( $\langle d \rangle$ ) is kept constant at 250  $\mu\text{m}$  for all the bi-dispersed mixtures. The Reynolds number (Eq. 4.7) is varied by changing the fluid inlet velocity at the top face (consolidation simulations). The values of the coefficient of sliding as 0.6 and rolling friction as 0.002 are used in the simulations. The fluid is glycerin with 5 % water at a temperature of 25°C ( $\rho_f = 1.01 \text{ g/cm}^3$  and  $\eta_f = 1.03 \text{ mPa}\cdot\text{s}$ ) and the attractive forces are neglected. Details of the other parameters used in this study are given in the Table 4.8.

Table 4.8 The particle and the fluid properties used to study the bi-dispersed filter cake

Property	Symbol	Values		
DEM time step (s)	$t_p$	$5 \times 10^{-7}$		
CFD time step (s)	$t_f$	$5 \times 10^{-5}$		
Mass fraction ratio (-)	$m_b : m_s$	0.75 : 0.25	0.5 : 0.5	0.25 : 0.75
Big particle diameter ( $\mu\text{m}$ )	$d_{pb}$	312.5	375	437.5
Small particle diameter ( $\mu\text{m}$ )	$d_{ps}$	156.25	187.5	218.75
Total mass of particle (g)	$m_p$	1.0843	1.5626	2.212

The Fig. 4.13 shows the initial dry void fraction and the corresponding mass fractions used in this study. It is observed that the initial dry void fraction decreases (0.41 to 0.378) with the increase in the mass fraction of bigger particles (0 to 0.5), but with an increase in the mass fraction of bigger particles from 0.5 to 0.75, the void fraction is almost unchanged (0.378 and 0.379).

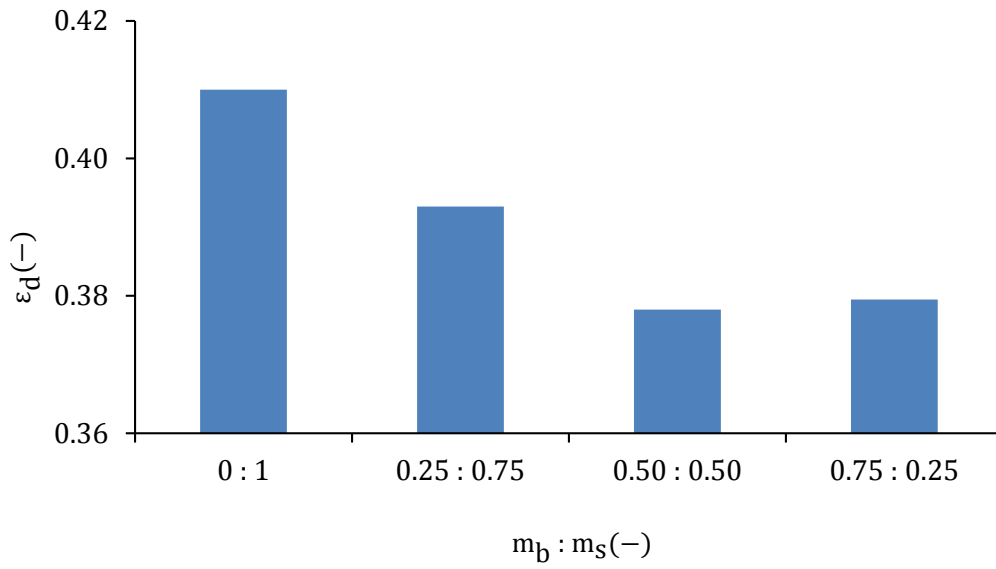


Fig. 4.13 Effect of the particle mass fraction ratio on the void fraction of the dry packed beds/cakes.

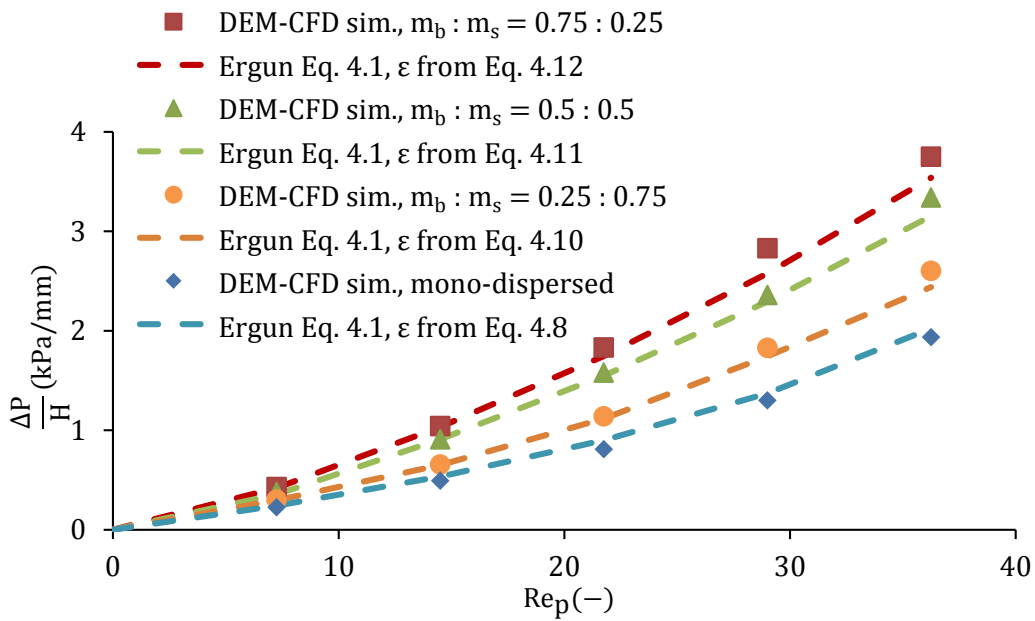


Fig. 4.14 Effect of the particle mass fraction ratio and the Reynolds number on the pressure drop per unit height.

The Fig. 4.14 shows the effect of the particle mass fraction ratio and the Reynolds number on the pressure drop per unit height. For the same Reynolds number, the predicted pressure drop is highly dependent on the particle mass fraction ratio. In general, the pressure drop increases with the increase in the mass fraction of the bigger particles.

Further, the Fig. 4.15 shows that the minimum Reynolds number at which a considerable change in the void fraction (consolidation) is observed, decreases with the increase in the mass fraction of the bigger particles.

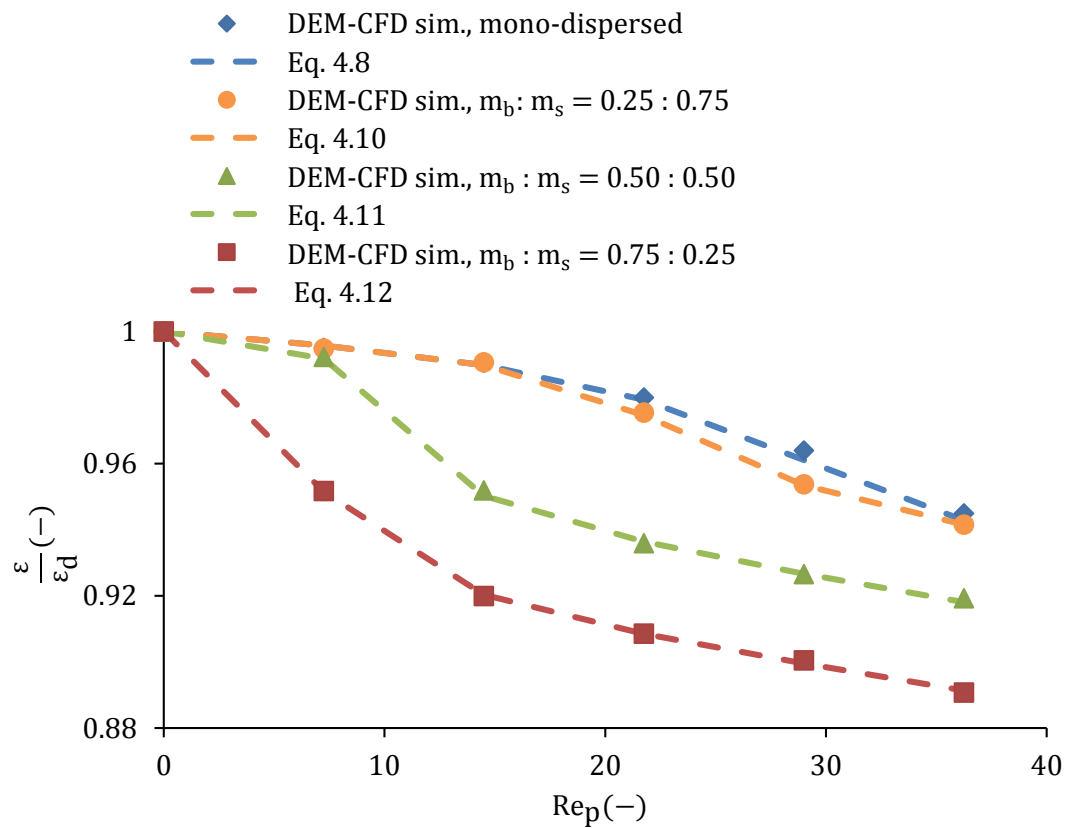


Fig. 4.15 Effect of the particle mass fraction ratio and the Reynolds number on the void fraction of the filter cakes.

The primary reason for this is that in order to maintain the mass weighted mean particle diameter, the particle diameters (big and small) are set to a lower value with the increase in the mass fraction of the bigger particles (Table 4.8). Further, the lower values of the initial void fractions with the increase in the mass fraction of the bigger particles also contribute to the increased pressure drop per unit height which in turn exerts higher fluid force on the packed bed/cake. Thus lowering the minimum Reynolds number beyond which the packed bed/cake undergoes consolidation.

The results from the simulation are used in a regression analysis and the Eqs. 4.10-4.12 represents the relationship between the void fraction and the Reynolds number for bi-dispersed particles with the particle size ratio of 2:1 in the absence of the attractive forces. These equations are useful to predict the consolidation and the corresponding pressure drop as shown in the Fig. 4.14. for particles with coefficient of sliding and rolling friction as 0.6 and 0.002, respectively

$$\frac{\varepsilon}{\varepsilon_d(0.393)} = \frac{0.998 - 0.01048 \cdot \text{Re}_p}{1 - 0.0104 \cdot \text{Re}_p + 0.0000264 \cdot \text{Re}_p^2} \quad \text{Re}_p < 21, m_b : m_s = 0.25 : 0.75 \quad 4.10$$

$$0.947 - 0.000543 \cdot \text{Re}_p + \frac{18.66}{\text{Re}_p^2} \quad 21 \leq \text{Re}_p \leq 36.5, m_b : m_s = 0.25 : 0.75$$

$$\frac{\varepsilon}{\varepsilon_d(0.378)} = \frac{0.954 - 0.00104 \cdot \text{Re}_p + \frac{2.38}{\text{Re}_p^2}}{5 \leq \text{Re}_p \leq 36.5, m_b : m_s = 0.50 : 0.50} \quad 4.11$$

$$\frac{\varepsilon}{\varepsilon_d(0.379)} = \frac{0.927 - 0.00102 \cdot \text{Re}_p + \frac{1.66}{\text{Re}_p^2}}{5 \leq \text{Re}_p \leq 36.5, m_b : m_s = 0.75 : 0.25} \quad 4.12$$

## 4.4 Non-spherical particles

### 4.4.1 Single particle

#### 4.4.1.1 Validation

The mathematical modeling of the volume averaged DEM-CFD coupling for the non-spherical particles is already presented in the Chapter 2. In this section, its implementation is validated by comparing the sedimenting characteristics (the terminal velocity and the orientation) of a single non-spherical particle with the experimental observations. The fluid is assumed to be water at 20°C ( $\rho_f = 1 \text{ g/cm}^3$  and  $\eta_f = 1 \text{ mPa}\cdot\text{s}$ ). Two types of non-spherical particles (A and B) are considered and their details are given in the Table 4.9.

Table 4.9 Particle properties of non-spherical particles

Property	Symbol	Values	
		Particle A	Particle B
Number of sub-elements (-)	Ns	2	2
Sphericity (-)	$\Psi$	0.9954	0.9303
Sub-element diameter ( $\mu\text{m}$ )	$d_{\text{pse}}$	500	250
Distance between the centers ( $\mu\text{m}$ )	$d_c$	56	141
Volume equivalent diameter ( $\mu\text{m}$ )	$d_{\text{pv}}$	532	302
Particle density ( $\text{g/cm}^3$ )	$\rho_p$	2.5	2.5

The Table 4.10 shows the comparison of terminal velocities of the non-spherical particles A and B with the corresponding values given by Eq. 2.28.<sup>122</sup> The terminal velocities predicted by the DEM-CFD simulations are in close agreement with the semi-empirical correlations.



Table 4.10 Terminal velocity of non-spherical particles

Terminal velocity ( cm/s )	Symbol	Particle	
		A	B
Semi-empirical (Eq. 2.28 )	$u_t$	9.02	4.14
DEM-CFD simulations	$u_t$	8.93	4.10

Further, it is observed that the non-spherical particle A shows initial oscillations in the projection of the particle diameters (Fig. 4.16). This is because, in the initial stage, the particle A has nearly the same projected diameter (due to high sphericity) on all the planes ( $d_{prj}^{yz} \approx d_{prj}^{xz} \approx d_{prj}^{xy}$ ) and the fluid forces acting in each direction compete to have the least possible resistance to the motion of the particle. The oscillations stabilize when the projected diameter is minimum on the plane (xy) normal to the gravitational axis.

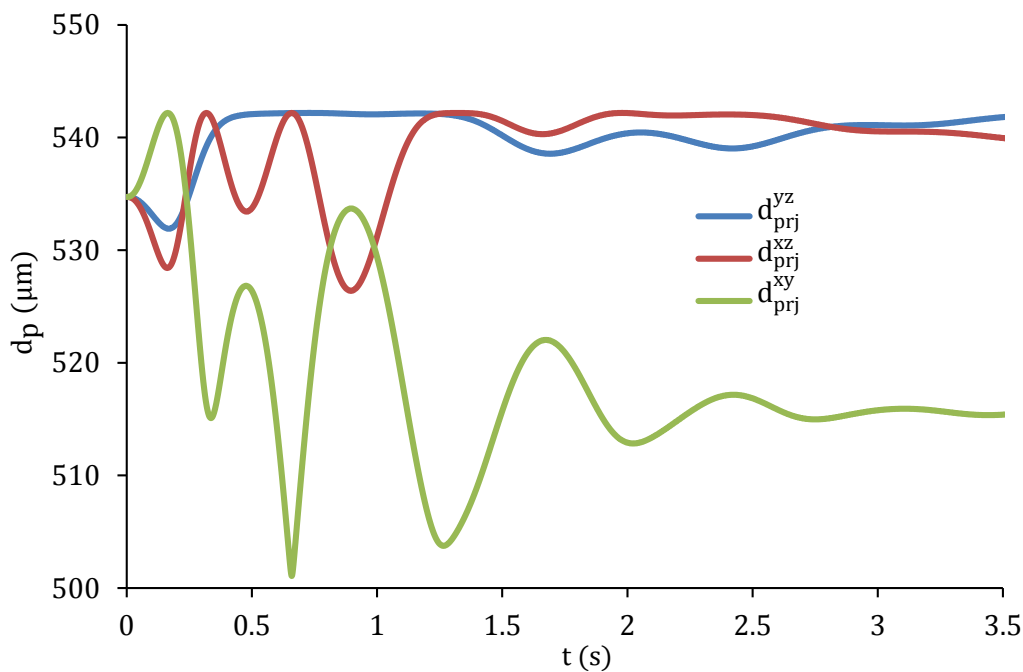


Fig. 4.16 Variation in the projected diameter of the particle A over time.

In the case of the particle B, no oscillations are observed (Fig. 4.17). This is because the particle B at the initial stage has a higher projected diameter ( $d_{prj}^{xy}$ ) on the plane normal to the gravitational axis which is gradually reduced to the least possible value. The other two projected diameters are nearly equal ( $d_{prj}^{yz} = d_{prj}^{xz}$ ) and reach the maximum possible value.

Such presence or absence of the initial oscillations, changes in orientations, and stabilization with a minimum projected diameter were experimentally observed by McNown and Malaika<sup>189</sup> for non-spherical particles sedimenting with a Reynolds number greater than 0.1. The Reynolds number of the particles, A and B based on the terminal velocities (simulation) are 47.5 and 12.3, respectively.

Thus, the present implementation of the non-spherical DEM-CFD not only predicts the velocity of the particle in a fluid but also the orientation of the particle. These are crucial factors in determining the structure of the packed beds/cakes.

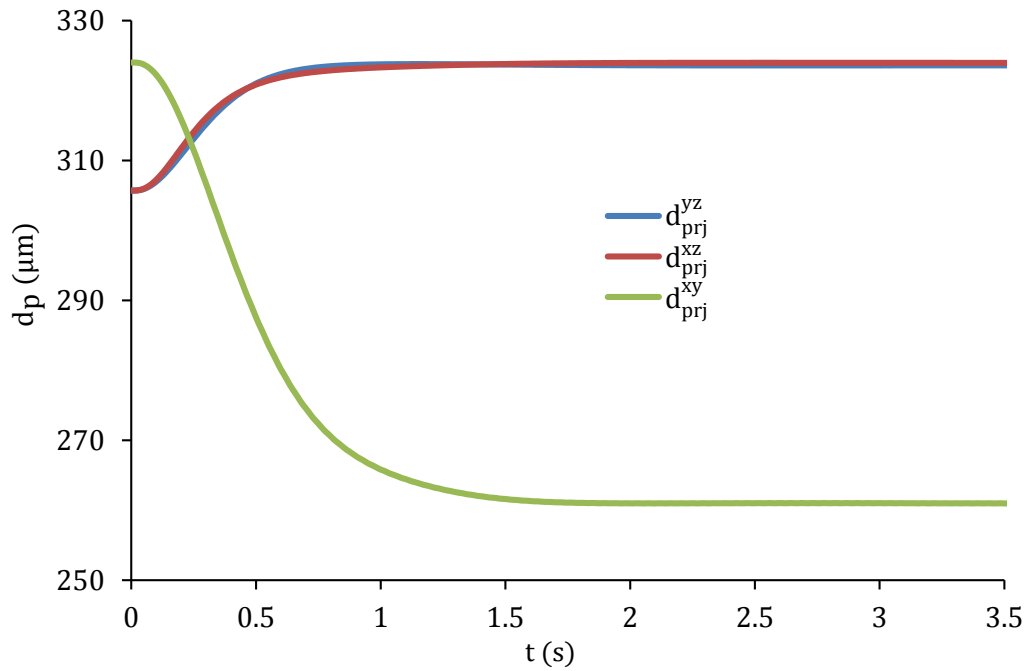


Fig. 4.17 Variation in the projected diameter of the particle B over time.

### 4.4.2 Sedimentation of the non-spherical suspensions

#### 4.4.2.1 Validation

The discussions in this section are based on the simulations of suspensions with non-spherical particles sedimenting in water at 20°C ( $\rho_f = 1 \text{ g/cm}^3$  and  $\eta_f = 1 \text{ mPa}\cdot\text{s}$ ). All the particles have the same volume equivalent diameter of (302  $\mu\text{m}$ ). The other particle properties are listed in the Table 4.11. and the Table 4.12. The Fig. 4.18 shows the graphical representations and the initial orientations of the particles (C, D, and E).

Table 4.11 Properties of non-spherical particles

Property	Symbol	Values
Coefficient of restitution (-)	$e_n$	0.1
Coefficient of rolling friction (-)	$\mu_r$	0.002
Coefficient of sliding friction (-)	$\mu_s$	(0.1, 0.3, 0.6)
CFD time step (s)	$t_f$	$5 \times 10^{-5}$
Total mass of the particles (g)	$M_s$	1.5858
Particle density ( $\text{g/cm}^3$ )	$\rho_p$	2.5
DEM time step (s)	$t_p$	$5 \times 10^{-7}$
Poisons ratio (-)	$\nu$	0.3
Volume equivalent diameter ( $\mu\text{m}$ )	$d_{pv}$	302
Young's modulus (Gpa)	$E$	0.1

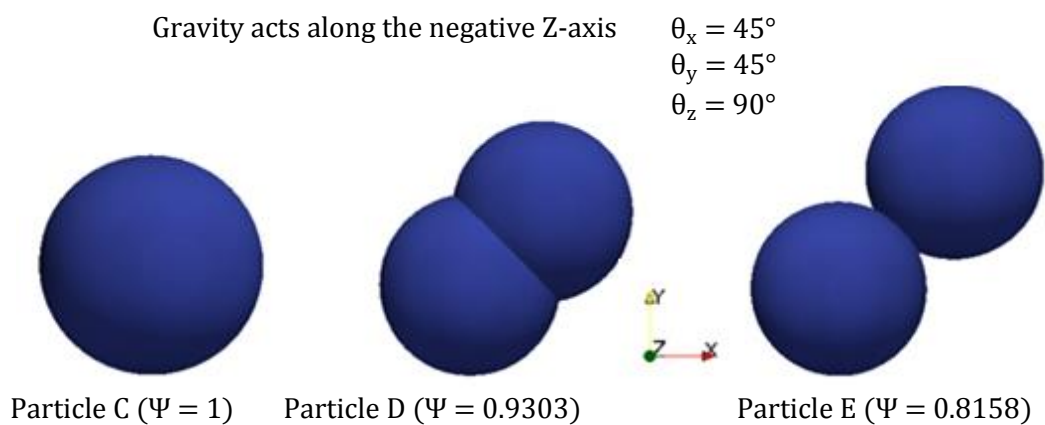


Fig. 4.18 Graphical representation of the spherical (C) and non-spherical (D, E) particles.

Table 4.12 Non-spherical parameters varied in the study

Property	Symbol	Particle		
		C	D	E
Diameter of sub-elements ( $\mu\text{m}$ )	$d_{ps}$	302	250	240
Number of sub-elements (-)	$N_s$	2	2	2
Distance between the centers ( $\mu\text{m}$ )	$d_c$	0	141	226
Sphericity (-)	$\Psi$	1	0.9303	0.8158
Void fraction power function (-)	$2 + (\gamma - 2)n$	- 2.57	- 2.2463	- 0.5930

The terminal velocity of the suspension ( $u_s^{\text{emp}}$ ) can be predicted using the Eq. 4.13.<sup>190</sup>

$$u_s^{\text{emp}} = u_t \varepsilon_{\text{ints}}^{n-2} \quad 4.13$$

Here,  $u_t$  is the terminal velocity of a single non-spherical particle calculated using Eq. 2.28.  $\varepsilon_{\text{ints}}$  is the void fraction of the suspension and  $n$  is calculated using the Eq. 2.30.<sup>97</sup> In the simulations, the velocity of the suspension is calculated using Eq. 4.14.

$$u_s^{\text{sim}} = \frac{x_h}{t_h} \quad 4.14$$

Here,  $x_h$  is the distance travelled by the topmost particle in the suspension and  $t_h$  is the time required by particle to travel this distance. The Table 4.13, shows the comparison of the terminal velocity of the suspension predicted by the DEM-CFD simulations which is in agreement with the Eq. 4.13. The decrease in the terminal velocity, of the suspension with the increase in the sphericity of the particles is predicted by the DEM-CFD simulations which is in agreement with the experimental observations.<sup>190</sup> Thus the implemented, volume averaged DEM-CFD coupling for the non-spherical particles

(suspensions) is validated. Further, the study highlights, the loss of information (velocity and orientation) when the non-spherical particles are modelled as spheres having the same volume equivalent diameter.

Table 4.13 Terminal velocity of suspensions

Property	Symbol	Particle		
		C	D	E
Sphericity	$\Psi$	1	0.9303	0.8158
Empirical terminal velocity (cm/s)	$u_s^{\text{emp}}$	2.2932	2.1147	1.883
DEM-CFD terminal velocity (cm/s)	$u_s^{\text{sim}}$	2.3118	2.1316	1.9274

#### 4.4.3 Effect of the sphericity and friction

In this section, the effect of the sphericity on the void fraction of the packed beds/cakes is discussed. The particles (C, D and E, Table 4.13) and flow conditions (sedimentation) are the same as in the previous section.

The Fig. 4.19 shows the effect of the sphericity on the void fraction of the packed beds/cakes. The simulation results suggest that the void fraction of the packed bed/cake increases with the decrease in the sphericity. The dashed lines in the Fig. 4.19 represent the experimentally observed trends of the void fraction of the packed beds/cakes corresponding to the dense, the normal and the loose packing.<sup>59</sup> Loose packing is expected for a packed bed/cake formed due to sedimentation.<sup>57,58</sup> The trend of the void fraction predicted by the DEM-CFD simulation is in agreement with the experimental observations. The Fig. 4.20 shows the final stage of the packed beds/cakes where the coefficient of friction is set to 0.6.

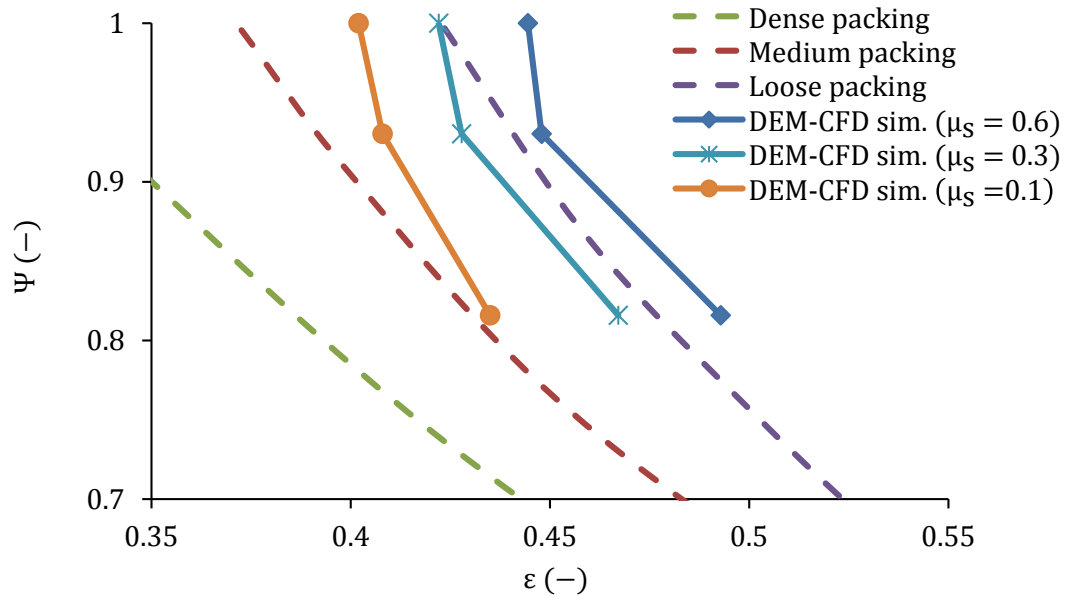


Fig. 4.19 Effect of the sphericity and the coefficient of sliding friction on the void fraction.

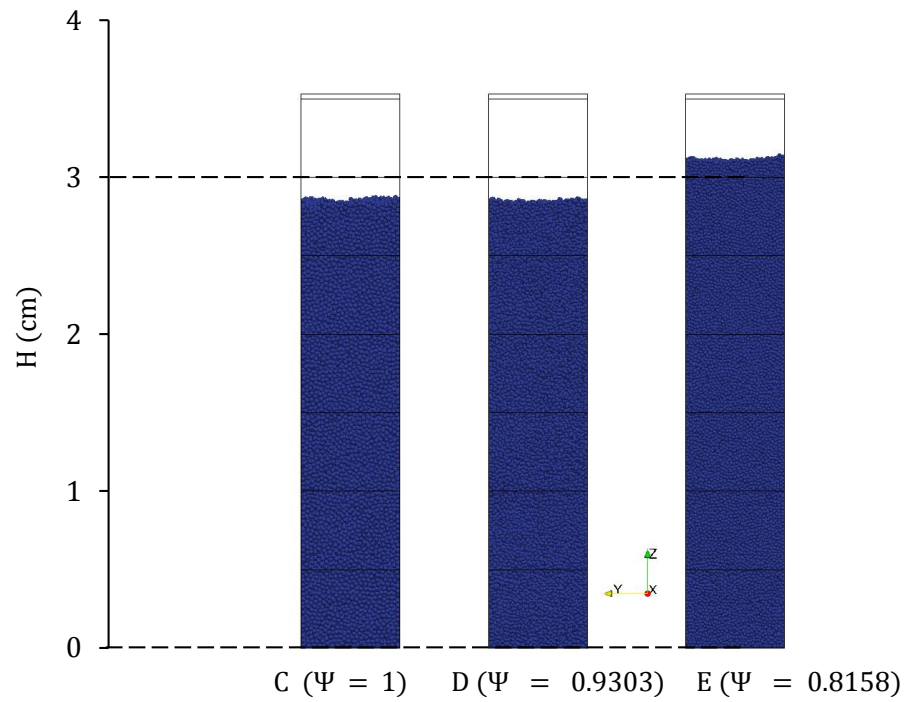


Fig. 4.20 Final stage of the packed beds/cakes with the coefficient of sliding friction as 0.6.

Further, the simulations also show that void fraction of the packed bed/cake is influenced by the coefficient of sliding friction. A denser packing is obtained with the decrease in the coefficient of sliding friction. The influences and reasons are similar to

the spherical particles which are already discussed in the sec. 4.3.3.1. The attractive forces between the particles can also affect the void fraction, but are not considered in this study.

#### 4.4.4 Effect of the initial orientation

The orientation of a particle is defined by the angles ( $\theta_x, \theta_y, \theta_z$ ) between the major axis of the particle and the three principle axis. The non-spherical particles (D and E) are used to study the effect of the initial orientation of the particle on the void fraction of the packed bed/cake. All the particles in a suspension have the same orientation. The different orientations and the corresponding void fractions of the packed beds/cakes are shown in the Fig. 4.21 and Fig. 4.22.

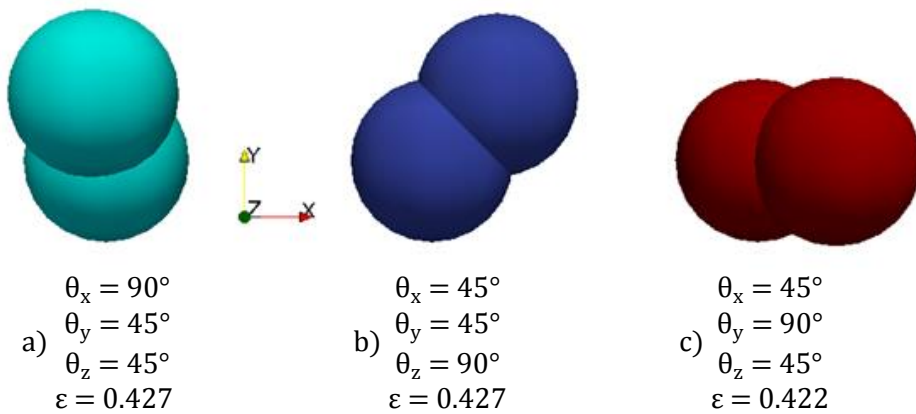


Fig. 4.21 Different initial orientations and the corresponding void fraction of the particle D

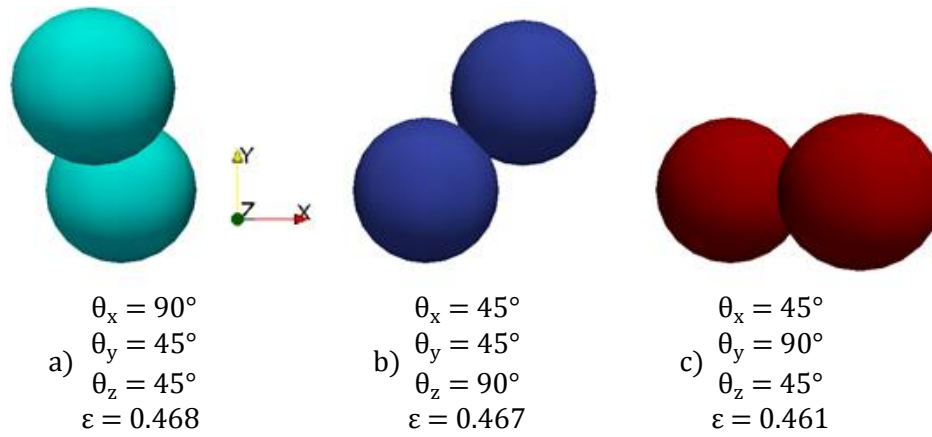


Fig. 4.22 Different initial orientations and the corresponding void fraction of the particle E.

It is observed that for the range of the sphericity between 0.8158 to 1 the initial orientations of the particles have no significant effect on the void fraction of the formed packed beds/cakes. This is due to the change in orientation of the sedimenting particles. Irrespective of the initial orientation the sedimenting particles orient themselves in such a way that they experience the least possible fluid resistance.

#### 4.4.5 Consolidation due to the fluid forces

Under the same fluid conditions and the same volume equivalent diameter, the pressure drop across a packed bed/cake depends on the void fraction and the sphericity. The Eq. 4.15 suggests that the pressure drop increases with a decrease in the sphericity but the void fraction and the sphericity are inter-dependent (Fig. 4.19).

$$\frac{\Delta P}{H} = 150 \frac{\eta_f (1 - \varepsilon)^2 U_f}{\varepsilon^3 (\psi d_{pv})^2} + 1.75 \frac{(1 - \varepsilon) \rho_f U_f^2}{\varepsilon^3 \psi d_{pv}} \quad 4.15$$

To understand these complex inter-dependencies, DEM-CFD simulations are carried out. Here, the particles C, D and E are used (Table 4.11 and Table 4.12). The coefficient



of sliding friction is set to 0.6. The void fractions of the packed beds/cakes, obtained under dry conditions (no fluid forces) are given in the Table 4.14.

Table 4.14 Variation of pressure drop and void fraction with respect to the sphericity

Particle	Sphericity (-)	Dry void fraction (-)	Pressure drop per unit height (kPa/m)	
			DEM-CFD	Eq. 4.15
-	$\Psi$	$\epsilon_d$	$\Delta P/H$	$\Delta P/H$
C	1	0.41	42.96	42.77
D	0.9303	0.408	50.43	50.38
E	0.8158	0.462	37.28	37.23

All the dry packed beds/cakes are subjected to a fluid flow with an inlet velocity of 0.5 cm/s ( $Re_p=0.054$ ). The Table 4.14 shows that the pressure drops per unit height predicted by the DEM-CFD simulations are in agreement with the Ergun equation (Eq. 4.15). Further, the pressure drop per unit height predicted by the DEM-CFD simulations, across a packed bed/cake formed due to the non-spherical particles D ( $\psi = 0.9303$ ) is the highest. The higher pressure drop is due to the reduced sphericity alone as the corresponding void fractions of the packed beds/cakes formed due to particles C and D are nearly equal. In contrast to this, the pressure drop per unit length across a filter cake formed due to the particles E ( $\psi = 0.8158$ ) is the least one. The reason is the increase in the void fraction which dominates the effect of the reduced sphericity.

The study is extended to a wide range of particle Reynolds number (0 to 75). The Fig. 4.23 shows the variation of the void fraction and the pressure drop per unit height of the packed beds/cakes with respect to the particle Reynolds number.

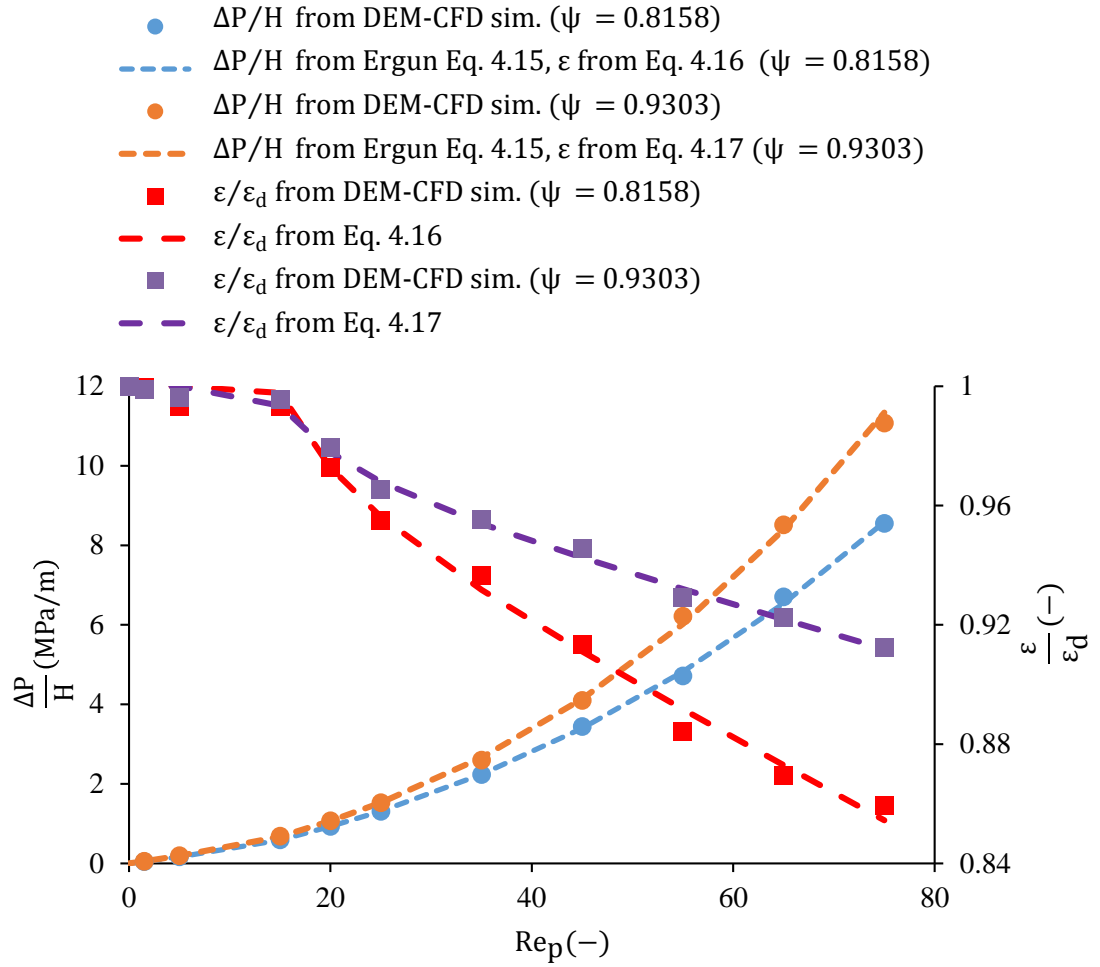


Fig. 4.23 Effect of the sphericity on the pressure drop and the effect of the flow conditions on the consolidation.

The consolidation of the packed bed/cake is observed when the Reynolds number is greater than 5. For the same Reynolds number, the packed bed/cake with the particles D ( $\psi = 0.9303$ ) has a higher consolidation than the packed bed/cake with the particles E ( $\psi = 0.8158$ ). This is because of the interdependency between the void fraction, sphericity and the pressure drop. These interdependencies are captured by the Eq. 4.16 and 4.17 and are useful for the prediction of the pressure drop (Fig. 4.23). Further it should be noted that the theses equations are valid for the particles with a coefficient of sliding friction of 0.6.

$$\frac{\varepsilon}{\varepsilon_d(0.462)} = 0.983 - 0.000961 \cdot \text{Re}_p + \frac{5.599}{\text{Re}_p^2}, 5 \leq \text{Re}_p < 75, \psi = 0.8158 \quad 4.16$$

$$\frac{\varepsilon}{\varepsilon_d(0.408)} = 0.988 - 0.0018 \cdot \text{Re}_p + \frac{8.272}{\text{Re}_p^2}, 5 \leq \text{Re}_p < 75, \psi = 0.9303 \quad 4.17$$

Here,  $\varepsilon$  and  $\varepsilon_d$  are the void fraction of the filter cake after and before compression. Further, it should be noted that theses equations are valid for the particles with a coefficient of sliding friction of 0.6.

---

## 5 Summary and Conclusions

---

### 5.1 Summary

This study was dedicated to the investigation of the filter cake formation process using DEM-CFD simulation with experimentally calibrated parameters. The scope of this thesis was limited to the study of the effect of the size, the size distribution, the shape, and the particle-particle interaction parameter on the packed beds/cakes.

In the literature, most of the experimental studies related to packed bed/cake reported only the macroscopic properties (void fraction, pressure drop, mass flow rate). The literature lacked the information about the microscopic particle-particle interaction parameters. Therefore, in this study the particle-particle interaction properties, namely the coefficient of restitution and sliding friction were experimentally measured. A correlation was developed between the measured coefficient of restitution and the Stokes number. This correlation is valid to micron sized particle in the range of 200 to 1000  $\mu\text{m}$ . Measurement of these properties was one of the goals of this study which was successfully achieved. Further, the measured coefficient of restitution and sliding friction (in dry and wet conditions) served as input parameters in the numerical studies. The numerical studies in the literature were either based on the Eulerian-Eulerian or the Eulerian-Lagrangian approach. The Eulerian-Eulerian approach was not suitable for predicting the particle level characteristics like the consolidation of the packed beds/cakes. Studies in the literature showed that the *two-way volume averaged coupling approach between the DEM and CFD* was a promising approach to study the various aspects of the packed beds/cakes. The DEM-CFD studies in the literature were limited to spherical mono-dispersed particle. In this thesis, the numerical analysis was extended to the bi-dispersed and the non-spherical particles. In order to achieve this,

advanced drag models were implemented in the LIGGGHTS-OpenFOAM framework. The necessary validations were carried out and were presented in this thesis. This was the other successfully achieved goal of the thesis.

## 5.2 Conclusions

The key conclusions based on the numerical studies carried out in this thesis are:

1. The fluid cell size to the particle diameter ratio ( $h/d_p$ ) of 3 is a reasonable choice for the volume averaged DEM-CFD coupling (sec. 4.3.1).
2. Calculating the coefficient of restitution based on the lubrication theory or providing a constant equivalent coefficient of restitution has no significant effect on the void fraction of the packed bed/cake. Using a constant equivalent coefficient of restitution is a cheaper alternative in terms of the computational effort (secs. 4.3.2 and 4.3.3.3)
3. Setting the coefficient of sliding and rolling friction to 0.6 and 0.002, respectively, gives a void fraction of  $0.43 \pm_{0.001}^{0.001}$ . This is in close agreement with the experimental observation of Onoda and Liniger<sup>57</sup> (sec. 4.3.3.4)
4. For the spherical particles, if the coefficient of sliding is less than 0.6, then the rolling friction has a negligible effect on the void fraction of the packed bed/cake (sec. 4.3.3.4).
5. Most of the spherical particles in a packed bed/cake have a coordination number in the range of 3 to 7 (sec. 4.3.3.5).
6. The cohesion number influence the distribution of the coordination number. In general, the mean coordination number decreases with an increase in the cohesion number. Based on the simulations a correlation is developed between the cohesion number and the void fraction of the packed bed/cake formed due to monodispersed particles. This correlation is valid for particles with a coefficient of friction in the range of 0.3 to 0.6 (sec. 4.3.3.5 and Eq. 4.5).
7. The influences of the cohesion number (attractive forces) on the packed beds/cakes, formed due to bi-dispersed particles are complex. The simulations fail to predict the variation of the void fractions with respect to the mass fraction ratios when the attractive forces are of importance. A possible improvement in the predictions of the simulations can be achieved by using different values of work of

adhesion based on a constant cohesion number<sup>139</sup> for the interaction between the big-big, big-small and small-small particle contacts. The challenge here is to incorporate the interdependency between the cohesion number and the inclusion of the size ratio in the definition of coordination number. This needs further investigation, which will be addressed in future studies (sec. 4.3.4.1).

8. The volume averaged DEM-CFD approach can successfully predict the consolidation of the packed bed/cake. For a packed bed/cake formed due to the mono-dispersed particles ( $\rho_p = 2.5 \text{ g/cm}^3$  and  $d_p = 250 \text{ }\mu\text{m}$ ,  $\mu_s = 0.6$ ), the consolidation is significant for a Reynolds number greater than 29. Here, it should be noted that Reynolds number of 29 is not a universal criteria and is sensitive to the particle-particle interaction parameters like the coefficient of friction. Simulations have shown that the Reynolds number beyond which significant consolidation occurs decreases with the decrease in the coefficient of sliding friction (sec. 4.3.3.6).
9. In the case of bi-dispersed particles, for the same Reynolds number, the predicted pressure drop is highly dependent on the particle mass fraction ratio. In general, the pressure drop increases with the increase in the mass fraction of the bigger particles. The primary reason for this was that in order to maintain the mass weighted mean particle diameter, the particle diameters (big and small) was set to a lower value with the increase in the mass fraction of the bigger particles. Further, the lower values of the initial void fractions with the increase in the mass fraction of the bigger particles also contribute to the increased the pressure drop per unit height which in turn exerted higher fluid force on the packed bed/cake. Thus lowering the minimum Reynolds number beyond which the packed bed/cake undergoes consolidation. This study also highlights the importance of considering the bi-dispersed nature of the suspension even in the cases where the mass weighted mean particle diameter has the same value (sec. 4.3.4.2).
10. The present implementation of the non-spherical DEM-CFD not only predicts the velocity of the particle in a fluid but also the orientation of the particle. These are crucial factors in determining the rate of sedimentation and the final structure of the packed beds/cakes (secs. 4.4.1 and 4.4.2).

11. The simulation studies suggest that the void fraction of the packed bed/cake increases with the decrease in the sphericity. This is in agreement with the experimental observation in the literature (sec. 4.4.3)
12. For the range of the sphericity between 0.8158 to 1 the initial orientations of the particles have no significant effect on the void fraction of the formed packed bed/cake. This is due to the change in orientation of the sedimenting particles. Irrespective of the initial orientation the sedimenting particles orient themselves in such a way that they experience the least possible fluid resistance (sec. 4.4.4).
13. The complex inter-dependency between the void fraction, the mass fraction, the sphericity and the pressure drop are studied. Correlations are developed between the void fraction and the Reynolds number. These correlations can predict the consolidation and the corresponding pressure drop (sec. 4.4.5).

### 5.3 Recommendations for future work

This thesis dealt with certain details of the packed beds/cakes formation process. Future studies can focus on the other aspects of the packed bed/cake. A few of them are:

1. For the extensive validation of the present numerical implementation. Additional experiments can be performed in order to obtain the micro (work of adhesion) and macroscopic properties (void fraction, pressure drop, and mass flow rate) of the packed beds/cakes. The challenge here is to maintain the operating conditions which could be easily employed in the numerical studies
2. Extending the numerical analysis for a particle size ratio greater than 4. For this, the particle-fluid drag correlations are to be first developed. Then the volume averaged DEM-CFD approach could be used.
3. A generalized numerical framework can be developed where complex shaped non-spherical particles could be simulated. Here, the challenge is to find an efficient algorithm which could calculate the projected areas of a large number of parti

---

## Annexure

---

### A.1 Coefficient of sliding friction based on the measured shear forces

Table A.1 Measured particle-plate dry contact coefficient of the sliding friction.

Case	Particle diameter ( $\mu\text{m}$ )	Weight (N)	Coefficient of friction (-)	Average coefficient of friction (-)
-	( $d_p$ )	$W$	$\langle \mu_s \rangle^{d_p} = \frac{\sum_{i=1}^3 F_s^i}{3W}$	$\mu_s = \frac{\sum_{d_p=250}^{1000} \langle \mu_s \rangle^{d_p}}{9}$
Particle-plate dry contact	1000	17.78	0.3025	0.252
		22.95	0.265	
		26.08	0.239	
	500	17.78	0.247	
		22.95	0.250	
		26.08	0.238	
	250	17.78	0.244	
		22.95	0.247	
		26.08	0.236	



Table A.2 Measured particle-plate wet contact coefficient of the sliding friction.

Case	Particle diameter ( $\mu\text{m}$ )	Weight (N)	Coefficient of friction (-)	Average coefficient of friction (-)
-	( $d_p$ )	$W$	$\langle\mu_s\rangle^{d_p} = \frac{\sum_{i=1}^3 F_s^i}{3W}$	$\mu_s = \frac{\sum_{d_p=250}^{1000} \langle\mu_s\rangle^{d_p}}{9}$
Particle-plate wet contact	1000	17.78	0.237	0.222
		22.95	0.201	
		26.08	0.207	
	500	17.78	0.223	
		22.95	0.221	
		26.08	0.213	
	250	17.78	0.253	
		22.95	0.230	
		26.08	0.217	

Table A.3 Measured particle-particle dry contact coefficient of the sliding friction.

Case	Particle diameter ( $\mu\text{m}$ )	Weight (N)	Coefficient of friction (-)	Average coefficient of friction (-)
-	( $d_p$ )	$W$	$\langle\mu_s\rangle^{d_p} = \frac{\sum_{i=1}^3 F_s^i}{3W}$	$\mu_s = \frac{\sum_{d_p=250}^{1000} \langle\mu_s\rangle^{d_p}}{9}$
Particle-particle dry contact	1000	17.78	0.300	0.301
		22.95	0.318	
		26.08	0.292	
	500	17.78	0.295	
		22.95	0.315	
		26.08	0.291	
	250	17.78	0.280	
		22.95	0.320	
		26.08	0.301	

Table A.4 Measured particle-particle wet contact coefficient of the sliding friction.

Case	Particle diameter ( $\mu\text{m}$ )	Weight (N)	Coefficient of friction (-)	Average coefficient of friction (-)
-	( $d_p$ )	$W$	$\langle\mu_s\rangle^{d_p} = \frac{\sum_{i=1}^3 F_s^i}{3W}$	$\mu_s = \frac{\sum_{d_p=250}^{1000} \langle\mu_s\rangle^{d_p}}{9}$
Particle-particle dry contact	1000	17.78	0.276	0.285
		22.95	0.305	
		26.08	0.292	
	500	17.78	0.272	
		22.95	0.282	
		26.08	0.289	
	250	17.78	0.255	
		22.95	0.305	
		26.08	0.292	



---

## Bibliography

---

1. Tien C. *Granular Filtration of Aerosols and Hydrosols: Butterworths Series in Chemical Engineering*. Butterworth-Heinemann; 2013.
2. Wakeman RJ, Tarleton ES. *Filtration: Equipment Selection, Modelling and Process Simulation*. Elsevier; 1999.
3. Hutten IM. *Handbook of Nonwoven Filter Media*. Elsevier; 2007.
4. Sacramento RN, Yang Y, You Z, et al. Deep bed and cake filtration of two-size particle suspension in porous media. *J Pet Sci Eng*. 2015;126:201-210.
5. Matteson. *Filtration: Principles and Practices, Second Edition, Revised and Expanded*. CRC Press; 1986.
6. Chen Y-S, Hsiau S-S. Cake formation and growth in cake filtration. *Powder Technol*. 2009;192(2):217–224.
7. Masuda H, Higashitani K, Yoshida H. *Powder Technology Handbook, Third Edition*. CRC Press; 2006.
8. Wakao N, Kagei S. *Heat and Mass Transfer in Packed Beds*. Taylor & Francis; 1982.
9. Cheremisinoff NP. *Liquid Filtration*. Butterworth-Heinemann; 1998.
10. Rushton A, Ward AS, Holdich RG. *Solid-Liquid Filtration and Separation Technology*. John Wiley & Sons; 2008.
11. Norouzi HR, Zarghami R, Sotudeh-Gharebagh R, Mostoufi N. *Coupled CFD-DEM Modeling: Formulation, Implementation and Application to Multiphase Flows*. John Wiley & Sons; 2016.
12. Jackson R. *The Dynamics of Fluidized Particles*. Cambridge University Press; 2000.

13. Kolev N. *Packed Bed Columns: For Absorption, Desorption, Rectification and Direct Heat Transfer*. Elsevier; 2006.
14. Kruggel-Emden H, Simsek E, Rickelt S, Wirtz S, Scherer V. Review and extension of normal force models for the discrete element method. *Powder Technol.* 2007;171(3):157–173.
15. Chuhan Z, Pekau OA, Feng J, Guanglun W. Application of distinct element method in dynamic analysis of high rock slopes and blocky structures. *Soil Dyn Earthq Eng.* 1997;16(6):385–394.
16. Jing L, Stephansson O. *Fundamentals of Discrete Element Methods for Rock Engineering: Theory and Applications*. Elsevier; 2007.
17. Campbell CS, Brennen CE. Computer simulation of granular shear flows. *J Fluid Mech.* 1985;151:167–188.
18. Cundall PA, Strack OD. A discrete numerical model for granular assemblies. *geotechnique.* 1979;29(1):47–65.
19. Seville JPK, Wu C-Y. *Particle Technology and Engineering: An Engineer's Guide to Particles and Powders: Fundamentals and Computational Approaches*. Butterworth-Heinemann; 2016.
20. Munjiza A, Latham JP, John NWM. 3D dynamics of discrete element systems comprising irregular discrete elements—integration solution for finite rotations in 3D. *Int J Numer Methods Eng.* 2003;56(1):35–55.
21. Höhner D, Wirtz S, Scherer V. A study on the influence of particle shape on the mechanical interactions of granular media in a hopper using the Discrete Element Method. *Powder Technol.* 2015;278:286–305.
22. Höhner D, Wirtz S, Scherer V. A numerical study on the influence of particle shape on hopper discharge within the polyhedral and multi-sphere discrete element method. *Powder Technol.* 2012;226:16–28.
23. Vu-Quoc L, Zhang X, Walton OR. A 3-D discrete-element method for dry granular flows of ellipsoidal particles. *Comput Methods Appl Mech Eng.* 2000;187(3):483–528.
24. Kodam M, Bharadwaj R, Curtis J, Hancock B, Wassgren C. Cylindrical object contact detection for use in discrete element method simulations, Part II—Experimental validation. *Chem Eng Sci.* 2010;65(22):5863–5871.

25. Abbaspour-Fard MH. Discrete element modelling of the dynamic behaviour of non-spherical particulate materials. 2000.
26. Versteeg HK, Malalasekera W. *An Introduction to Computational Fluid Dynamics: The Finite Volume Method*. Pearson Education; 2007.
27. Wendt J. *Computational Fluid Dynamics: An Introduction*. Springer Science & Business Media; 2008.
28. LeVeque RJ. *Finite Difference Methods for Ordinary and Partial Differential Equations: Steady-State and Time-Dependent Problems*. SIAM; 2007.
29. Moukalled F, Mangani L, Darwish M. *The Finite Volume Method in Computational Fluid Dynamics: An Advanced Introduction with OpenFOAM® and Matlab*. Springer; 2015.
30. Larson MG, Bengzon F. *The Finite Element Method: Theory, Implementation, and Applications*. Springer Science & Business Media; 2013.
31. Weller H, Greenshields C, de Rouvray C. *OpenFOAM*. The OpenFOAM Foundation; 2018. <https://openfoam.org/release/2-2-0/>.
32. Fluent INC. FLUENT 6.3 user's guide. *Fluent Doc*. 2006.
33. Multiphysics C. Comsol multiphysics user guide (version 4.3 a). *COMSOL AB*. 2012:39–40.
34. Dedner A, Flemisch B, Klöfkor R. *Advances in DUNE*. Springer; 2012.
35. Crowe CT, Schwarzkopf JD, Sommerfeld M, Tsuji Y. *Multiphase Flows with Droplets and Particles, Second Edition*. CRC Press; 2011.
36. Ranade VV. *Computational Flow Modeling for Chemical Reactor Engineering*. Academic Press; 2002.
37. Zhao T. *Coupled DEM-CFD Analyses of Landslide-Induced Debris Flows*. Springer; 2017.
38. Fries L, Antonyuk S, Heinrich S, Dopfer D, Palzer S. Collision dynamics in fluidised bed granulators: A DEM-CFD study. *Chem Eng Sci*. 2013;86:108–123.
39. Di Renzo A, Di Maio FP. Homogeneous and bubbling fluidization regimes in DEM–CFD simulations: hydrodynamic stability of gas and liquid fluidized beds. *Chem Eng Sci*. 2007;62(1-2):116–130.

40. Zhao J, Shan T. Coupled CFD–DEM simulation of fluid–particle interaction in geomechanics. *Powder Technol.* 2013;239:248–258.
41. Hager A, Kanitz M, Grabe J, Kloss C, Goniva C. *Unresolved CFD-DEM in Environmental Engineering: Submarine Slope Stability and Other Applications*. SINTEF Academic Press; 2017.
42. Goniva C, Kloss C. *LIGGGHTS®project*. DCS computing; 2018.  
<https://www.cfdem.com/liggghtsr-open-source-discrete-element-method-particle-simulation-code>.
43. Goniva C, Kloss C. *CFDEM®project*. DCS computing; 2018.  
<https://www.cfdem.com/cfdemrcoupling-open-source-cfd-dem-framework>.
44. Gidaspow D. *Multiphase Flow and Fluidization: Continuum and Kinetic Theory Descriptions*. Academic press; 1994.
45. Sobieski W. Switch Function and Sphericity Coefficient in the Gidaspow Drag Model for Modeling Solid-Fluid Systems. *Dry Technol.* 2009;27(2):267–280.
46. Wen C, Yu Y. Mechanics of fluidization. In: *Chemical Engineering Progress Symposium Series*. Vol 62. ; 1966:100–101.
47. Ergun S. Fluid Flow through Packed Column. *Chem Eng Prog.* 1952;48:89.
48. Ruth BF, Montillon GH, Montonna RE. Studies in Filtration-I. Critical Analysis of Filtration Theory. *Ind Eng Chem.* 1933;25(1):76–82.
49. Ruth BF. Studies in filtration. II. Fundamental axiom of constant-pressure filtration. *Ind Eng Chem.* 1933;25:153–161.
50. Tiller FM. A revised approach to the theory of cake filtration. In: *Proc. Intern. Symp. Fine Particles Process, 1980*. Vol 2. ; 1980:1549–1582.
51. Tiller FM, Cooper H. The role of porosity in filtration: Part V. Porosity variation in filter cakes. *AIChE J.* 1962;8(4):445–449.
52. Tiller FM, Green TC. Role of porosity in filtration IX skin effect with highly compressible materials. *AIChE J.* 1973;19(6):1266–1269.
53. Tiller FM, Kwon JH. Role of porosity in filtration: XIII. Behavior of highly compactible cakes. *AIChE J.* 1998;44(10):2159–2167.
54. Tiller FM, Hsyung NB, Cong DZ. Role of porosity in filtration: XII. Filtration with sedimentation. *AIChE J.* 1995;41(5):1153–1164.

- 
55. Nield DA, Bejan A. *Convection in Porous Media*. Springer Science & Business Media; 2006.
  56. Scott GD, Kilgour DM. The density of random close packing of spheres. *J Phys Appl Phys*. 1969;2(6):863.
  57. Onoda GY, Liniger EG. Random loose packings of uniform spheres and the dilatancy onset. *Phys Rev Lett*. 1990;64(22):2727.
  58. Shapiro AP, Probst RF. Random packings of spheres and fluidity limits of monodisperse and bidisperse suspensions. *Phys Rev Lett*. 1992;68(9):1422.
  59. Brodkey RS, Hershey HC. *Transport Phenomena: A Unified Approach*. Brodkey publishing; 2003.
  60. Dong KJ, Yang RY, Zou RP, Yu AB, Roach G, Jamieson E. Simulation of the cake formation and growth in sedimentation and filtration. In: *Third International Conference on CFD in the Minerals and Process Industries, CSIRO, Melbourne, Australia*. ; 2003:10–12.
  61. Stein S, Tomas J. Modelling of the filtration behaviour using coupled DEM and CFD. In: *Discrete Element Modelling of Particulate Media*. ; 2012:113–120.
  62. Stein S. Simulation der Filtrations-und Konsolidierungsdynamik ultrafeiner Partikelsysteme mittels Kombination von Partikelmechanik, Diskrete-Elemente-Methode und Fluidodynamik: Micro-Macro Transactions. 2016.
  63. Dong KJ, Zou RP, Yang RY, Yu AB, Roach G. DEM simulation of cake formation in sedimentation and filtration. *Miner Eng*. 2009;22(11):921–930.
  64. Kabir MA, Gamwo IK. Filter cake formation on the vertical well at high temperature and high pressure: Computational fluid dynamics modeling and simulations. *J Pet Gas Eng*. 2011;7(2):146–164.
  65. Parry AJ. Numerical Prediction Method for Growth and Deformation of Filter Cakes. *J Fluids Eng*. 2006;128(6):1259–1265.
  66. Andersen NPR, Christensen ML, Keiding K. New approach to determining consolidation coefficients using cake-filtration experiments. *Powder Technol*. 2004;142(2-3):98–102.
  67. Iritani E, Matsumoto S, Katagiri N. Formation and consolidation of filter cake in microfiltration of emulsion–slurry. *J Membr Sci*. 2008;318(1-2):56–64.



68. Reichmann B, Tomas J. Expression behaviour of fine particle suspensions and the consolidated cake strength. *Powder Technol.* 2001;121(2-3):182–189.
69. Legendre D, Zenit R, Daniel C, Guiraud P. A note on the modelling of the bouncing of spherical drops or solid spheres on a wall in viscous fluid. *Chem Eng Sci.* 2006;61(11):3543–3549.
70. Joseph GG, Zenit R, Hunt ML, Rosenwinkel AM. Particle–wall collisions in a viscous fluid. *J Fluid Mech.* 2001;433:329–346.
71. Gondret P, Lance M, Petit L. Bouncing motion of spherical particles in fluids. *Phys Fluids.* 2002;14(2):643–652.
72. Joseph GG, Hunt ML. Oblique particle–wall collisions in a liquid. *J Fluid Mech.* 2004;510:71–93.
73. Davis RH, Serayssol J-M, Hinch EJ. The elastohydrodynamic collision of two spheres. *J Fluid Mech.* 1986;163:479–497.
74. ElectronicsTeache. Coefficient of friction values for clean surfaces, friction. <http://www.electronicsteacher.com/succeed-in-physical-science/friction/coefficient-of-friction-values-for-clean-surfaces.php>. Accessed April 23, 2018.
75. Oberg E, Jones FD, Horton HL, Ryffel HH, Geronimo JH. *Machinery's Handbook*. Industrial Press, Incorporated; 2016.
76. Lacombe R. *Adhesion Measurement Methods: Theory and Practice*. CRC Press; 2005.
77. Israelachvili JN. *Intermolecular and Surface Forces*. Academic press; 2011.
78. Pitz M, Hellmann A, Ripperger S, Antonyuk S. Development of a 3D Light Scattering Sensor for Online Characterization of Aerosol Particles. *Part Part Syst Charact.* 2018:1800045.
79. Carter RM, Yan Y. Measurement of particle shape using digital imaging techniques. In: *Journal of Physics: Conference Series*. Vol 15. IOP Publishing; 2005:177.
80. Kwan AK, Mora CF, Chan HC. Particle shape analysis of coarse aggregate using digital image processing. *Cem Concr Res.* 1999;29(9):1403–1410.
81. Osterroth S. *Mathematical Models for the Simulation of Combined Depth and Cake Filtration Processes*. BoD–Books on Demand; 2018.

- 
82. Osterroth S, Preston C, Markicevic B, Iliev O, Hurwitz M. The permeability prediction of beds of poly-disperse spheres with applicability to the cake filtration. *Sep Purif Technol.* 2016;165:114–122.
  83. Becker J, Cheng L, Kronsbein C, Wiegmann A. Simulation of cake filtration for polydisperse particles. *Chem Eng Technol.* 2016;39(3):559–566.
  84. Hager A, Kloss C, Pirker S, Goniva C. Parallel resolved open source CFD-DEM: method, validation and application. *J Comput Multiph Flows.* 2014;6(1):13–27.
  85. Bertrand F, Leclaire L-A, Levecque G. DEM-based models for the mixing of granular materials. *Chem Eng Sci.* 2005;60(8-9):2517–2531.
  86. Guo Y, Wu C-Y, Thornton C. Modeling gas-particle two-phase flows with complex and moving boundaries using DEM-CFD with an immersed boundary method. *AIChE J.* 2013;59(4):1075–1087.
  87. Kloss C, Goniva C, Hager A, Amberger S, Pirker S. Models, algorithms and validation for opensource DEM and CFD-DEM. *Prog Comput Fluid Dyn Int J.* 2012;12(2-3):140–152.
  88. Jajcevic D, Siegmund E, Radeke C, Khinast JG. Large-scale CFD-DEM simulations of fluidized granular systems. *Chem Eng Sci.* 2013;98:298–310.
  89. Liu D, Bu C, Chen X. Development and test of CFD-DEM model for complex geometry: A coupling algorithm for Fluent and DEM. *Comput Chem Eng.* 2013;58:260–268.
  90. Di Felice R. The voidage function for fluid-particle interaction systems. *Int J Multiph Flow.* 1994;20(1):153–159.
  91. Hill RJ, Koch DL, Ladd AJ. Moderate-Reynolds-number flows in ordered and random arrays of spheres. *J Fluid Mech.* 2001;448:243–278.
  92. Hill RJ, Koch DL, Ladd AJ. The first effects of fluid inertia on flows in ordered and random arrays of spheres. *J Fluid Mech.* 2001;448:213–241.
  93. Beetstra R. Drag force in random arrays of mono-and bidisperse spheres. 2005.
  94. Sarkar S, Kriebitzsch SHL, van der Hoef MA, Kuipers JAM. Gas–solid interaction force from direct numerical simulation (DNS) of binary systems with extreme diameter ratios. *Particuology.* 2009;7(4):233–237.

95. Sarkar S, Van der Hoef MA, Kuipers JAM. Fluid–particle interaction from lattice Boltzmann simulations for flow through polydisperse random arrays of spheres. *Chem Eng Sci.* 2009;64(11):2683–2691.
96. Beetstra R, van der Hoef MA, Kuipers JAM. Drag force of intermediate Reynolds number flow past mono-and bidisperse arrays of spheres. *AIChE J.* 2007;53(2):489–501.
97. Lu Y, Wei L, Wei J. A numerical study of bed expansion in supercritical water fluidized bed with a non-spherical particle drag model. *Chem Eng Res Des.* 2015;104:164–173.
98. Loth E. Drag of non-spherical solid particles of regular and irregular shape. *Powder Technol.* 2008;182(3):342–353.
99. Hölzer A, Sommerfeld M. Lattice Boltzmann simulations to determine drag, lift and torque acting on non-spherical particles. *Comput Fluids.* 2009;38(3):572–589.
100. Ganser GH. A rational approach to drag prediction of spherical and nonspherical particles. *Powder Technol.* 1993;77(2):143–152.
101. Schiller L. A drag coefficient correlation. *Zeit Ver Dtsch Ing.* 1933;77:318–320.
102. Solutions DEM. EDEM 2.3 user guide. *Edinb Scotl UK.* 2010.
103. CD-Adapco. *User Guide-STAR-CCM+ Version 8.06.* CD-Adapco; 2013.
104. Gopalakrishnan P, Tafti D. Development of parallel DEM for the open source code MFIX. *Powder Technol.* 2013;235:33–41.
105. Kloss C, Goniva C, Aichinger G, Pirker S. Comprehensive DEM-DPM-CFD simulations-model synthesis, experimental validation and scalability. In: *Proceedings of the Seventh International Conference on CFD in the Minerals and Process Industries, CSIRO, Melbourne, Australia.* ; 2009.
106. Anderson TB, Jackson R. Fluid mechanical description of fluidized beds. Equations of motion. *Ind Eng Chem Fundam.* 1967;6(4):527–539.
107. Tosun I. Formulation of cake filtration. *Chem Eng Sci.* 1986;41(10):2563–2568.

108. Hernández-Jiménez F, Third JR, Acosta-Iborra A, Müller CR. Critical Evaluation of Euler-Euler and Euler-Lagrangian Modelling Strategies in a 2-D Gas Fluidized Bed. 2011.
109. Adamczyk WP, Klimanek A, Białecki RA, Węcel G, Kozołub P, Czakiert T. Comparison of the standard Euler–Euler and hybrid Euler–Lagrange approaches for modeling particle transport in a pilot-scale circulating fluidized bed. *Particuology*. 2014;15:129–137.
110. Bensaid S, Marchisio DL, Fino D, Saracco G, Specchia V. Modelling of diesel particulate filtration in wall-flow traps. *Chem Eng J*. 2009;154(1-3):211–218.
111. Tien C, Bai R. An assessment of the conventional cake filtration theory. *Chem Eng Sci*. 2003;58(7):1323–1336.
112. Stamatakis K, Tien C. Cake formation and growth in cake filtration. *Chem Eng Sci*. 1991;46(8):1917–1933.
113. Zhou ZY, Kuang SB, Chu KW, Yu AB. Discrete particle simulation of particle–fluid flow: model formulations and their applicability. *J Fluid Mech*. 2010;661:482–510.
114. Zhu HP, Zhou ZY, Yang RY, Yu AB. Discrete particle simulation of particulate systems: theoretical developments. *Chem Eng Sci*. 2007;62(13):3378–3396.
115. Xu BH, Yu AB. Numerical simulation of the gas-solid flow in a fluidized bed by combining discrete particle method with computational fluid dynamics. *Chem Eng Sci*. 1997;52(16):2785–2809.
116. Smuts EM. A methodology for coupled CFD-DEM modeling of particulate suspension rheology. 2015.
117. Bokkers GA, van Sint Annaland M, Kuipers JAM. Mixing and segregation in a bidisperse gas–solid fluidised bed: a numerical and experimental study. *Powder Technol*. 2004;140(3):176–186.
118. Feng YQ, Yu AB. Assessment of model formulations in the discrete particle simulation of gas- solid flow. *Ind Eng Chem Res*. 2004;43(26):8378–8390.
119. Feng YQ, Xu BH, Zhang SJ, Yu AB, Zulli P. Discrete particle simulation of gas fluidization of particle mixtures. *AIChE J*. 2004;50(8):1713–1728.

120. Li S, Marshall JS, Liu G, Yao Q. Adhesive particulate flow: The discrete-element method and its application in energy and environmental engineering. *Prog Energy Combust Sci.* 2011;37(6):633–668.
121. Wadell H. The coefficient of resistance as a function of Reynolds number for solids of various shapes. *J Frankl Inst.* 1934;217(4):459–490.
122. Haider A, Levenspiel O. Drag coefficient and terminal velocity of spherical and nonspherical particles. *Powder Technol.* 1989;58(1):63–70.
123. Fand RM, Kim BYK, Lam ACC, Phan RT. Resistance to the flow of fluids through simple and complex porous media whose matrices are composed of randomly packed spheres. *J Fluids Eng.* 1987;109(3):268–273.
124. DCS Computing. LIGGGHTS(R)-PUBLIC Documentation, Version 3.X - LIGGGHTS v3.X documentation. <https://www.cfdem.com/media/DEM/docu/Manual.html>. Accessed March 26, 2018.
125. Di Renzo A, Di Maio FP. Comparison of contact-force models for the simulation of collisions in DEM-based granular flow codes. *Chem Eng Sci.* 2004;59(3):525–541.
126. Hertz H. Über die Berührung fester elastischer Körper [About the touch of solid elastic body]. *J Für Reine Angew Math.* 1882;92:156–171.
127. Zhang W, Noda R, Horio M. Evaluation of lubrication force on colliding particles for DEM simulation of fluidized beds. *Powder Technol.* 2005;158(1-3):92–101.
128. Davis RH, Rager DA, Good BT. Elastohydrodynamic rebound of spheres from coated surfaces. *J Fluid Mech.* 2002;468:107–119.
129. Lin S-Y, Lin J-F. Numerical investigation of lubrication force on a spherical particle moving to a plane wall at finite Reynolds numbers. *Int J Multiph Flow.* 2013;53:40-53.
130. Sun R, Xiao H. SediFoam: A general-purpose, open-source CFD–DEM solver for particle-laden flow with emphasis on sediment transport. *Comput Geosci.* 2016;89:207-219.
131. Brändle de Motta JC, Breugem W-P, Gazanion B, Estivalezes J-L, Vincent S, Climent E. Numerical modelling of finite-size particle collisions in a viscous fluid. *Phys Fluids.* 2013;25(8):083302.

132. Breugem W-P. A combined soft-sphere collision/immersed boundary method for resolved simulations of particulate flows. In: *ASME 2010 3rd Joint US-European Fluids Engineering Summer Meeting Collocated with 8th International Conference on Nanochannels, Microchannels, and Minichannels*. American Society of Mechanical Engineers; 2010:2381–2392.
133. Mindlin RD. Elastic spheres in contact under varying oblique forces. *Trans ASME J Appl Mech*. 1953;20:327–344.
134. Tsuji Y, Tanaka T, Ishida T. Lagrangian numerical simulation of plug flow of cohesionless particles in a horizontal pipe. *Powder Technol*. 1992;71(3):239–250. doi:10.1016/0032-5910(92)88030-L
135. Di Renzo A, Di Maio FP. An improved integral non-linear model for the contact of particles in distinct element simulations. *Chem Eng Sci*. 2005;60(5):1303–1312.
136. Zhou YC, Wright BD, Yang RY, Xu BH, Yu A-B. Rolling friction in the dynamic simulation of sandpile formation. *Phys Stat Mech Its Appl*. 1999;269(2):536–553.
137. Martin CL, Bordia RK. Influence of adhesion and friction on the geometry of packings of spherical particles. *Phys Rev E*. 2008;77(3):031307.
138. Johnson K, Kendell K, Roberts A. The adhesion and surface energy of elastic solids. *J Phys Appl Phys*. 1971;4(8):1186.
139. Behjani MA, Rahmanian N, Fardina bt Abdul Ghani N, Hassanpour A. An investigation on process of seeded granulation in a continuous drum granulator using DEM. *Adv Powder Technol*. 2017;28(10):2456–2464.
140. Official OpenFOAM Repository. *OpenFOAM-2.2.x: OpenFOAM Foundation Patch Version of OpenFOAM-2.2.*; 2018. <https://github.com/OpenFOAM/OpenFOAM-2.2.x>. Accessed May 2, 2018.
141. Miller GF, Pursey H, Bullard EC. On the partition of energy between elastic waves in a semi-infinite solid. *Proc R Soc Lond A*. 1955;233(1192):55–69.
142. Thornton C. *Granular Dynamics, Contact Mechanics and Particle System Simulations: A DEM Study*. Springer; 2015.
143. Martín MM. *Introduction to Software for Chemical Engineers*. CRC Press; 2014.

144. Wu CL, Zhan JM, Li YS, Lam KS, Berrouk AS. Accurate void fraction calculation for three-dimensional discrete particle model on unstructured mesh. *Chem Eng Sci.* 2009;64(6):1260–1266.
145. Wu S, Long X, Yang K. Accurate calculation and Matlab based fast realization of merit function's Hesse matrix for the design of multilayer optical coating. *Optoelectron Lett.* 2009;5(5):359–363.
146. Peng Z, Doroodchi E, Luo C, Moghtaderi B. Influence of void fraction calculation on fidelity of CFD-DEM simulation of gas-solid bubbling fluidized beds. *AIChE J.* 2014;60(6):2000–2018.
147. Wee Chuan Lim E, Wang C-H, Yu A-B. Discrete element simulation for pneumatic conveying of granular material. *AIChE J.* 2006;52(2):496–509.
148. Deb S, Tafti DK. A novel two-grid formulation for fluid-particle systems using the discrete element method. *Powder Technol.* 2013;246:601–616.
149. Issa RI. Solution of the implicitly discretised fluid flow equations by operator-splitting. *J Comput Phys.* 1986;62(1):40–65.
150. Nilsson H. A look inside icoFoam (and pisoFoam). lecture slides presented at the: Chalmers.  
[http://www.tfd.chalmers.se/~hani/kurser/OS\\_CFD\\_2013/aLookInsideIcoFoam.pdf](http://www.tfd.chalmers.se/~hani/kurser/OS_CFD_2013/aLookInsideIcoFoam.pdf). Accessed June 19, 2018.
151. Crüger B, Salikov V, Heinrich S, et al. Coefficient of restitution for particles impacting on wet surfaces: An improved experimental approach. *Particology.* 2016;25:1–9.
152. Richard D, Quéré D. Bouncing water drops. *EPL Europhys Lett.* 2000;50(6):769.
153. Foerster SF, Louge MY, Chang H, Allia K. Measurements of the collision properties of small spheres. *Phys Fluids.* 1994;6(3):1108–1115.
154. ISO 12103-1, A4 Coarse Test Dust. Powder Technology Inc. <http://www.powdertechologyinc.com/product/iso-12103-1-a4-coarse-test-dust/>. Accessed April 24, 2018.
155. Firefly S. UV-VIS Küvette Messungen & Küvetten Material Guide. FireflySci Cuvette Shop. <https://www.fireflysci.com/news/2016/1/26/kvette-fr-uv-vis-messungen-kvetten-material-guide>. Accessed January 28, 2018.

- 
156. Veritas I. Constellation 120E. Constellation 120E. <http://veritaslight.com/constellation-120e/>. Accessed January 28, 2018.
  157. Integrated Design Tools. Os-series digital high-speed camera. IDT Vision. <https://idtvision.com/products/cameras/os-series-cameras/>. Accessed January 28, 2018.
  158. The MathWorks Inc. MATLAB - MathWorks. <https://de.mathworks.com/products/matlab.html>. Accessed January 28, 2018.
  159. Zigrang DJ, Sylvester ND. An explicit equation for particle settling velocities in solid-liquid systems. *AIChE J.* 1981;27(6):1043-1044.
  160. Zanker A. Monographs determine settling velocities for solid-liquid systems. *Chem Eng Field.* 1980:147–50.
  161. Barnea E, Mizrahi J. A generalized approach to the fluid dynamics of particulate systems: Part 1. General correlation for fluidization and sedimentation in solid multiparticle systems. *Chem Eng J.* 1973;5(2):171–189.
  162. Barnea E, Mizrahi J. A generalised approach to the fluid dynamics of particulate systems part 2: Sedimentation and fluidisation of clouds of spherical liquid drops. *Can J Chem Eng.* 1975;53(5):461-468.
  163. Turton R, Clark NN. An explicit relationship to predict spherical particle terminal velocity. *Powder Technol.* 1987;53(2):127-129.
  164. Armstrong-Hélouvry B, Dupont P, De Wit CC. A survey of models, analysis tools and compensation methods for the control of machines with friction. *Automatica.* 1994;30(7):1083–1138.
  165. Anh LX. *Dynamics of Mechanical Systems with Coulomb Friction*. Springer Science & Business Media; 2012.
  166. Popov VL. *Contact Mechanics and Friction*. Springer; 2010.
  167. Maw N, Barber JR, Fawcett JN. The oblique impact of elastic spheres. *Wear.* 1976;38(1):101–114.
  168. Stable Micro Systems. Products TA. XT plus texture analyser. <https://stablemicrosystems.com/TAXTplus.html>. Accessed April 18, 2018.
  169. UHU GmbH & Co KG. Epoxy adhesives (2-component) - epoxi resin adhesives, acrylic adhesives and UHU repair powerkitt. <http://www.uhu.com/en/products/epoxy-adhesives-2-component/detail/uhu->



- plus-schnellfest2-k-epoxidharzkleber-1.html?cHash=6df9ccce606febc1d79f6833771ec22c&step=0. Accessed April 18, 2018.
170. Persson BNJ. *Sliding Friction: Physical Principles and Applications*. Springer Science & Business Media; 2013.
171. Gohar R. Film thickness and pressure distribution in elastohydrodynamic lubrication. In: *Elastohydrodynamics*. Published by imperial college press and distributed by world scientific publishing co.; 2001:169-224.
172. Chu PSY, Cameron A. Pressure viscosity characteristics of lubricating oils. *J Inst Pet*. 1962;48(461):147-155.
173. Cooper JR, Dooley RB. *Release on the IAPWS Formulation 2008 for the Viscosity of Ordinary Water Substance*. The International Association for the Properties of Water and Steam; :1-2.
174. Park SK, Miller KW. Random number generators: good ones are hard to find. *Commun ACM*. 1988;31(10):1192–1201.
175. Chen F. Coupled flow discrete element method application in granular porous media using open source codes. *Dr Diss*. 2009:21.
176. Antonyuk S, Heinrich S, Tomas J, Deen NG, van Buijtenen MS, Kuipers JAM. Energy absorption during compression and impact of dry elastic-plastic spherical granules. *Granul Matter*. 2010;12(1):15–47.
177. Gilson L, Kozhar S, Antonyuk S, Bröckel U, Heinrich S. Contact models based on experimental characterization of irregular shaped, micrometer-sized particles. *Granul Matter*. 2014;16(3):313–326.
178. Salikov V, Antonyuk S, Heinrich S, Sutkar VS, Deen NG, Kuipers JAM. Characterization and CFD-DEM modelling of a prismatic spouted bed. *Powder Technol*. 2015;270:622–636.
179. Audero MA, Bevilacqua AM, de Bernasconi NB, Russo DO, Sterba ME. Immobilization of simulated high-level waste in sintered glasses. *J Nucl Mater*. 1995;223(2):151–156.
180. Watkins IG, Prado M. Mechanical Properties of Glass Microspheres. *Procedia Mater Sci*. 2015;8:1057–1065.

- 
181. Mader-Arndt K, Aman S, Fuchs R, Tomas J. Contact properties determination of macroscopic fine disperse glass particles via compression tests in normal direction. *Adv Powder Technol.* 2017;28(1):101–114.
  182. Liu P, LaMarche CQ, Kellogg KM, Hrenya CM. Fine-particle defluidization: Interaction between cohesion, Young's modulus and static bed height. *Chem Eng Sci.* 2016;145:266-278.
  183. Volk A, Kähler CJ. Density model for aqueous glycerol solutions. *Exp Fluids.* 2018;59(5):75.
  184. Yang RY, Zou RP, Yu AB. Computer simulation of the packing of fine particles. *Phys Rev E.* 2000;62(3):3900.
  185. Dullien F. *Porous Media Fluid Transport and Pore Structure.* Elsevier; 2012.
  186. Hough DB, White LR. The calculation of Hamaker constants from Lifshitz theory with applications to wetting phenomena. *Adv Colloid Interface Sci.* 1980;14(1):3–41.
  187. Li Q, Rudolph V, Peukert W. London-van der Waals adhesiveness of rough particles. *Powder Technol.* 2006;161(3):248–255.
  188. Hager WH. Wilfrid Noel Bond and the Bond number. *J Hydraul Res.* 2012;50(1):3-9.
  189. McNown JS, Malaika J. Effects of particle shape on settling velocity at low Reynolds numbers. *Eos Trans Am Geophys Union.* 1950;31(1):74–82.
  190. Richardson JF, Zaki WN. The sedimentation of a suspension of uniform spheres under conditions of viscous flow. *Chem Eng Sci.* 1954;3(2):65-73.



---

## Index

---

Amplification factor .....	27	Filtration .....	1
Archimedes' force .....	18	Hard-sphere .....	3
cfdemSolverPiso .....	43	LAMMPS .....	43
Coefficient of restitution .....	51	LIGGGHTS .....	43
Coefficient of sliding friction.....	52	Mass weightage .....	21
Cohesion number .....	72	Mass weighted mean particle	
Computational Fluid Dynamics		diameter .....	21
(CFD) .....	4	Multi-element approach.....	4
Consolidation .....	3	Multi-sphere DEM modeling.....	34
Contact list .....	44	Non-spherical particle Reynolds	
Coordination number .....	73	number .....	23
Cutoff lubrication force.....	28	OpenFOAM .....	42
DEM-CFD coupling.....	5	Orientation .....	94
Depth filtration.....	1	Overlap .....	28
Dilute/dense flows.....	5	Packed bed/cake .....	2
Discrete Element Method (DEM) .....	3	Park-Miller algorithm .....	60
Distinct Element Method .....	3	Periodic condition for the particle	
Divided void fraction big .....	41	phase .....	60
Divided void fraction method .....	40	pisoFoam solver.....	42
Effective radius .....	30	Poly-dispersity correction factor .....	20
Effective Young's modulus.....	30	Relative angular velocity .....	33

Resolved coupling approach .....	8	Terminal Reynolds number .....	25
Single element approach .....	4	Thickness of the fluid .....	56
Soft-sphere .....	3	Two overlapping continua .....	15
Sphericity .....	24	Two-way coupling .....	5
Stokes number .....	45	Unit normal vector .....	30
Suspension correction factor .....	25	Void fraction .....	3
Tangential overlap .....	32	Volume equivalent diameter .....	22

---

## Publications

---

### Journals:

- Deshpande, Raturaj, Sergiy Antonyuk, and Oleg Iliev. "Study of the filter cake formed due to the sedimentation of monodispersed and bidispersed particles using discrete element method–computational fluid dynamics simulations." *AIChE Journal* 65, no. 4 (2019): 1294-1303.
- R. Deshpande, S. Antonyuk & O. Iliev "Analysis of the Filter Cake Formation Process due to Non-Spherical Particles Using DEM-CFD Simulations" *submitted*.

### Conferences:

- R. Deshpande, S. Antonyuk & O. Iliev "Analysis of filter cake formation using Computational Fluid Dynamics - Discrete Element Method (CFD-DEM) simulation" *Proceedings of the FILTECH 2016 Conference*. ([link](#))
- R. Deshpande, S. Antonyuk & O. Iliev "Study of compressible filter cake formation using DEM-CFD simulation." *European Congress on Computational Methods in Applied Sciences and Engineering, Crete Island, Greece, 5-10. Jun. 2016*. ([link](#))
- S. Antonyuk, R. Deshpande & O. Iliev "Effect of drag models and particle-particle interaction parameters on cake formation using Discrete Element Method-Computational Fluid Dynamics (DEM-CFD) simulation." *IV International Conference on Particle-Based Methods, Barcelona, Spain, 28-30. Sep. 2015*. ([link](#))

### Posters:

- O. Iliev, S. Antonyuk, & R. Deshpande "DEM-CFD coupling for the simulation of a filter cake formed due to the poly-dispersed particles" *InterPore, New Orleans, USA, 14-17. May. 2018*.
- R. Deshpande, S. Antonyuk, & O. Iliev "Study of filtration process using Computational Fluid Dynamics and Discrete Element Method (CFD-DEM) coupling." *International congress on Particle Technology Nuremberg PARTEC, Germany, 19-21. Apr. 2016*.



---

## Curriculum Vitae

---

### Personal Data:

Name	Ruturaj Ramesh Deshpande
Date of Birth	17. 09. 1988
Nationality	Indian
Place	Daund



### Education:

Oct.-2014 to Sep.-2018	PhD student Institute of Particle Process Engineering, TU Kaiserslautern, Germany and Fraunhofer ITWM, Kaiserslautern, Germany
Jul.-2011 to Jul.-2013	M.Eng. in Mechanical (Thermal Engineering) BITS, Pilani, India
Aug.-2006 to May.-2010	B.Eng. in Mechanical University of Pune, India

### Work Experience:

Mar.-2016 to Sep.-2018	Research Assistant Fraunhofer ITWM, Kaiserslautern, Germany
Jan.-2013 to Apr.-2013	Research Intern CD-adapco, Bangalore, India
Jul.-2011 to Dec.-2012	Teaching Assistant BITS, Pilani, India





---

## Lebenslauf

---

### Persönliche Daten:

Name	Ruturaj Ramesh Deshpande
Geburtsdatum	17. 09. 1988
Nationalität	Indisch
Ort	Daund



### Studium und Schule:

Okt.-2014 bis Sep.-2018	Doktorand Lehrstuhl für Mechanische Verfahrenstechnik, TU Kaiserslautern, Deutschland Und Fraunhofer ITWM, Kaiserslautern, Deutschland
Juli-2011 bis Juli-2013	M.Eng in Maschinenbau (Thermische Technik) BITS, Pilani, Indien
Aug.-2006 bis Mai-2010	B.Eng in Maschinenbau Universität von Pune, Indien

### Beruflicher Werdegang:

Mär.-2016 bis Sep.-2018	Hilfswissenschaftler Fraunhofer ITWM, Kaiserslautern, Deutschland
Jan.-2013 bis Apr.-2013	Forschungs-Praktikant CD-adapco, Bangalore, Indien
Jul.-2011 bis Dez.-2012	Lehrassistent BITS, Pilani, Indien



The process of cake filtration is used in many process industries where large quantities of solids are to be recovered/filtered. The present study is dedicated to the investigation of the filter cake formation process using DEM-CFD simulation with experimentally calibrated parameters. Experiments are carried out to measure the particle-particle interaction properties. Numerical analysis is carried out using a two-way volume averaged DEM-CFD coupling approach. For bi-dispersed and non-spherical particles, appropriate drag models are implemented and validated numerically. Then the sensitivity analysis of the various factors affecting the structure of the packed bed/cakes is performed. Further, the consolidation in the packed beds/cakes due to the fluid forces is studied.

ISBN 978-3-8396-1519-5



FRAUNHOFER VERLAG